Shear Regulation of Star Formation Efficiency in Nearby Galaxies

by

Joseph Nofech

A thesis submitted in partial fulfillment of the requirements for the degree of

Master of Science

Department of Physics

University of Alberta

Abstract

We use 7m ALMA CO(2-1) observations from the Physics at High Angular resolution in Nearby GalaxieS (PHANGS) survey combined with ultraviolet+infrared star formation rate (SFR) data from the z=0 Multiwavelength Galaxy Synthesis (z0MGS) project to measure the relationship between molecular depletion time $\tau_{\rm dep}$ and rotational shear β at 750 pc resolution. In addition to this main analysis, we use the available data to test a number of proposed star formation models. This is performed for 55 galaxies, the largest uniform sample of SFRs and molecular gas observations to date. Galaxy parameters are optimized by fitting CO(2-1) velocity centroid maps to a "flat disk" model using the DISKFIT software. These fits are used to produce smooth analytic fits to the universal rotation curve model for each galaxy, which are then used to measure shear. Overall, despite having a very large homogeneous sample of molecular gas and star formation data, we do not find substantial evidence for the influence of shear on star formation rate; nor do our data exhibit clear support for any of the proposed star formation models. However, we note that while some key quantities do not display a correlation overall (such as $\tau_{\rm dep}$ and β), weak correlations and anticorrelations of high statistical significance are still observed across many individual galaxies in our sample. This strongly suggests that there may be some common underlying factor(s) influencing the behaviour of these quantities.

Preface

This work was performed as part of the Physics at High Angular resolution in Nearby GalaxieS (PHANGS) international research collaboration, under the supervision of Professor E. Rosolowsky, the lead collaborator at the University of Alberta. The work presented in this thesis makes use of data from the Atacama Large Millimetre / submillimetre Array (ALMA) obtained and processed by the PHANGS data reduction team (led by Jerome Pety), as well as data from the WISE and GALEX satellites obtained and processed in the z=0 Multiwavelength Galaxy Synthesis (z0MGS) project (led by Adam Leroy).

When using the PHANGS-ALMA data to generate the kinematic parameters of galaxies using the DISKFIT software (Spekkens & Sellwood, 2007), the output fits were discussed with Philipp Lang and compared with work-in-progress kinematic parameter fits from his own work (Lang, Meidt, Rosolowsky, Nofech et al., in prep.). These discussions helped guide some decisions regarding how unsatisfactory fits (namely for inclinations) were handled and improved upon.

The work presented in this thesis will be published in a journal at a later date.

This thesis is dedicated to life, to life,
l'chaim.

Acknowledgements

I would like to express my deepest gratitude to my supervisor, Professor Erik Rosolowsky, for his endless patience, guidance, and expertise in acquainting me with the field and helping me complete this project. I also give my warmest thanks members of the PHANGS collaboration, Adam K. Leroy, Sharon Meidt, and Philipp Lang for their insight and advice on this work.

Contents

List of Tables

List of Figures

Chapter 1

Introduction

When we rewind time far enough into the past, we find that every living thing and everything that they interact with on a day-to-day basis exists as a consequence of star formation. We as living beings are composed of the remnants of dead stars, living on a rock composed of the remnants of dead stars, heated by a star that itself is enriched by the remnants of dead stars; and this star will proceed to enrich the surrounding interstellar medium with heavier elements when it eventually dies. This cycle of stellar birth and death is what populates the known Universe with the heavier material that composes planets as well as life itself. Understanding star formation forms a vital step in understanding our origins as a whole.

In this research project, we examine the interplay between star formation rates across galaxies and the large-scale rotational motions of the galaxies. Using high-resolution molecular emission maps from the Atacama Large Millimetre / submillimetre Array (ALMA), with combined infrared and ultraviolet star formation rate maps, we compare the depletion times throughout a number of galaxies with the properties of their rotation curve. With this data, we test whether the properties displayed any sort of correlation as predicted by theory. We also use our data to test a number of particularly prominent star formation models in the field.

Many abbreviations and symbols are used throughout this thesis. These are largely summarized in Table 1.1.

Abbreviation or Symbol	Definition	Units (if any)
PHANGS	Physics at High Angular Resolution in Nearby GalaxieS	
z0MGS	z=0 Multiwavelength Galaxy Synthesis	
ALMA	Atacama Large Millimetre / submillimetre Array	
WISE	Wide-field Infrared Survey Explorer	
GALEX	Galaxy Evolution Explorer	
MW	Milky Way	
GMC	giant molecular cloud	
ISM	interstellar medium	
FUV	far ultraviolet	
NUV	near ultraviolet	
SFR	star formation rate	
$\Sigma_{\rm SFR}$	surface density of star formation rate	$M_\odot\ {\rm yr}^{-1}\ {\rm kpc}^{-2}$
SFE	star formation efficiency	${\rm yr}^{-1}$
$\alpha_{\rm CO}^{(2-1)}$	CO(2-1)-to-molecular conversion factor	$(M_\odot\ {\rm kpc}^{-2})$ / (K km s^{-1})
$\Sigma_{\rm mol}$, $\Sigma_{\rm gas}$	surface density of (molecular / total) gas	$M_\odot\ {\rm kpc}^{-2}$
$W_{\rm CO}$	integrated line-of-sight CO(2-1) intensity	K km s^{-1}
$V_{\rm LoS}$	line-of-sight velocity	km s^{-1}
V	rotational velocity	km s^{-1}
R	radius from galaxy centre	kpc
$\tau_{\rm dep}$	depletion time	yr
$\tau_{\rm ff}$	freefall time	yr
$\tau_{\rm orb}$	orbital time	yr
β	logarithmic derivative of a rotation curve	unitless
κ	radial epicyclic frequency	kpc^{-1} s^{-1} km
A	Oort A parameter	kpc^{-1} s^{-1} km
$\sigma_{\rm g}$	velocity dispersion of the gas	km s^{-1}
Q	Toomre stability parameter	unitless
Ω	differential rotation	km s^{-1} kpc^{-1}
ρ	Spearman rank correlation coefficient	unitless

Table 1.1: Common abbreviations and symbols used throughout this thesis

1.1 Star Formation

The story of star formation begins and ends in the interstellar medium (ISM): the sparse gas, dust, and radiation in the otherwise largely-empty stretches of space within a galaxy. The properties of interstellar gas vary due to a wide variety of

factors such as turbulence, the large-scale motions of a galaxy, and the presence of stellar feedback; with temperatures ranging anywhere from T ~ 10 K to 10^6 K, and typical densities ranging anywhere from n $\sim 10^{-3}$ cm^{-3} to 10^2 cm^{-3}. We focus on the cold, dense phase of the ISM where star formation occurs.

A volume of cool interstellar gas will exert little outward pressure, and thus the densest, coolest regions of gas (called molecular clouds, with particularly large regions aptly known as giant molecular clouds) are where the gas is most likely to form gravitational instabilities that have insufficient pressure to prevent collapse. A dense cloud can be said to collapse if it meets the Jeans instability criterion; that is, if its mass exceeds the threshold "Jeans mass" of:

$$M_J \approx \left(\frac{5kT}{G\mu m_H}\right)^{3/2} \left(\frac{3}{4\pi\rho_0}\right)^{1/2} , \tag{1.1}$$

where T and ρ_0 are the initial temperature and density of the region, μ is the mean molecular weight of the gas (Carroll & Ostlie, 2006), m_H is the mass of a hydrogen atom, k is the Boltzmann constant, and G is the universal gravitational constant. The ISM is typically composed of around 90% hydrogen and 10% helium by number (or 80% H_2 molecules and 20% He atoms, in a cool molecular cloud), yielding a mean molecular weight of $\mu = 2.36$ in cool regions of the ISM where the hydrogen is entirely molecular.

As an illustrative example, a fairly typical star-forming region within these cool molecular clouds has a temperature of ~ 10 K and a number density of $\sim 10^4 \mathrm{cm}^{-3}$ (which, combined with the aforementioned mean molecular weight, yields a mass density of $\rho_0 = 3.9 \times 10^{-20}$ g cm^{-3}). This gives a Jeans mass of about $5\ M_\odot$, which is roughly on the scale of a typical stellar mass!

A cloud exceeding this Jeans mass will collapse, simultaneously heating up and losing energy to radiation as it falls. The cloud fragments in the process, taking a few million years to do so. Each fragment continues to collapse, eventually becoming dense enough to trap radiation, which slows the collapse somewhat due to an increase in temperature and pressure. The fragment continues to collapse until a sufficient heat is reached that the H_2 molecular bonds are broken, which allows infrared radiation to escape more easily and causes the fragment to rapidly collapse

once again.

The collapsing fragment increases in temperature and pressure as before, with cooler gas falling onto it from outside, until it reaches a sufficient temperature and pressure that hydrogen fusion begins in the core. When the contraction stops due to the nuclear burning, a main-sequence star is born.

The characteristic timescale over which this process occurs, in a simplified picture where the collapse overwhelms any potential opposing forces, is the free-fall time:

$$\tau_{\rm ff} = \sqrt{\frac{3\pi}{32 G \rho_0}} \, . \tag{1.2}$$

However, star formation is "inefficient". If all molecular gas were collapsing into stars at any given time, we would expect to observe star formation rates of $\Sigma_{\rm mol}/\tau_{\rm ff}$ (where $\Sigma_{\rm mol}$ is the molecular surface density of the gas), but the actual star formation rates observed are typically $\sim 1\%$ of this within the Milky Way (Krumholz & Tan, 2007) and for the many observed nearby galaxies (Utomo et al., 2018).

What makes star formation inefficient? A wide variety of possible explanations exist, but the reason for this star formation inefficiency is not yet well understood. Perhaps a good starting point for searching for the answer is to observe in a variety of galaxies how the star formation efficiency (i.e. the fraction of gas converted into stars over time) behaves in relation to other galactic parameters, and to make note of where it differs compared to predictions from models.

1.2 Observations of Star Formation

The star formation efficiency is commonly defined as the ratio between the star formation rate and the molecular gas mass (Leroy et al., 2013). It is the inverse of the molecular depletion time, the approximate timescale taken for a cloud of gas to deplete itself through a constant rate of star formation:

$$\tau_{\rm dep} = \frac{\Sigma_{\rm mol}}{\Sigma_{\rm SFR}} \, , \tag{1.3}$$

where $\Sigma_{\rm mol}$ refers to the molecular gas surface density throughout a galaxy, and $\Sigma_{\rm SFR}$ is the star formation rate (SFR) surface density throughout a galaxy. We will be using these two fundamental quantities to observe the depletion time throughout many nearby galaxies. The remainder of this section will provide more details regarding what these properties are, how they behave, and how they are measured.

1.2.1 Molecular Clouds

The cool, dense molecular clouds in which stars form can range from hundreds to millions of solar masses and typically span anywhere from tens of to well over a hundred parsecs. By mass, the gases that make up molecular clouds are roughly 70% hydrogen and slightly under 30% helium (with heavier trace elements and dust making up the remainder), and the fraction of the hydrogen that is molecular will vary throughout and among galaxies. Of course, the coldest ($T \sim 10$ K) and densest ($n > 10^4$ cm^{-3}; Kennicutt & Evans, 2012) regions within these clouds are capable of forming gravitational instabilities that overcome their self-pressure and thus collapse into stars.

Unfortunately, despite being abundant and widespread, H_2 is nearly invisible. The lowest-level excitation state of H_2 is its J=1 rotational state, occurring at 175 K above the ground state; however, the molecular clouds in which H_2 resides are typically below ~ 100 K, meaning that very few H_2 molecules will be emitting any light. On top of this, the molecule being diatomic and symmetric means that this particular transition is forbidden in the first place (Krumholz, 2015), so in the end this transition would not occur to begin with even if the molecular clouds were somehow hot enough.

Essentially, because H_2 is so difficult to observe directly, we instead rely on tracers such as CO and dust that tend to be present under similar conditions as H_2.

CO

CO is the most abundant molecule after H_2 itself, and appears in roughly the same places and conditions as H_2 (Krumholz, 2015; Bolatto et al., 2013). Unlike H_2, CO

has a number of rotational states that can be reached at very low temperatures; for example, it can be excited from the ground state to the $J = 1$ rotational state at 5.5 K. This means that it will readily emit light at the incredibly low temperatures of the clouds in which it resides. As a result, CO is incredibly useful as a tracer.

Both ^{12}CO and ^{13}CO, the most common isotopologues of CO, are used for studying molecular gas. Emission from ^{13}CO is optically thin due to its comparitively lower abundance, and optically thin emission lines can be used to measure the column densities of the emitting gas by simply counting the photons received. This makes ^{13}CO a useful tracer for molecular gas within the Milky Way; however, it is less reliable for extragalactic observations due to how sparse the emission is. Instead, ^{12}CO is used for studies observations due to its abundance.

^{12}CO is not optically thin, which somewhat complicates the relationship between the detected ^{12}CO intensity and the corresponding amount of gas. In general, the intensity of a spectral line at some frequency ν through a cloud of optical depth τ_ν is:

$$I_\nu = \left(1 - e^{-\tau_\nu}\right) B_\nu(T) \, , \tag{1.4}$$

where $B_\nu(T)$ is Planck's function at frequency ν and gas temperature T; and the optical depth itself follows a Gaussian profile about the line's central frequency ν_0 that widens based on the one-dimensional velocity dispersion of the gas $\sigma_{\rm 1D}$:

$$\tau_\nu = \tau_{\nu_0} e^{-\frac{(\nu-\nu_0)^2}{2(\nu_0 \sigma_{\rm 1D}/c)^2}} \, , \tag{1.5}$$

where τ_{ν_0} is the "peak" optical depth and c is the speed of light.

Essentially, the intensity becomes $B_\nu(T)$ at frequencies where the emission is optically thick ($\tau_\nu \gg 1$), and drops to nearly zero elsewhere. That is, the height of the intensity profile increases with temperature, and the width increases with velocity dispersion. Indeed, Krumholz (2015) shows that the total intensity integrated across the spectrum (in standard radio astronomy units of $\mathrm{K\,km\,s^{-1}}$) is roughly proportional to the gas temperature multiplied by the velocity dispersion.

The significance of this result is that the ratio between the expected mass density from a cloud with optically thick emission and the integrated intensity of this

emission (which is theoretically proportional to temperature multiplied by velocity dispersion) turns out to be roughly *constant*, under the assumptions that molecular clouds are approximately virialized and that molecular clouds have similar volume densities across large scales (Krumholz, 2015). This implies that although ^{12}CO emission is not optically thin, the turbulent structure of molecular clouds means that the line luminosity is still a good tracer of the molecular mass, and we are therefore able to empirically calibrate the CO intensity to the H_2 mass (Bolatto et al., 2013) with a simple conversion factor. The conversion factor that we use will be described in Section 2.3.

Dust

Dust makes up roughly 1% of the ISM by mass (Bolatto et al., 2013), and is made up of solid metals of up to ~ 0.1 μm in size. Despite being very sparse compared to the gaseous ISM, dust is still a useful tracer through its emissive and absorptive properties.

Dust stands out from its gaseous surroundings by being able to emit thermal radiation. Dust emission is optically thin, so the intensity of dust emission received from a cloud (which is a mixture of gas and dust) at a given wavelength can be thought of as:

$$I_\nu = \tau_\nu B_\nu(T) \, , \tag{1.6}$$

where $B_\nu(T)$ is Planck's function and $\tau_\nu = \Sigma_{\rm mix}\kappa_\nu$ is the optical depth of the cloud (where κ_ν is the opacity per gram of the cloud at a certain frequency, and $\Sigma_{\rm mix}$ is the cloud's surface density). What this essentially means is that if κ_ν and temperature can be determined, then the surface density of the cloud (which is overwhelmingly gas by mass; that is, $\Sigma_{\rm mix} \approx \Sigma_{\rm gas}$) can be found by measuring the intensity of the thermal dust emission at a known frequency (Krumholz & Tan, 2007).

In addition, dust also absorbs light from stars (especially around the ultraviolet regime) and re-emits it (mainly as infrared). If κ_ν is known, then the column gas density of a cloud can also be measured as:

$$\Sigma_{\rm gas} \approx \frac{A(\nu)}{\kappa_\nu} \, , \tag{1.7}$$

where $A(\nu)$ is the extinction of starlight through the cloud (Krumholz, 2015). Dust is especially prone to scattering and absorption of shorter wavelength light (i.e. ultraviolet and beyond), and re-emitting the absorbed energy as infrared, making this effect particularly useful in actively star-forming regions where younger, bluer stars are nearby. As a result of emitting and re-emitting behaviours, dust is useful as a tracer of the ISM in general.

1.2.2 Star Formation Rates

Regions undergoing active star formation will be home to young, massive stars with strong UV radiation. Star formation rates can in principle be traced by simply observing the UV emission; however, a major problem is the fact that star formation happens deep in molecular clouds, and much of the UV radiation is absorbed by the accompanying dust in the thick surrounding gas.

In nearby regions within the Milky Way, star formation rates can be measured almost directly by simply counting the number of stars that form. The Milky Way has near-complete catalogs of young stellar objects (YSOs; that is, protostars and pre-main-sequence stars) available, and the star formation rates within the Galaxy can be thought of as the total mass of these YSOs divided by their lifetimes; that is,

$$\langle \mathrm{SFR} \rangle = \frac{N(\mathbf{YSOs}) \times \langle M_{\mathrm{YSOs}} \rangle}{t_{\mathrm{YSOs}}} \text{ (Kennicutt \& Evans, 2012),} \tag{1.8}$$

where the approximate lifetimes can be calibrated with respect to another category of stellar objects. As an example, if the ratio of pre-main-sequence stars to protostars is known, and the characteristic lifetime of protostars is known through observations of infrared excesses, then the lifetime of the pre-main-sequence stage can simply be approximated as the age of the protostars multiplied by this ratio.

Measuring the star formation rates outside the Milky Way is a different story entirely, as individual stars can no longer be resolved. We instead rely on near- and far-ultraviolet radiation (NUV and FUV, respectively) as indicators of high-mass (i.e. young) stars; however, as mentioned above, about half of the UV radiation is absorbed by surrounding dust and re-radiated as infrared continuum or as infrared emissions from polycyclic aromatic hydrocarbons (Kennicutt & Evans, 2012). As

such, it is better and increasingly common to combine UV observations with IR observations to measure extragalactic star formation rates, which is what we will be doing in this work. In addition to the aforementioned NUV and FUV radiation, infrared continuum emission, and infrared polycyclic aromatic hydrocarbon emission, other tracers of recent star formation also exist. Young massive stars will emit extreme UV radiation as well; that is, photons with energies above $13.6\ \mathrm{eV}$ that ionize surrounding hydrogen atoms, which in return will produce detectable Hα lines through recombination.

1.3 Star Formation in Galaxies

It is important to observe star formation within a variety of galaxies to detect patterns regarding the behaviour of star formation efficiency. However, due to the sheer distance to these galaxies and due to the relatively low resolution of radio imaging, our ability to analyze other galaxies is quite limited compared to that for our own Milky Way (MW). Current techniques give resolution elements roughly on the scale of molecular clouds for nearby galaxies; we are unable to "see" extragalactic molecular clouds (let alone their dense cores) in quite the same manner that can be observed in the MW.

Another limitation of observing from this "zoomed-out" perspective is our "two-dimensional" view of these galaxies, which makes it difficult to accurately compute properties like volume density (and consequently free-fall time; see Equation 1.2). Without access to data of the same linear resolution as what the MW provides, we are unable to use the techniques that grant this coveted three-dimensional view of each galaxy; that is, we cannot measure the free-fall time (Equation 1.2) very accurately. Instead, we rely on timescales based on the 2D observables, such as the molecular surface density.

These 2D observables are still very useful, and there exist a variety of empirical relationships between 2D surface densities and quantities such as star formation. Kennicutt (1998) compares the galaxy-averaged star formation rates to the total gas densities of numerous entire galaxies, revealing a simple trend now commonly

referred to as the Kennicutt-Schmidt Law:

$$\Sigma_{\rm SFR} \propto \Sigma_{\rm gas}^{N} \ , \tag{1.9}$$

where $N = 1.4 \pm 0.15$ (Kennicutt, 1998). Note that this $\Sigma_{\rm gas}$ represents the total gas surface density rather than the molecular gas density.

Leroy et al. (2008) shows that the molecular fraction of this gas density tends to smoothly decrease with increasing radius from the center of a galaxy, with hydrogen at small radii being almost completely H_2. Regions of mostly-molecular gas tends to have a fairly constant depletion time in spiral galaxies, at $\sim 2 \times 10^9$ yr, whereas this depletion time dramatically increases further outwards, indicating a strong dependence of star formation on galactic environment. Leroy et al. (2013) constrains this result further, obtaining a value of 2.2 Gyr with 0.3 dex scatter (1σ) when comparing 30 galaxies with each line of sight weighed equally (although overall depletion times still varied from galaxy to galaxy). In addition, their data reveals a tight correlation between the star formation rate and the molecular gas density (as opposed to the total gas density), such that:

$$\Sigma_{\rm SFR} \propto \Sigma_{\rm mol}^{N} \ , \tag{1.10}$$

where $N = 1.0 \pm 0.2$. These results are shown in Figure 1.1.

1.4 Theoretical Models for Star Formation in Galaxies

There are a large variety of star formation models that can be used to predict the depletion time throughout a galaxy. Following Leroy et al. (2008), we outline several proposed models that we will be testing using our data. In this work, we focus on the those models that depend on the rotation curve of the galaxy but compare to other dominant models in the literature for context. We summarize the results of these comparisons in Section 4.2.

It is worth noting that each model requires different data in order to test, with some being reliant on the rotation curve of the galaxy (Section 3). In addition, it is also worth noting that certain models require the use of the total gas surface density

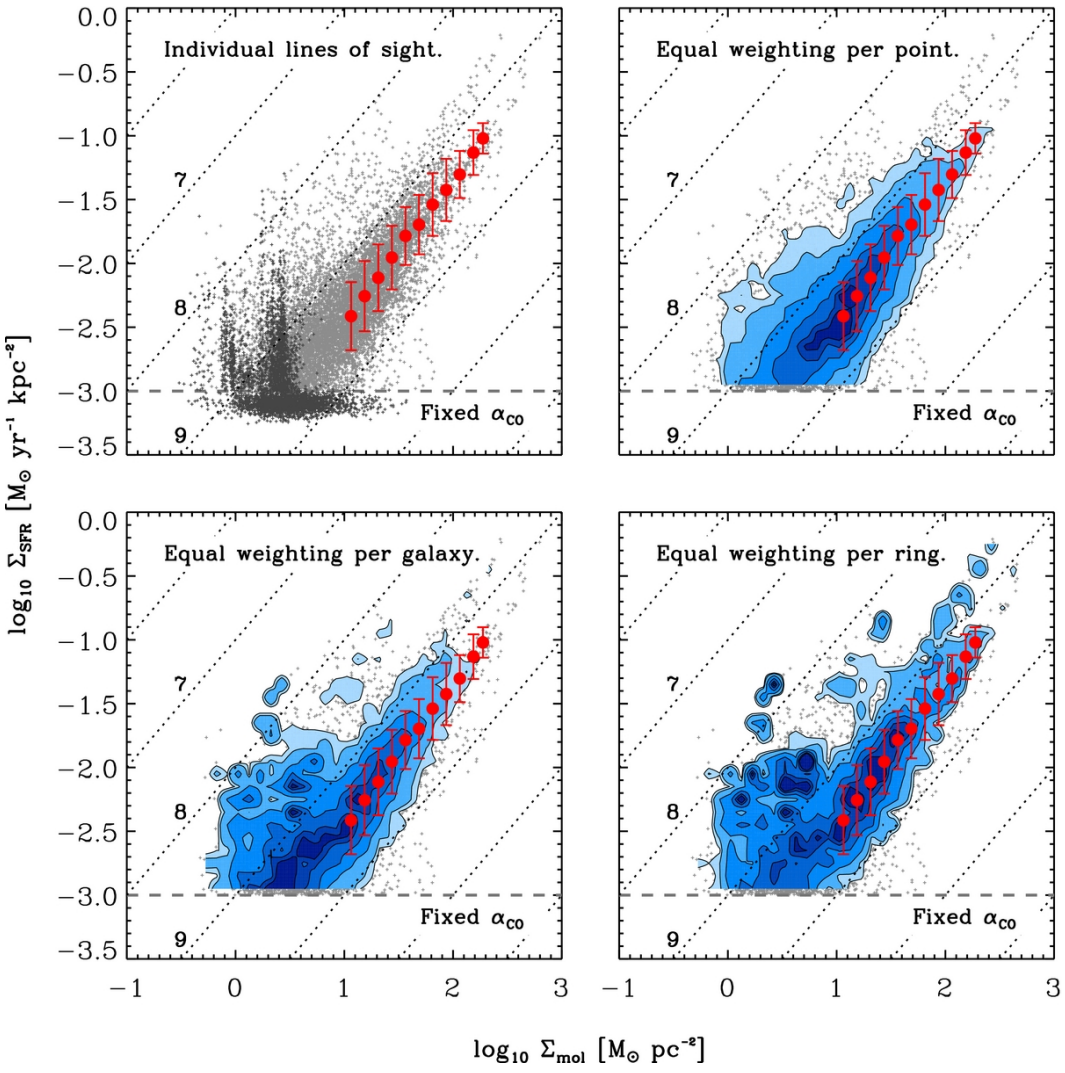

Figure 1.1: Star formation law from Leroy et al. (2013). Used with permission.

($\Sigma_{\rm gas}$) rather than the molecular gas surface density ($\Sigma_{\rm mol}$). For these models we will assume a constant molecular fraction of approximately 1 due to the lack of atomic gas data for all of our sample; that is, we assume $\Sigma_{\rm mol} \sim \Sigma_{\rm gas}$. Models involving $\Sigma_{\rm gas}$ tend to come from the Kennicutt (1998) era of star formation models, when $\Sigma_{\rm gas}$ was considered the key quantity for determining star formation rate; however, more recent observations (Leroy et al., 2013) instead suggest that $\Sigma_{\rm mol}$ is the dominant factor, as stars form from molecular gas rather than atomic gas.

1.4.1 Constant H_2 Star Formation Efficiency

This model describes the case where the depletion time is purely dependent on the properties of the cloud population, which are assumed to be independent of the properties of the galaxy environment around it. With this assumption, the star formation efficiency (and its inverse, the depletion time) of H_2 is assumed to be approximately constant if GMCs have largely similar intrinsic properties, and if the interior behaviour of the clouds is largely decoupled from the surrounding ISM as a whole. If these conditions are met and the observations include several clouds within each resolution element, then the H_2 depletion time is roughly constant, and the overall depletion time of the cloud can be described as:

$$\tau_{\rm dep}^{\rm gas} = \tau_{\rm dep,H_2} \frac{R_{\rm mol} + 1}{R_{\rm mol}} \, , \tag{1.11}$$

where $R_{\rm mol} = \Sigma_{\rm H2}/\Sigma_{\rm HI}$ (Leroy et al., 2008). Because we assume a consistent molecular fraction of ~ 1, this simplifies to $\tau_{\rm dep}^{\rm gas} \approx \tau_{\rm dep,H_2}$.

We use this model as a naive conjecture that broadly agrees with large scale measurements of the star formation law (Leroy et al., 2013), which serves as a useful comparison to other models.

1.4.2 Gravitational Instability in a Gas Disk

The Toomre Q parameter describes the threshold at which instabilities in a gaseous disk will collapse:

$$Q_{\rm gas} = \frac{\sigma_{\rm g} \kappa}{\pi G \Sigma_{\rm gas}} \, , \tag{1.12}$$

where $\sigma_{\rm g}$ is the velocity dispersion of the gas (see Section 2.1), κ is the radial epicyclic frequency (see Section 3.3), and $\Sigma_{\rm gas}$ is the surface density of the gas (which we simply estimate to be $\Sigma_{\rm mol}$). This model can be thought of as a slight refinement of the previous conjecture, and describes a scenario where an instability (i.e. collapse) occurs if $Q < 1$; otherwise the region is stable against collapse and star formation does not occur. We essentially expect lower depletion times for lower Q.

1.4.3 Disk Free-fall Time with Fixed Scale Height

With free-fall time being the approximate timescale for star formation, this model is essentially the Kennicutt-Schmidt law (Equation 1.9) using the Kennicutt (1998) value of $N = 1.4$, while assuming a fixed scale height for GMC volume (i.e. assuming that $\rho_{\rm gas} \propto \Sigma_{\rm gas}$). In this case, this N value can be approximately thought of as a result of stars collapsing on a scale of the gas free-fall time (where $\tau_{\rm ff}^{\rm gas} \propto \rho_{\rm gas}^{-0.5}$), such that if $\Sigma_{\rm SFR} \propto \Sigma_{\rm gas}^{1.5}$ (Leroy et al., 2008), then it follows that the star formation efficiency is $\Sigma_{\rm SFR}/\Sigma_{\rm gas} \propto \Sigma_{\rm gas}^{0.5}$ and its inverse is $\tau_{\rm dep}^{\rm gas} \propto \Sigma_{\rm gas}^{-0.5}$. This means that the correlation $\tau_{\rm dep}^{\rm gas} \propto \tau_{\rm ff}^{\rm gas}$ is expected.

1.4.4 Orbital Timescale

This is a very simple model that treats the orbital time as the approximate timescale for star formation (Silk, 1997; Elmegreen, 1989). Thus,

$$\begin{aligned} \tau_{\rm dep}^{\rm gas} &\propto \tau_{\rm orb} \ , \\ &\propto \frac{2\pi}{\Omega} \ , \end{aligned} \tag{1.13}$$

where $\Omega = V(R)/R$ is the differential rotation throughout a galaxy, and $V(R)$ is the rotational velocity at radius R.

1.4.5 GMC Collisions

Tan (2000) describes a model in which rotational shear throughout a galaxy "enhances the collision rate" of clouds, which gives rise to increased star formation

rates. This model (hereafter the "GMC collision model") is as follows:

$$\Sigma_{\rm SFR}(R) \quad \propto \quad \Sigma_{\rm gas}\Omega(1-0.7\beta)/Q \ , \tag{1.14}$$

that is, it predicts a proportionality between the depletion times and the timescale for clouds to collide due to shear:

$$\tau_{\rm dep}^{\rm gas} \quad \propto \quad Q/\Omega(1-0.7\beta) \ , \tag{1.15}$$

where β (the logarithmic derivative of the rotation curve) describes the amount of rotational shear throughout the galaxy, with regions of low shear ($\beta = 1$) decreasing the rate of cloud collisions and thereby increasing $\tau_{\rm dep}^{\rm gas}$, and vice versa for regions of increased shear ($\beta = 0$).

1.4.6 Meidt et al. 2018 Model

Meidt et al. (2018) asserts that the effect of cloud-scale shear on a galactic potential can inhibit dense regions from collapsing. The shear from galactic motions across a cloud-sized region can be approximately described by:

$$\sigma_{\rm gal} \sim R_{\rm c}\kappa \ , \tag{1.16}$$

where κ is the epicyclic frequency of the cloud's motion (see Section 3.3), and $R_{\rm c}$ is the radius of the cloud. Essentially, with this cloud-scale shear hindering the collapse of dense regions, the model predicts that κ is the dominant term in setting the star formation rates, so a positive correlation between $\tau_{\rm dep}$ and κ is expected.

1.4.7 Shear-Regulated Model

Hunter et al. (1998) presents a star formation model in which rotational shearing motions can inhibit instabilities from collapsing. It essentially predicts a threshold gas density proportional to the Oort A parameter (Leroy et al., 2008), where star formation rates increase as the gas density above this threshold increases. Below this threshold, star formation does not occur. This model essentially predicts that larger shears as parameterized by A lead to longer depletion times.

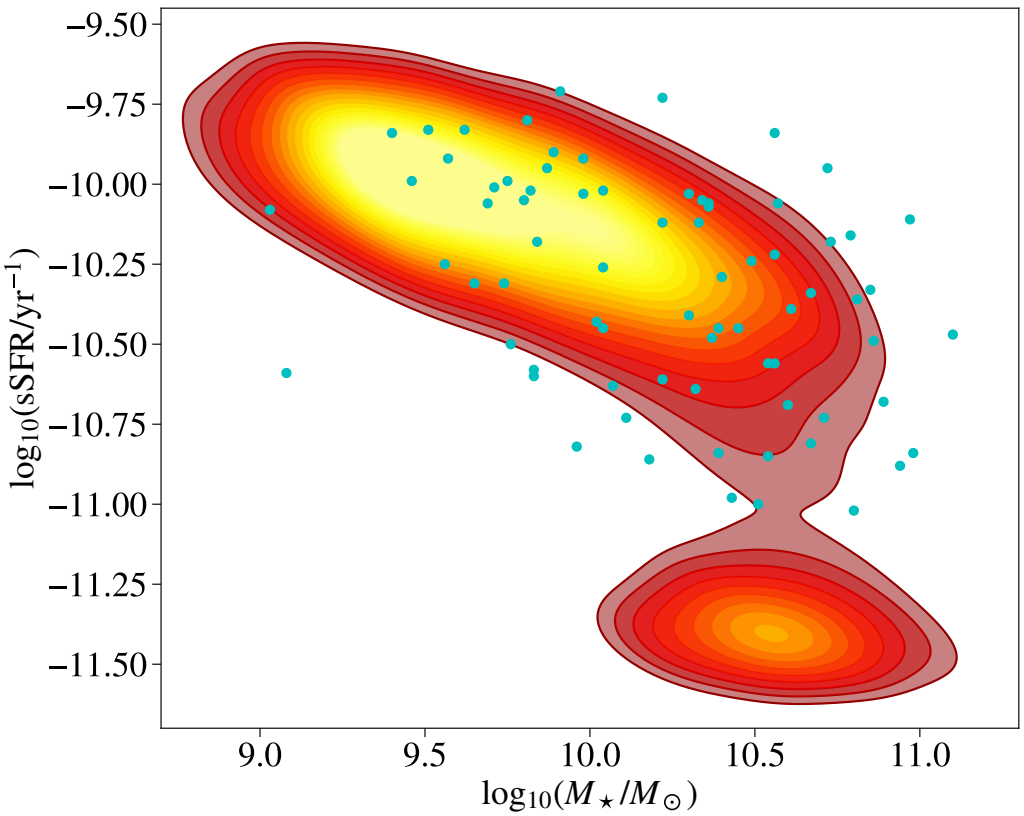

Figure 1.2: PHANGS Sample (cyan points) overlaid on the z0MGS population of local galaxies. This figure illustrates how the PHANGS sample samples the star forming main sequence of galaxies. Figure courtesy of Erik Rosolowsky; used with permission.

1.5 Motivation

This research was performed as part of the Physics at High Angular resolution in Nearby GalaxieS (PHANGS) collaboration. The primary goal of PHANGS is to use new high-resolution images of nearby galaxies to understand the interplay between the small "cloud"-scale physics, the physics within the interstellar medium, star formation and feedback, and the overall large-scale motions of a galaxy; as well as to understand how these pieces all come together to affect the evolution of a galaxy as a whole.

The observational scope of PHANGS includes nearby galaxies beyond the Local Group, with primary targets (see Figure 1.2) consisting mostly of disk galaxies on the "star-forming main sequence" of galaxies. For clarity, if one were to compare

the overall star formation rate with the overall stellar mass across a wide variety of galaxies, this "star-forming main sequence" would essentially describe the many star-forming galaxies that exhibit a fairly tight correlation between the two properties (as opposed to "starburst" or "red cloud" galaxies, whose star formation rates are respectively much higher or much lower than this trend; Schiminovich et al., 2007).

PHANGS currently has a number of ongoing observational campaigns, including ALMA $\sim$ 1" CO(2-1) imaging of over 74 disk galaxies, VLA HI imaging of 21 nearby galaxy disks, Astrosat far-ultraviolet (FUV) imaging of 6 nearby galaxy disks, VLT/MUSE 1" optical imaging of $\sim$ 20 nearby disk galaxies, and HST imaging of 38 nearby disk galaxies. For this research in particular, we used ALMA $\sim$ 7" CO(2-1) data for the 74 galaxies.

The primary goal of this research is to combine this PHANGS CO(2-1) data with corresponding star formation rate maps from the z=0 Multiwavelength Galaxy Synthesis (z0MGS) project (which combines IR+UV data from the WISE+GALEX surveys; Leroy et al., accepted) to observe the relationship between the depletion time of galaxies (that is, the approximate timescale for a GMC to deplete itself assuming a constant rate of star formation) with their rotational shear (which we will primarily parameterize as β, the logarithmic derivative of the rotation curve), to see whether the rotational shear throughout a galaxy has any correlation with the star formation throughout. The ratio between the depletion times and free-fall times (the approximate timescale for star formation, and thus the approximate timescale for interstellar medium evolution) as well as the ratio between depletion times and the orbital timescales (the timescale over which galactic dynamical effects take place) will also be compared to rotational shear for this purpose. Further details about this data are provided in Section 2.

This analysis is performed for 55 of the primary PHANGS target galaxies, making this the largest uniform sample of SFRs and molecular gas observations to date. Figure 2.2 displays the relationship between $\Sigma_{\rm SFR}$ and $\Sigma_{\rm mol}$ for these 55 galaxies (calculated as described in Section 2), and shows strong agreement with the previous generation of star formation studies (Leroy et al., 2013). As part of our analysis,

we use velocity centroid maps from the ALMA data to generate rotation curves using the DISKFIT software, and optimize galactic parameters (such as inclinations and kinematic position angles), for each of the galaxies (Section 3.1). Finally, we also test the theoretical models described in Section 1.4 for these galaxies using the data at hand.

The remainder of this section will outline how the paper is organized. Section 2 will describe in detail where the initial data we used comes from, for which galaxies this desired data is available, and how this data is converted into the convenient 2D maps that we use for our analysis. Section 3 will detail how the rotation curves are generated for the target galaxies, from the initial galactic parameter optimizations with DISKFIT to the final fits to theoretical rotation curve models. Section 4 demonstrates the results of our analyses from these completed data products, and includes the tests for the various star formation models presented in Section 1.4. Section 5 will discuss how the results compare with expectations and why the results behave this way, and includes the results if an alternate method of converting CO(2-1) intensity to molecular surface density is used. The work is then summarized and concluded in Section 6, and the Appendix describes a variety of alternative methods that were used to test correlations between depletion time and rotational shear.

Chapter 2

Data

In this section we discuss where our data originated, and how the quantities we consider in our analysis are derived from this data.

2.1 PHANGS ALMA CO(2-1)

We use data from the PHANGS survey of nearby galaxies, which was taken as part of the Large ALMA Program (2017.1.00886.L). This data comprises of CO(2-1) spectral line imaging for a set of nearby ($d < 17$ Mpc), relatively massive ($M_\star > 5 \times 10^9\ M_\odot$) and face-on ($i < 75°$) galaxies undergoing active star formation ($\dot{M}_\star / M_\star > 10^{-11}\ \mathrm{yr}^{-1}$), in a region of the sky viewable by the ALMA observatory (Dec $< +25°$). This yields a set of 74 galaxies that we will refer to as the primary PHANGS targets, 55 of which are considered in our primary analysis; with most exclusions being due to limitations of the data, such as insufficient resolutions compared to the star formation rate data (as detailed in Section 2.3). However, as part of our analysis involves generating the rotation curves for these galaxies from their velocity centroid maps using the DISKFIT software (which occurs independently of the galaxies' star formation rates), rotation curves are generated for 72 of these initial 74 galaxies as well.[1] Table 2.1 summarizes the basic properties of these 72 galaxies.

[1] Of the primary PHANGS targets, NGC3239 is an irregular galaxy, and NGC4694 has insufficient coverage such that DISKFIT is unable to generate a reasonable rotation curve fit. As such, the two are excluded from all calculations.

Galaxy	RA (°)	Dec (°)	Distance (Mpc)	$\log(M_\star)$	Bar	T	R_e (kpc)
IC1954*	52.879707	-51.904861	15.2	9.75	True	3.3	2.8
IC5273*	344.861176	-37.702839	14.7	9.66	True	5.6	2.5
IC5332*	353.614441	-36.101059	9.9	9.58	True	6.8	4.2
NGC0628*	24.173855	15.783643	9.8	10.18	False	5.2	4.5
NGC0685	26.928452	-52.761978	16.0	9.73	True	5.4	4.0
NGC1087*	41.604919	-0.498717	14.4	9.75	True	5.2	2.5
NGC1097*	41.578957	-30.274675	14.2	10.66	True	3.3	3.4
NGC1300	49.920815	-19.411114	26.1	10.77	True	4.0	9.5
NGC1317*	50.684540	-37.103790	19.0	10.53	True	0.8	2.1
NGC1365*	53.401520	-36.140404	18.1	10.71	True	3.2	3.8
NGC1385	54.369015	-24.501162	22.7	10.14	True	5.9	3.4
NGC1433*	55.506195	-47.221943	16.8	10.64	True	1.5	5.3
NGC1511*	59.902458	-67.633926	15.6	9.81	False	2.0	2.4
NGC1512*	60.975574	-43.348724	16.8	10.49	True	1.2	4.6
NGC1546*	63.651218	-56.060898	18.0	10.29	False	-0.4	2.4
NGC1559	64.402382	-62.783409	19.8	10.18	True	5.9	3.9
NGC1566*	65.001587	-54.938011	18.0	10.62	True	4.0	4.1
NGC1637	70.367424	-2.857936	9.8	9.54	True	5.0	2.3
NGC1672*	71.427040	-59.247257	11.9	10.17	True	3.3	2.7
NGC1792*	76.309692	-37.980560	12.8	10.26	True	4.0	3.4
NGC1809	75.520660	-69.567940	15.0	9.30	False	5.0	···
NGC2090*	86.757874	-34.250599	11.8	9.92	False	4.5	2.0
NGC2283	101.469971	-18.210800	10.4	9.47	True	5.9	2.4
NGC2566	124.690033	-25.499519	23.7	10.39	True	2.7	4.9
NGC2775*	137.583954	7.038066	17.0	10.79	False	1.6	3.5
NGC2835*	139.470444	-22.354679	10.1	9.64	True	5.0	3.7
NGC2903*	143.042114	21.500841	8.5	10.36	True	4.0	3.6
NGC2997*	146.411636	-31.191090	11.3	10.40	True	5.1	5.6
NGC3059	147.533997	-73.922195	19.8	10.15	True	4.0	4.4
NGC3137*	152.281158	-29.064301	14.9	9.70	True	5.9	4.5
NGC3351*	160.990646	11.703670	10.0	10.21	True	3.1	3.2
NGC3507	165.855728	18.135521	20.9	10.38	True	3.1	3.8
NGC3511*	165.849213	-23.086714	9.9	9.63	True	5.1	3.3
NGC3521*	166.452393	-0.035949	11.2	10.76	True	4.0	3.9
NGC3596	168.775803	14.787066	10.1	9.40	True	5.2	1.6
NGC3621*	169.567917	-32.812599	6.6	9.86	True	6.9	2.7
NGC3626	170.015884	18.356846	20.0	10.41	False	-0.8	1.8
NGC3627*	170.062515	12.991500	10.6	10.61	True	3.1	3.6
NGC4207*	183.876816	9.584928	16.8	9.62	False	7.7	1.2
NGC4254*	184.706802	14.416412	16.8	10.47	False	5.2	3.8
NGC4293*	185.303467	18.382574	16.0	10.44	True	0.3	4.8

Table 2.1 – continued on next page

Table 2.1 – continued from previous page

Galaxy	RA (°)	Dec (°)	Distance (Mpc)	$\log(M_\star)$	Bar	T	R_e (kpc)
NGC4298*	185.386505	14.606110	16.8	10.04	False	5.1	3.3
NGC4303*	185.478882	4.473744	17.6	10.61	True	4.0	4.5
NGC4321*	185.728867	15.822304	15.2	10.64	True	4.0	6.2
NGC4424*	186.798203	9.420637	16.4	9.82	True	1.3	2.9
NGC4457*	187.245926	3.570620	15.6	10.39	True	0.3	1.3
NGC4496A*	187.913544	3.939608	14.9	9.54	True	7.4	3.7
NGC4535*	188.584595	8.197973	15.8	10.43	True	5.0	6.8
NGC4536*	188.612778	2.188243	15.2	10.14	True	4.3	3.2
NGC4540*	188.711929	15.551724	16.8	9.69	True	6.2	2.2
NGC4548*	188.860245	14.496331	16.2	10.64	True	3.1	5.3
NGC4569*	189.207596	13.162875	16.8	10.78	True	2.4	6.1
NGC4571*	189.234924	14.217327	14.9	9.99	False	6.4	3.9
NGC4579*	189.431381	11.818217	16.8	10.88	True	2.8	4.3
NGC4654*	190.985748	13.126715	16.8	10.21	True	5.9	4.1
NGC4689	191.939896	13.762724	16.8	10.17	False	4.7	4.5
NGC4731*	192.755035	-6.392839	12.4	9.42	True	5.9	5.9
NGC4781*	193.599167	-10.537116	15.3	9.74	True	7.0	2.6
NGC4826*	194.181839	21.683083	4.4	10.18	True	2.2	1.5
NGC4941*	196.054611	-5.551536	14.0	10.01	True	2.1	2.8
NGC4951*	196.282135	-6.493824	12.0	9.50	True	6.0	1.6
NGC5042*	198.879196	-23.983883	12.6	9.54	True	5.0	2.9
NGC5068*	199.728073	-21.038744	5.2	9.32	True	6.0	2.3
NGC5128	201.358688	-43.016083	3.6	10.89	False	-2.1	4.5
NGC5134*	201.327255	-21.134195	18.5	10.27	True	2.9	2.1
NGC5248*	204.383362	8.885195	12.7	10.14	True	4.0	2.5
NGC5530	214.613800	-43.388260	11.8	9.99	True	4.2	2.5
NGC5643	218.169907	-44.174610	11.8	10.06	True	5.0	3.2
NGC6300	259.247803	-62.820549	13.1	10.31	True	3.1	3.7
NGC6744*	287.442078	-63.857540	11.6	10.81	True	4.0	9.9
NGC7456*	345.543060	-39.569412	7.9	8.93	False	6.0	2.1
NGC7496*	347.447021	-43.427849	18.7	9.83	True	3.2	3.1

Table 2.1: Basic properties of the 72 galaxy sample. Note that $M_\star$ is stellar mass in units of $M_\odot$; T refers to the Hubble stage T; and R_e is the effective radius of the galaxy, determined from WISE 1 maps from the z0MGS project (Sun et al., in prep.; Leroy et al., accepted).

* Galaxies with all required data that are part of the final 55-galaxy set.

The PHANGS survey uses all three ALMA arrays: the 12m array, 7m array, and total power array. For this work, we focus on data produced from combining

the short spacing array (7m) and a total power telescope (12m), yielding CO(2-1) spectral cubes with angular resolutions of around $6''$ to $8''$, dependent on location and observing track length.

Compared to data that involves the main array (12m), the combination of short spacing array and total power telescope data (hereafter referred to as "7m+tp") boasts better spatial coverage than the main array data at the cost of resolution. These data are preferred for our analysis, as our work with DISKFIT (Section 3.1) prioritizes coverage over resolution.

The raw interferometer data is calibrated and then converted to image data via a process involving inverse Fourier transform and running a deconvolution algorithm. A signal mask (i.e. a mask that allows data from wherever there is expected to be emission) and multiscale cleaning (i.e. tweaking the inverse-Fourier-transformed "dirty" image such that its Fourier transform more closely matches the original raw data) are applied to stabilize this deconvolution process. These images are then combined with the data from the total power telescope (if available; Herrera et al., submitted) using the FEATHER algorithm. However, the precise details of the process are beyond the scope of this thesis.

This process returns a set of data cubes, which are essentially maps of each galaxy with a spectrum at each pixel (corresponding to line-of-sight velocities as calculated from the Doppler formula) with a velocity resolution of 2.5 km s^{-1} and a typical noise level of ~ 10 mK. Noise is estimated empirically from signal-free regions (and velocities) of the cube, and signal is identified as outliers relative to this noise model. This is done in a two-stage masking algorithm, where all emission with peak brightness above $T_B > 5\sigma$ (where σ is the local standard deviation of the noise distribution) is identified, and the environmental mask is then dilated such that emission connected spatially or spectrally to this peak is treated as signal. The current "Version 3.3" PHANGS release has data split into either "broad" or "strict" masking categories depending on how strict this particular step was; with the "broad" maps having wider coverage at the cost of more noise compared to the "strict" maps.

After the environmental mask is applied to the data cubes, properties such as

the integrated intensity ($W_{\rm CO}$, or "moment 0") and velocity centroids ($V_{\rm LoS}$, or "moment 1") of the emission distribution along each line of sight (pixel) can be measured, as:

$$W_{\rm CO} = \sum_i T(v_i) dv \ , \tag{2.1}$$

and

$$V_{\rm LoS} = \frac{1}{W_{\rm CO}} \sum_i v_i T(v_i) dv \ , \tag{2.2}$$

where $T(v)$ refers to the temperature across the spectrum, and v can be thought of as the spectral axis converted to a line-of-sight velocity through the Doppler formula. In addition, the velocity dispersion $\sigma_{\rm g}$ at each pixel can be estimated using the "equivalent width" method (which is the minimum data-driven model, compared to simply estimating $\sigma_{\rm g}$ as being a constant ~ 10 km/s or so), as follows:

$$\sigma_{\rm g} = \frac{W_{\rm CO}}{\sqrt{2\pi T_{\rm peak}}} \ , \tag{2.3}$$

where $T_{\rm peak}$ is simply the peak temperature along each line of sight.

2.2 z0MGS Star Formation Rate Imaging

For the star formation rate maps in our analysis, we use data from the z=0 Multi-wavelength Galaxy Synthesis (z0MGS) project (Leroy et al., accepted). This data is a compilation of ultraviolet and infrared images from the GALEX and WISE satellites, respectively, that have matching angular resolutions of $7.5''$ and $15''$. For the purposes of our work, the near-ultraviolet (NUV; 231 nm), far-ultraviolet (FUV; 154 nm), and the infrared WISE 3 (W3; 12 μm) bands are available in $7.5''$ resolution for the majority of the primary PHANGS target galaxies. However, the infrared WISE 4 band (W4; 22 μm) is only available at $15''$ resolution. Details behind the z0MGS project and how the matching-resolution maps for each band are generated can be read about further in Leroy et al., accepted.

The star formation rate maps ($\Sigma_{\rm SFR}$, in $M_\odot$ kpc^{-2} yr^{-1}) can be obtained from simply combining the ultraviolet and infrared contributions. The NUV and WISE

3 maps can be combined as follows (Leroy et al., accepted):

$$\begin{aligned}\frac{\Sigma_{\rm SFR,\ NUV+W3}}{M_\odot\ {\rm yr}^{-1}\ {\rm kpc}^{-2}} &= \Sigma_{\rm SFR,\ NUV} + \Sigma_{\rm SFR,\ W3}, \\ &= 1.04\times10^{-1}\frac{I_{\rm NUV}}{\rm MJy\ sr^{-1}} \\ &\quad + 3.77\times10^{-3}\frac{I_{\rm W3}}{\rm MJy\ sr^{-1}}, \end{aligned} \tag{2.4}$$

where $I_{\rm NUV}$ and $I_{\rm W3}$ refer to the intensities of the NUV and W3 bands, respectively. Likewise, SFR as calculated from the FUV+W4 bands is:

$$\begin{aligned}\frac{\Sigma_{\rm SFR,\ FUV+W4}}{M_\odot\ {\rm yr}^{-1}\ {\rm kpc}^{-2}} &= \Sigma_{\rm SFR,\ FUV} + \Sigma_{\rm SFR,\ W4}, \\ &= 1.04\times10^{-1}\frac{I_{\rm FUV}}{\rm MJy\ sr^{-1}} \\ &\quad + 3.24\times10^{-3}\frac{I_{\rm W4}}{\rm MJy\ sr^{-1}}\ . \end{aligned} \tag{2.5}$$

The reason that we consider both combinations of SFR maps is that neither is perfect for our work: the WISE 3 band is dominated by polycyclic aromatic hydrocarbons and suffers from larger uncertainties due to being sensitive to both chemistry and other effects from the environment (Leroy et al., accepted), and the WISE 4 band (while being a reliable tracer of hot gas near young stars) of course has its aforementioned downside of lower resolution. In Section 2.3 we explain how this issue is circumvented.

2.3 Derived Data

We require the use of $\Sigma_{\rm SFR}$ and $\Sigma_{\rm mol}$ maps; that is, maps of star formation rate and molecular surface density. The latter is proportional to the integrated CO(2-1) intensity maps of the galaxies:

$$\Sigma_{\rm mol} = \alpha_{\rm CO}^{(2-1)} W_{\rm CO}\ , \tag{2.6}$$

where the $W_{\rm CO}$ intensity maps were obtained from 7m+tp (or, if data including contributions from the total power array is unavailable, 7m) spectral cube data, captured from ALMA by the PHANGS collaboration as described in Section 2.1; and $\alpha_{\rm CO}^{(2-1)}$ is the conversion factor from integrated CO(2-1) intensity to the molecular surface

density. We use an experimental method that approximates this conversion factor as being proportional to the metallicity throughout a galaxy (Sun et al., in prep.), which in turn can be described in terms of the oxygen abundance, $\log(\mathrm{O/H})$, such that:

$$Z/Z_{\odot} = 10^{\log(\mathrm{O/H})-\log(\mathrm{O/H})_{\odot}} \ . \tag{2.7}$$

The solar value of oxygen abundance is taken to be 8.69 (Sun et al., in prep.), and the oxygen abundance at the characteristic radius of each galaxy is:

$$12 + \log(\mathrm{O/H})_{R_{\mathrm{e}}} = a + b\,(\log(M_{\star}/M_{\odot}) - 8 - c)\,e^{-(\log(M_{\star}/M_{\odot})-8-c)} \ , \tag{2.8}$$

where $M_{\star}$ is the stellar mass of each galaxy (measured using the WISE 1 maps from the z0MGS project; Leroy et al., accepted), and parameters for the mass-metallicity relationship are calibrated to be $a = 8.73$, $b = 0.010$, and $c = 3.5$ (Sánchez et al., 2019). The oxygen abundance throughout each galaxy can then be calculated as:

$$12 + \log(\mathrm{O/H}) = \left(12 + \log(\mathrm{O/H})_{R_{\mathrm{e}}} + \alpha_{\log(O/H)}(R/R_{\mathrm{e}} - 1)\right) \ , \tag{2.9}$$

where $\alpha_{\log(O/H)} = -0.10$ dex/R_{e} (Sánchez et al., 2014). This gives metallicities throughout each galaxy according to Equation 2.7; producing a conversion factor that increases with radius throughout each galaxy.

Prior to obtaining the CO(2-1)-to-molecular conversion factor this way, we had used a simpler method for obtaining $\alpha_{\mathrm{CO}}^{(2-1)}$ in which we simply adopt a value of $6.2\frac{M_{\odot}/\mathrm{pc}^2}{\mathrm{K\ km\ s^{-1}}}$, from the Milky Way value of $\alpha_{\mathrm{CO}}^{(1-0)} = 4.35\frac{M_{\odot}/\mathrm{pc}^2}{\mathrm{K\ km\ s^{-1}}}$ and a common line ratio of CO(2-1)/CO(1-0)=0.7 (Utomo et al., 2018). The results of the main analysis and the model comparisons using this simplified method are presented in Appendix A.

As described in Section 2.2, our SFR maps (Σ_{SFR}, in $M_{\odot}\ \mathrm{kpc}^{-2}\ \mathrm{yr}^{-1}$) are obtained using WISE and GALEX data convolved to a common angular resolution from the z0MGS project. The SFR maps in hand are combinations of NUV and WISE 3 data, and combinations of FUV and WISE 4 data; however, the former has greater systematic error due to its infrared band being dominated by polycyclic aromatic hydrocarbons, and the latter's infrared band is only available in a lower

resolution. To circumvent this issue, our final calculated SFR maps combine the spatial structure of the $\Sigma_{\rm SFR,\ NUV+W3}$ data with the accuracy of the $\Sigma_{\rm SFR,\ FUV+W4}$ data by simply rescaling the former to the latter, as follows:

$$\Sigma_{\rm SFR,\ 7.5"} = \Sigma_{\rm SFR,\ NUV+W3,\ 7.5"} \times \frac{\Sigma_{\rm SFR,\ FUV+W4,\ 15"}}{\Sigma_{\rm SFR,\ NUV+W3,\ 15"}} \ . \tag{2.10}$$

Galaxies for which any of the NUV, FUV, W3, or W4 data are unavailable are not included in the main analysis. In addition, for the main analysis, the $W_{\rm CO}$ and $\Sigma_{\rm SFR}$ maps need to have the same resolution before calculations are done, so the SFR data and the cube data are convolved to a common physical scale of $750\ {\rm pc}$. This resolution is available for nearly all of the target galaxies, while also being close to the initial resolutions of the 7m+tp PHANGS data cubes and the $7.5''$ $\Sigma_{\rm SFR}$ maps. These restrictions yield a final main sample of 55 galaxies for which the primary analysis is conducted. However, as mentioned in Section 2, rotation curves and galactic parameter optimizations are still performed on the $V_{\rm LoS}$ maps for nearly the full set of initial PHANGS targets. Figure 2.1 displays a sample of the important maps in our analysis for NGC 4321 (with the $3.4\ \mu{\rm m}$ WISE 1 map, which is proportional to the the stellar surface density, included for comparison), and Section 3 provides details about the rotation curves and galactic parameter optimizations.

Finally, we project both $\Sigma_{\rm SFR}$ and $\Sigma_{\rm mol}$ to their face-on quantities using the inclination of the galaxies (Section 3):

$$\Sigma_{\rm SFR} = \ \Sigma_{\rm SFR,obs} \cos i \ , \tag{2.11}$$

$$\Sigma_{\rm mol} = \ \Sigma_{\rm mol,obs} \cos i \ . \tag{2.12}$$

2.4 Star Formation Law

Figure 1.1 shows the star formation law from Leroy et al. (2013), where $\Sigma_{\rm SFR}$ is shown to exhibit a clear linear proportionality with $\Sigma_{\rm mol}$ across 30 galaxies. Using our new PHANGS+z0MGS data for 55 galaxies, we present a recreation of this image with more "modern" data in Figure 2.2. Even with nearly double the number of galaxies across a wider range, these results show very strong agreement with the previous generation of star formation studies.

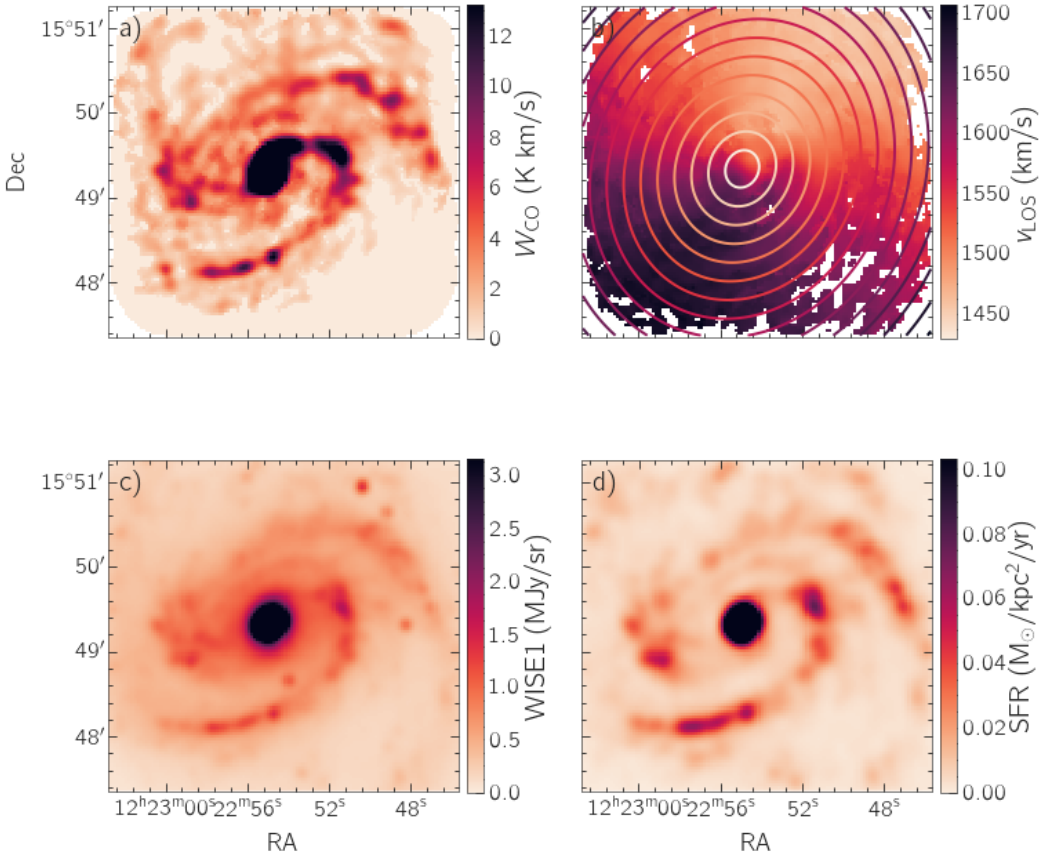

Figure 2.1: Example data for NGC 4321. (a) Integrated intensity for CO(2-1), (b) Velocity centroid surface with 1 kpc elliptical bins overlaid, (c) Stellar mass surface density (WISE 1), (d) Star formation rate map.

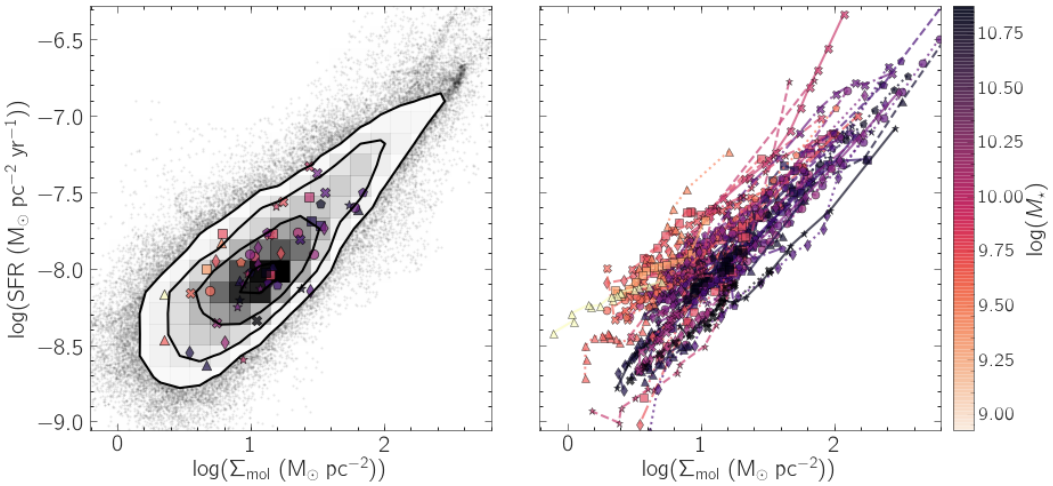

Figure 2.2: $\Sigma_{\rm SFR}$ versus $\Sigma_{\rm mol}$ for the 55-galaxy set, with data convolved to a common spatial scale of 750 pc. *Left:* 2D histogram of the combined $\Sigma_{\rm SFR}$ and $\Sigma_{\rm mol}$ maps, with markers indicating the median values for each galaxy. *Right:* Overall trend for $\Sigma_{\rm SFR}$ versus $\Sigma_{\rm mol}$ for each individual galaxy, in bins of equal number. The colours of lines and markers indicate stellar mass.

We also note that galaxies with low stellar mass tend to have higher SFRs per unit molecular mass.

Chapter 3

Rotation Curves

In this Chapter, we present the rotation curves, galaxy parameter fits, and subsequent analytical fits to the smoothed rotation curve model for each of our galaxies. Section 3.1 describes the use of the DISKFIT (Sellwood & Sánchez, 2010) algorithm to create a data-driven model for rotation curves.

Our main analysis involves the derivatives of rotation curves, and the DISKFIT output rotation curves are not smooth. Section 3.2 describes the process by which we fit a smooth rotation curve model to each galaxy, including correcting for the effects of beam-smearing. From the smooth models, we calculate the rotation curve derivatives in Section 3.3.

3.1 Rotation Curve Fitting with DISKFIT

To get a preliminary understanding of what the rotation curves of our 74-galaxy sample should look like, we generated rotation curves for these galaxies procedurally using the DISKFIT software (Sellwood & Sánchez, 2010), which attempts to solve for various galactic parameters (inclination, position angle, systemic velocity, noncircular flows, warping, etc.) using a line-of-sight velocity map as input. We used the integrated velocity centroid maps (or the "moment 1" maps, hereafter $V_{\rm LoS}$ (Equation 2.3), from the 7m ALMA data at their native resolution, prioritizing 7m+tp over 7m data wherever possible (see Section 2.3), for its advantage of high coverage compared to 12m data. While the primary analysis of this research uses PHANGS-ALMA data with "strict" masking to minimize the contribution of noise

(Section 2.1), our work with DISKFIT involved using velocity centroid maps with "broad" masking instead, which has greater coverage but also includes more noise than the alternative (Section 2.1). These preliminary rotation curves are being used as a basis of comparison for a more sophisticated approach to generating the curves (Lang et al., in prep.) and will be presented therein.

The basic galactic model used in DISKFIT is that of a flat disk with a fixed position angle that defines the line-of-nodes, and a constant inclination for all radial bins following Spekkens & Sellwood (2007):

$$\begin{aligned} V &= V_{\rm sys} + \sin i \left[V_t \cos\theta + \sum_{\rm m=1}^{\infty} V_{\rm m,t} \cos\theta \cos\left(m\theta + \theta_{\rm m,t}\right) \right. \\ &\quad \left. + V_r \sin\theta + \sum_{\rm m=1}^{\infty} V_{\rm m,r} \sin\theta \cos\left(m\theta + \theta_{\rm m,r}\right) \right] , \end{aligned} \tag{3.1}$$

where θ is the angle between the line of nodes and the position measured in the disk of the galaxy, i is the inclination, V_t is the circular rotation speed, V_r is the radial flow speed, and the harmonic sums account for the effects of non-circular motions with the amplitudes ($V_{\rm m,t}$, $V_{\rm m,r}$) and phases ($\theta_{\rm m,t}$, $\theta_{\rm m,r}$). Our basic model sets all of these terms to zero except V_t. DISKFIT supports fitting for warping and radial flows with V_r, $V_{m,t}$, and $V_{r,t} \neq 0$, but we opted to not use these settings for our dataset to keep the model relatively simple. Including either of these terms led to DISKFIT failing to properly converge when too many parameters were floating (or, in the case of bar fits, even with only one or two parameters floating), resulting in unsuccessful runs even on simplistic mock galaxies. DISKFIT responds especially poorly when there are holes in coverage as in the PHANGS data. With warping disabled, DISKFIT's "flat disk" model is essentially treated as a number of concentric rings with the same position angle, inclination, etc., with each ring having a different rotational velocity that DISKFIT outputs while attempting to optimize the parameters.

The required DISKFIT input for each galaxy includes the $V_{\rm LoS}$ map (with corresponding uncertainty map), initial guesses for each of the orientation parameters, a list of radii over which the code is run (i.e. the radii of each of the concentric

"rings" of the disk whose circular velocities are calculated), along with parameter-fit toggles. For most galaxies, the code was run over 25 evenly-spaced rings from the 0.40th to the 98.5th percentiles of galactocentric radius in the moment-1 map. However, certain galaxies with sparser or lower-resolution $V_{\rm LoS}$ maps required alterations such as a decreased number of rings, as there were often not enough data points involved in the calculation of each ring's rotational velocity to produce a meaningful result. Several galaxies also required changes to the considered minimum/maximum radii for several reasons, such as certain regions being considered extraneous for our purposes (e.g. nuclear regions that are decoupled from the disk), or the galaxy being ring-shaped.

The rotation curves and parameter fits were generated by procedurally running the DISKFIT optimization scheme over several iterations, with "good" parameter fits being saved and used in subsequent iterations while wildly-inaccurate fits were discarded. Initial guesses for the galaxies' kinematic position angles (PAs) and systemic velocities were simply pulled from the HyperLeda database (Paturel et al., 1989). HyperLeda was also initially used for the inclinations as well, but using inclinations from recent IR observations (Lang et al., in prep.; Salo et al., 2015) resulted in slightly better rotation curves.

However, many of these initial guesses for position angle needed significant altering before being fed into DISKFIT. HyperLeda only provides the *photometric* position angle rather than the kinematic PA that DISKFIT requires, so many of the queried PAs were off by roughly $180°$. In addition, a number of galaxies have nuclear regions that are decoupled from the rest of the disk region, and the online database may have provided parameters (PA, inclination, etc.) for a region that our work is less concerned with. For cases such as these, initial guesses for the kinematic PAs were simply approximated by eye from glancing at their $V_{\rm LoS}$ maps, and left for DISKFIT to optimize from there.

We used the central coordinates fixed to results from the recent work in IR imaging (Lang et al., in prep.), which greatly improved overall results relative to optically selected centres from HyperLeda.

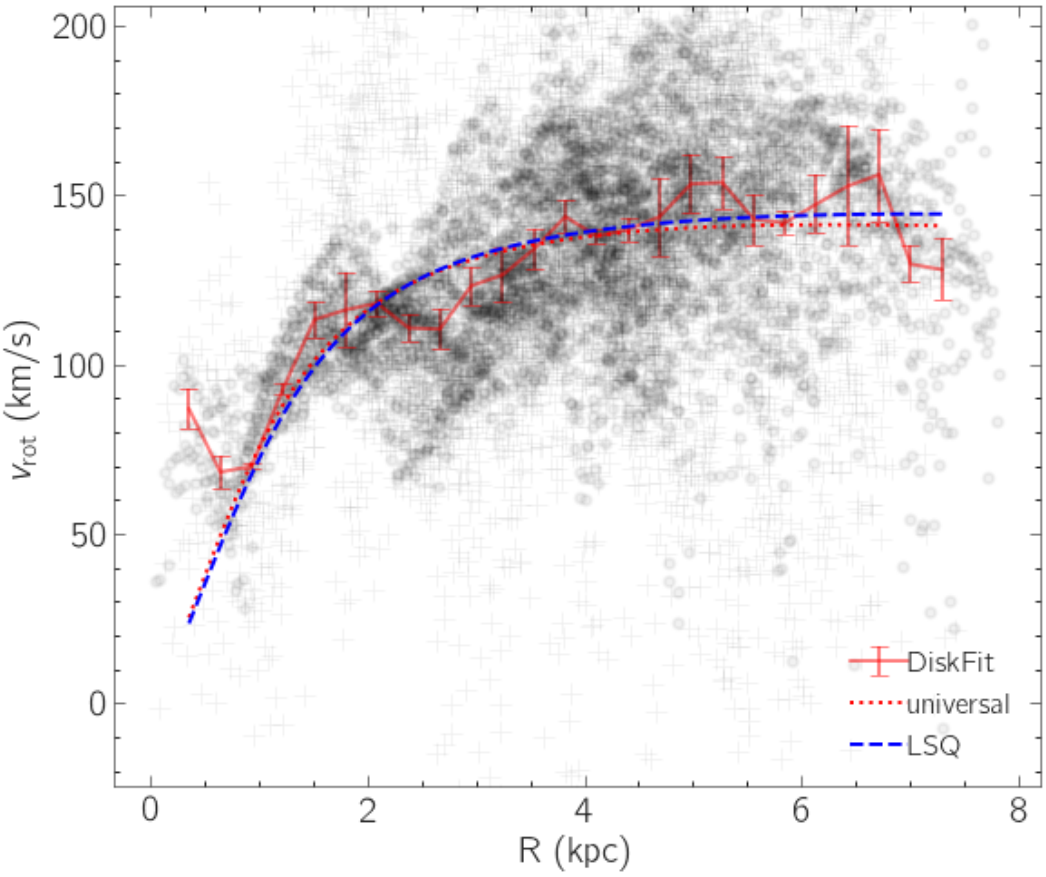

Figure 3.1: Rotation curve for NGC 0628 showing deprojected $V_{\rm LoS}$ data in grey (with dots indicating data near the major axis and "+" signs indicating other data), the DISKFIT rotation curve as a solid red line, the preliminary URC fit to this DISKFIT rotation curve as a dotted red line (for the sake of comparison), and the final LSQ-optimized URC model after the beam smearing correction as a dashed blue line.

Table 3.1 displays the final output parameters for each of the galaxies. Here, RA and Dec indicate each galaxy's central coordinates in decimal degrees; PA is the kinematic position angle (further improved from the DISKFIT output, as will be detailed in Section 3.2); i is the inclination; $V_{\rm sys}$ is the systemic velocity; and $V_{\rm max}$, $r_{\rm max}$, and A are parameters found when fitting the DiskFit rotation curve to the universal rotation curve model (see: Section 3.2). Galaxies with an asterisk (*) next to their name indicate that DISKFIT (which assumes a minimum inclination of $18.19°$, or a minimum ellipticity of 0.05) fitted the galaxy's inclination to something below this minimum. Some of these galaxies such as NGC0628 are face-on to

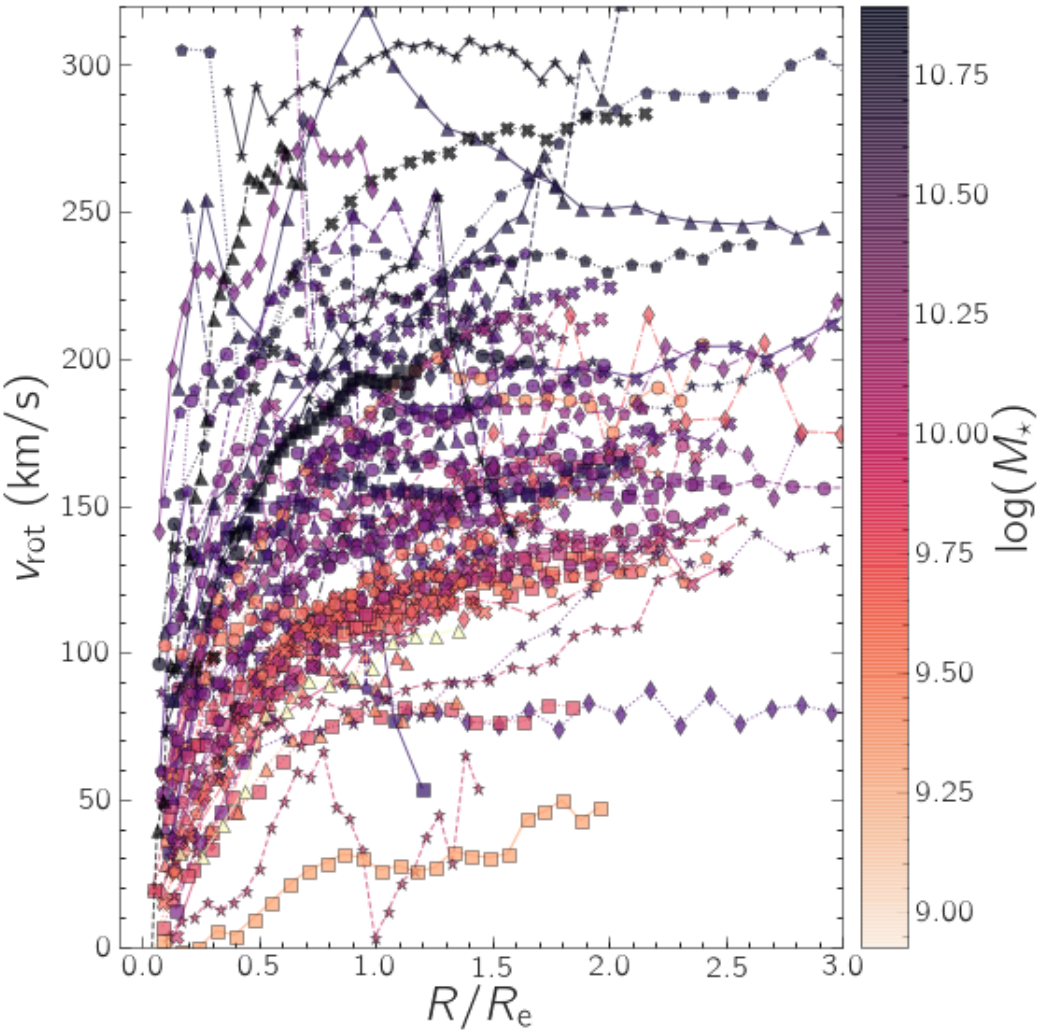

Figure 3.2: DiskFit output rotation curves for the 72-galaxy set, with colour indicating stellar mass $\log(M_\star)$. The radius values have been normalized by the effective radius R_e of each galaxy (defined by fits to the WISE1 stellar mass maps; Sun et al., in prep.). Note that NGC3239 and NGC4694 are excluded from this set, as NGC3239 is an irregular galaxy and NGC4694's data was insufficient for DISKFIT to converge on a reasonable fit. NGC1809 has a successful rotation curve fit and is used in the main analysis, but is also excluded from this figure by virtue of not having an available R_e value.

begin with, but several others were simply unable to obtain reasonable inclination fits from DISKFIT. To address this, we assumed the inclination derived from the study of the high resolution rotation curves for PHANGS galaxies derived in Lang et al. (in prep.), and ran one DISKFIT iteration with their inclination locked to this value.

In addition, Figure 3.1 displays the output DISKFIT rotation curve for a single galaxy (where the fits to a theoretical model will be discussed in further detail in Section 3.2). Figure 3.2 displays these raw DISKFIT output rotation curves for the entire sample of PHANGS target galaxies at once (minus NGC3239 and NGC4694), normalized with respect to their effective radii R_e (defined by fits to the WISE1 stellar mass maps; Sun et al., in prep.), with the colours of the curves indicating the galaxies' stellar masses ($\log(M_\star)$).

Galaxy	PA ($^\circ$)	Incl ($^\circ$)	$V_{\rm sys}$ (km s^{-1})	$V_{\rm max}$ (km s^{-1})	$R_{\rm max}$ (kpc)	A	Sample
IC1954	63	55	1041	94	2.25	1.16	clean
IC5273	234	48	1284	102	3.38	1.29	clean
IC5332*	67	24	695	77	3.09	1.43	clean
NGC0628*	21	9	651	105	2.53	1.12	marginal
NGC0685	99	32	1349	98	3.93	1.45	clean
NGC1087	357	37	1500	122	1.57	1.34	clean
NGC1097	124	40	1257	206	4.06	0.15	marginal
NGC1300	275	36	1544	138	8.92	0.67	marginal
NGC1317*	225	25	1932	113	1.11	2.61	marginal
NGC1365*	212	55	1603	224	6.38	1.06	marginal
NGC1385	183	38	1478	110	2.05	1.43	clean
NGC1433*	199	29	1056	160	2.47	1.46	marginal
NGC1511	293	58	1328	106	5.01	2.41	clean
NGC1512	261	73	867	152	9.80	0.68	all
NGC1546	147	66	1249	132	1.48	1.49	clean
NGC1559	247	52	1276	116	4.79	0.88	clean
NGC1566	221	23	1481	195	3.57	0.15	marginal
NGC1637	209	39	713	107	2.47	1.02	clean
NGC1672*	131	38	1319	111	2.57	1.12	clean
NGC1792	319	65	1174	119	2.87	1.14	clean
NGC1809	137	71	1288	82	2.58	1.16	marginal
NGC2090	192	67	900	122	1.47	1.24	clean
NGC2283	357	36	821	92	0.96	1.55	clean
NGC2566*	316	49	1595	120	3.00	1.25	marginal

Table 3.1 – continued on next page

Table 3.1 – continued from previous page

Galaxy	PA ($^\circ$)	i ($^\circ$)	$V_{\rm sys}$ (km s^{-1})	$V_{\rm max}$ (km s^{-1})	$R_{\rm max}$ (kpc)	A	Sample
NGC2775	157	41	1342	204	3.91	3.23	clean
NGC2835	0	46	867	88	1.90	1.14	clean
NGC2903	206	63	549	182	8.45	0.16	clean
NGC2997	110	31	1077	172	2.34	1.36	marginal
NGC3059*	347	19	1236	146	4.04	1.33	marginal
NGC3137	359	69	1084	87	2.47	1.20	clean
NGC3351	192	39	776	173	1.36	1.49	marginal
NGC3507*	58	25	971	116	3.22	1.18	clean
NGC3511	256	69	1096	97	2.34	1.12	clean
NGC3521	343	68	798	178	2.40	1.34	clean
NGC3596*	78	17	1188	125	2.01	3.72	clean
NGC3621	343	64	724	102	3.00	1.19	clean
NGC3626*	165	47	1481	190	1.26	2.16	clean
NGC3627	171	55	716	156	3.45	2.31	clean
NGC4207	121	30	614	121	2.59	3.65	marginal
NGC4254	68	29	2390	151	2.54	1.37	clean
NGC4293	56	73	929	107	2.86	1.08	marginal
NGC4298	315	56	1135	98	3.00	1.39	clean
NGC4303*	314	26	1557	122	2.57	1.46	clean
NGC4321	155	31	1575	168	4.48	1.18	clean
NGC4424	92	57	452	75	6.27	1.36	all
NGC4457	76	51	890	69	0.77	1.76	clean
NGC4496A	50	28	1723	100	4.16	1.73	clean
NGC4535	180	44	1956	124	4.13	0.88	marginal
NGC4536	304	65	1794	143	1.54	1.83	marginal
NGC4540	17	43	1285	65	2.05	1.73	clean
NGC4548*	137	38	485	152	1.67	1.97	marginal
NGC4569	18	52	-226	195	6.76	1.15	clean
NGC4571	218	28	343	106	1.92	1.18	clean
NGC4579	90	38	1516	204	4.51	0.15	marginal
NGC4654	124	55	1053	118	4.02	1.43	clean
NGC4689	164	38	1617	105	3.01	1.13	clean
NGC4731*	295	64	1476	58	4.32	0.87	marginal
NGC4781	287	55	1248	92	2.79	1.13	clean
NGC4826	293	36	408	193	0.33	1.32	clean
NGC4941	203	42	1115	175	4.29	1.43	marginal
NGC4951	91	65	1180	100	1.63	1.62	clean
NGC5042	190	41	1388	93	1.24	1.21	marginal
NGC5068	344	53	667	61	8.29	0.96	marginal
NGC5128	311	74	568	196	2.86	2.26	marginal
NGC5134*	319	26	1743	99	3.94	0.97	marginal

Table 3.1 – continued on next page

Table 3.1 – continued from previous page

Galaxy	PA ($^\circ$)	i ($^\circ$)	$V_{\rm sys}$ (km s^{-1})	$V_{\rm max}$ (km s^{-1})	$R_{\rm max}$ (kpc)	A	Sample
NGC5248	108	44	1165	136	1.18	1.53	marginal
NGC5530	306	58	1181	110	3.68	1.10	clean
NGC5643*	317	30	1191	136	2.27	1.22	clean
NGC6300	105	49	1104	138	2.28	1.25	clean
NGC6744	14	52	832	132	5.38	0.76	clean
NGC7456	15	52	1192	89	2.43	1.35	marginal
NGC7496	191	42	1638	74	3.40	1.06	clean

Table 3.1: Output DISKFIT parameters and LSQ-optimized URC parameters for each PHANGS target galaxy, using 7m $V_{\rm LoS}$ data. Note that the PA is the improved fit from the LSQ URC optimization, rather than the DISKFIT output.
* Galaxies whose DISKFIT inclinations fell below 18.19°. These inclinations were instead fixed to those from Lang et al. (in prep.).

Complications with DISKFIT

While DISKFIT was able to produce parameter fits and rotation curves for 72 of the galaxies, the quality of these rotation curves varied. There were a small handful of galaxies for which DISKFIT was unable to produce usable rotation curves, due to either large gaps or the overall sparseness of the $V_{\rm LoS}$ data. DISKFIT also has an unfortunate tendency to wildly overestimate inclinations in the former scenario (e.g. NGC1512).

Due to the variable results in rotation curve and parameter fits, the full set of all 74 target galaxies (72, excluding NGC3239 and NGC4694) was split into several samples based on the reliability of the DISKFIT output (see Figure 3.3 for an example). We will refer to these as the "all", "marginal", and "clean" samples, each being a superset of the latter. The "clean" sample refers to the 44 well-behaved galaxies that have stable parameter fits and a sensible, almost-ideal DISKFIT rotation curve; the "marginal" sample (70 galaxies, including the "clean" sample) includes those with good parameter fits and passable DISKFIT rotation curves (in the sense that they may exhibit some jaggedness discontinuities, but they are overall believable and largely match the $V_{\rm LoS}$ data); and the "all" sample (which contains the other two galaxies) simply refers to the full 72-galaxy set. Galaxies with the required 2D

data that are part of the "marginal" sample *and* have the required PHANGS and z0MGS data (Section 2) are used in the final analysis; galaxies outside this group are of course unusable either due to missing data or due to nonsensical rotation curve fits.

3.2 Analytic Rotation Curve Fits

After completing the DISKFIT analysis, we use the output galactic parameters (such as kinematic PA, inclination, systemic velocity, etc.) as the basis for generating a smooth rotation curve model for the galaxy, for the sake of smoothly describing each galaxy's underlying mass distribution, and for providing stable derivatives for the rotation curve. We evaluated cubic spline fits, the Brandt (1960) rotation curve, the simple exponential rotation curve used in Leroy et al. (2008), and the Universal Rotation Curve (URC) of Persic et al. (1996) (see Appendix C). We find that the URC model best reproduces most of the large-scale features in the rotation curves of the DISKFIT models, in particular it captures the significant fraction of rotation curves that are not monotonic.

The URC model is as follows:

$$V(R) = V_{\rm max}\left[(0.72 + 0.44\ln A)\,\frac{1.97x^{1.22}}{(x^2+0.78^2)^{1.43}} + 1.6\exp(-0.4A)\frac{x^2}{x^2+1.5^2A^2}\right]^{0.5} \tag{3.2}$$

for some $V_{\rm max}$, $R_{\rm max}$, and shape parameter A; where $x \equiv R/R_{\rm max}$.

With the DISKFIT rotation curves and the $V_{\rm LoS}$ maps (with corresponding error maps) available, a URC fit is generated for each galaxy by comparing the observed $V_{\rm LoS}$ data to a predicted 2D beam-sampled "model" velocity centroid map (from a floating set of URC parameters) projected into the plane of the sky using DISKFIT's output inclination, systemic velocity, and position angle. After the model URC is projected into the sky, we convolve this model centroid map with a Gaussian beam to match the resolution of the observed data, and optimize the parameters of the URC and the galaxy position angle using a least-squares approach (LSQ). We also attempted Markov-chain Monte Carlo sampling of the probability space but this

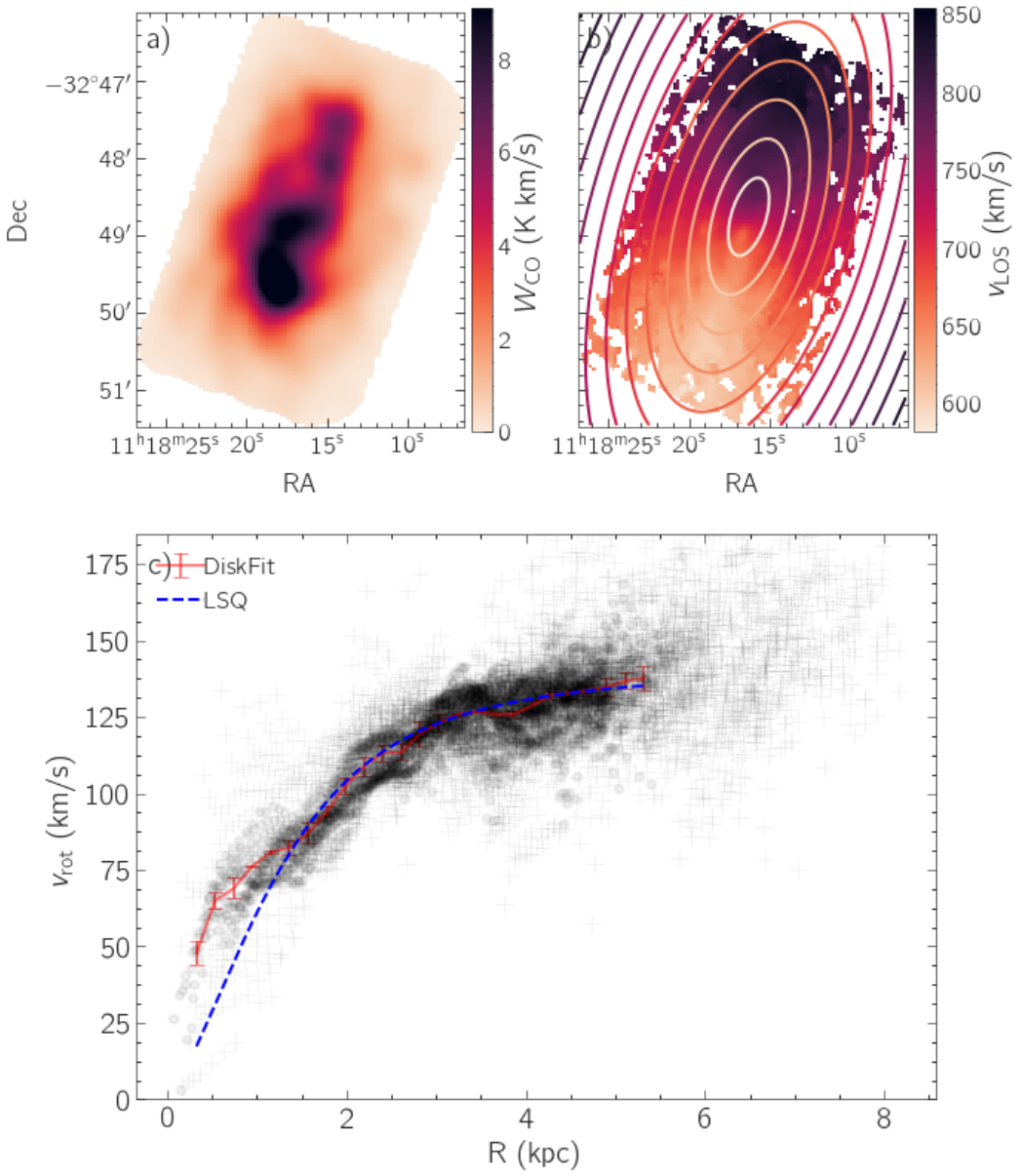

Figure 3.3: Example DISKFIT output for NGC3621. (a) Integrated CO(2-1) intensity (b) Integrated line-of-sight velocity with galactocentric radius contours overlaid (c) Fitted rotation curve of the galaxy, where the deprojected $V_{\rm LoS}$ data is displayed in grey (with dots indicating data near the major axis and "+" signs indicating other data), the DISKFIT rotation curve is displayed as a solid red line, and the dashed line indicates the final LSQ-optimized URC model after the beam smearing correction. This is an example of a well-behaved galaxy that would fall into the "clean" grouping.

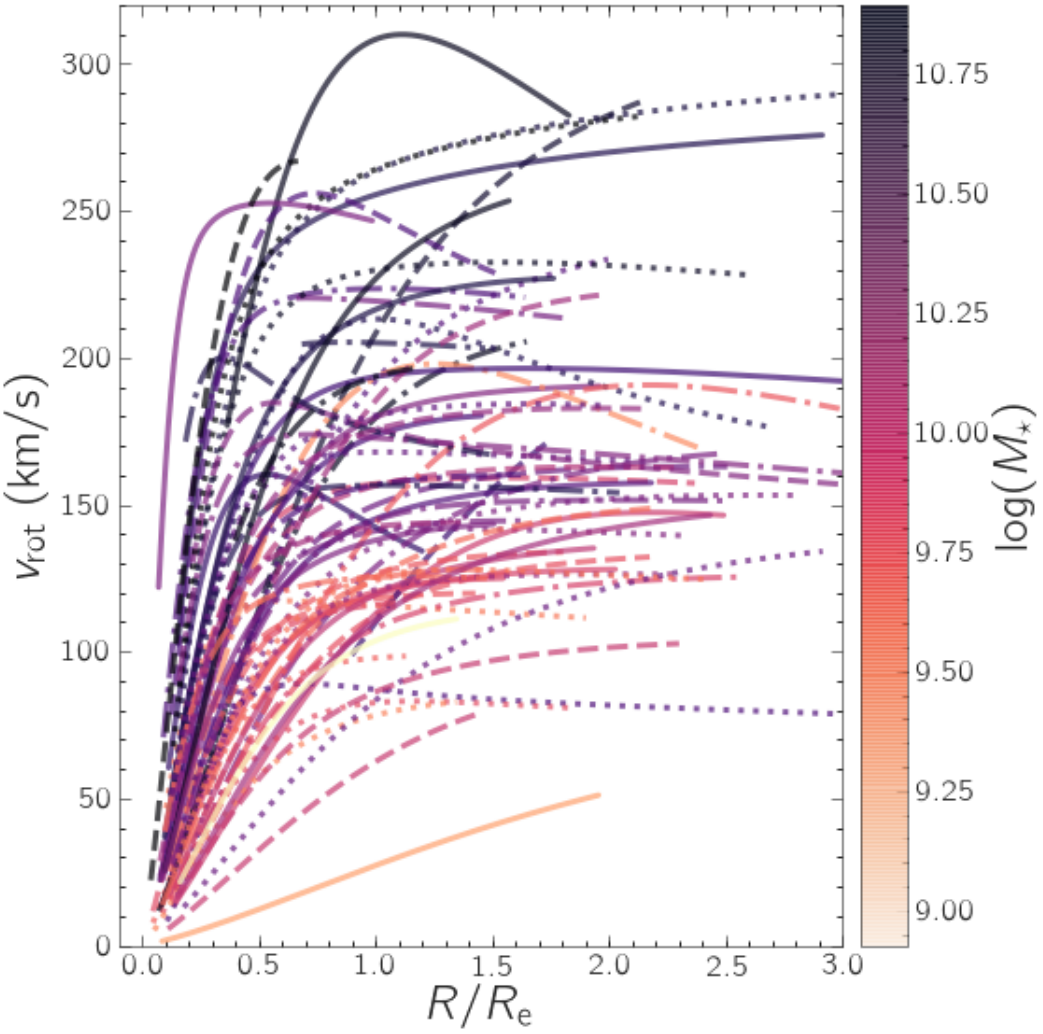

Figure 3.4: LSQ-optimized URC fits to the rotation curves in Figure 3.2 for the full 72-galaxy set, with the beam smearing correction. Colours indicate stellar mass $\log(M_\star)$, and radius values have been normalized by the effective radius R_e of each galaxy (defined by fits to the WISE1 stellar mass maps; Sun et al., in prep.). Note that NGC3239 and NGC4694 are excluded from this set, as NGC3239 is an irregular galaxy and NGC4694's data was insufficient for DISKFIT to converge on a reasonable fit. NGC1809 has a successful rotation curve fit and is used in the main analysis, but is also excluded from this figure by virtue of not having an available R_e value.

proved to have a high rate of unstable URC fits compared to just leaving the LSQ results alone, so this method was eventually scrapped.

Figure 3.1 and Figure 3.3c show the DISKFIT output rotation curve and the URC-fitted rotation curves of individual galaxies on the deprojected $V_{\rm LoS}$ data (that is, $(V_{\rm LoS} - V_{\rm sys})/(\sin(i)\ \cos(\phi))$, where i is the inclination and ϕ refers to the angle from the major axis in the disk plane). In addition, Figure 3.4 displays the final LSQ-optimized URC fits for all of the galaxies, coloured based on their respective stellar mass values as in Figure 3.2.

3.3 Rotation Curves and Shear

With the URC fits finalized, these smoothed rotation curves were then used to calculate the important rotation curve derivatives (e.g. β, A, κ).

There are a variety of parameterizations that can be used to quantify rotational shear. Common parameterizations include the Oort A parameter,

$$A = \frac{1}{2}\left(\frac{V}{R} - \frac{dV}{dR}\right); \tag{3.3}$$

the epicyclic frequency, κ, which is closely tied to the line width from galactic motions, and is proportional to the approximate galactic shear across a cloud-sized region (Meidt et al., 2018):

$$\kappa^2 = 2\left(\frac{V^2}{R^2} + \frac{V}{R}\frac{dV}{dR}\right); \tag{3.4}$$

and the β parameter (i.e. the logarithmic derivative of the curve),

$$\beta = \frac{d\ln\ V}{d\ln\ R}. \tag{3.5}$$

As mentioned in Section 1.5, our main analysis involves the β parameter, as it is a data-driven measure of the differential rotation throughout a galaxy.

To help illustrate, galactic regions with low β (near 0, i.e. flat rotation curve) will have high shear due to objects at slightly different radii orbiting at different angular velocities, whereas regions with $\beta \sim 1$ (i.e. solid body rotation) will have lower shear due to everything moving at the same angular velocity (Suwannajak

et al., 2014). The values of β will typically fall between 0 and 1, with the expected behaviour being that it should be near 1 at low radii (where the rotational velocity increases fairly uniformly, and shear is therefore low), and it should decrease to near 0 at higher radii (where the rotation curve flattens out, and shear therefore increases). In a similar vein, $A \sim 0$ for solid-body rotation, and is $A = \frac{V}{2R}$ for a flat rotation curve.

To illustrate how these shear parameterizations behave overall across a large set of galaxies, Figure 3.5 shows the β, A, and κ plotted against radius for the 70 galaxies in the "marginal" sample (recall that the marginal sample includes all "clean" rotation curves as well).

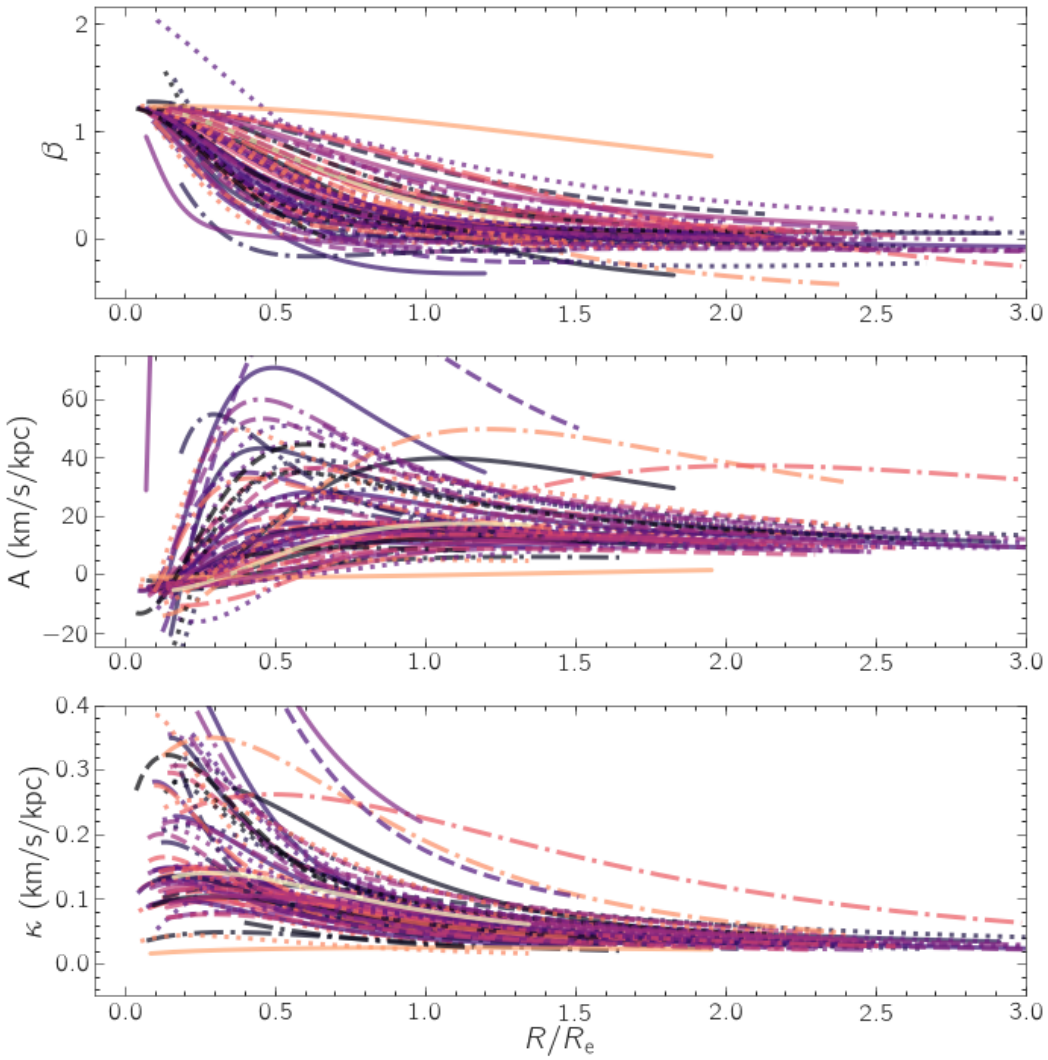

Figure 3.5: From top to bottom: β vs. R, Oort A vs. R, and κ vs. R; for the 70 galaxies in the "marginal" sample. Colours indicate the stellar mass of each galaxy, consistent with Figure 3.4. The radius values has been normalized by the effective radius R_e of the galaxy. NGC1809 is excluded from this figure by virtue of not having an available R_e value.

Chapter 4

Results

The finalized star formation rate and molecular surface density maps (detailed in Section 2.3) can be used to calculate useful quantities such as the molecular depletion time throughout each galaxy,

$$\tau_{\rm dep} = \frac{\Sigma_{\rm mol}}{\Sigma_{\rm SFR}} \, , \tag{4.1}$$

which is the approximate timescale for molecular gas to deplete itself through a constant rate of star formation. As mentioned in Section 1.5, another important timescale to consider is the molecular free-fall time,

$$\tau_{\rm ff} = \sqrt{\frac{3\pi}{32 G \rho_0}} \, , \tag{4.2}$$

the approximate time over which a cloud of molecular gas collapses into stars (and thus can be seen as the characteristic timescale over which ISM evolves due to gravitational effects); where ρ_0 is the initial volume density of this molecular gas. However, it is difficult to find this 3-dimensional volume density when looking at a 2-dimensional image of a galaxy from very far away, so for the purposes of this research, we will simply approximate molecular clouds as having a constant thickness of $\sim 100 \, \rm pc$, characteristic of the molecular gas in the Milky Way (Utomo et al., 2018):

$$\tau_{\rm ff} \sim \sqrt{\frac{3\pi}{32 G} \frac{100 \rm pc}{\Sigma_{\rm mol}}} \, . \tag{4.3}$$

The final relevant timescale is the orbital time,

$$\tau_{\rm orb} = \frac{2\pi R}{V} \, , \tag{4.4}$$

which can be thought of as the approximate timescale over which large-scale dynamical effects in a galaxy take effect; where V is the circular rotational velocity of the galaxy. When comparing depletion time with rotational shear, normalizing the depletion time with respect to these two timescales across each galaxy may help illuminate a trend between the quantities; namely, we might observe a trend between the shear and regions where depletion time is much higher/lower than the ISM-evolving/dynamical-evolving timescales.

4.1 Main Results

These results are for the 53 galaxies in the intersection between the 55 galaxies that have the required PHANGS and z0MGS data (Section 2) and the 70 galaxies having rotation curves of at least "marginal" quality (Section 3.1)

The molecular depletion time is plotted against β parameters in Figure 4.1, with the left panel displaying a 2D histogram comparing the two properties across the entire sample at once with each beam-sampled[1] line-of-sight datum weighted equally, and with markers indicating the median values for each galaxy. The markers are colour-coded to indicate the stellar mass of the galaxy. The right panel displays the averages of these properties (in radial bins of equal numbers of data) across each of these individual galaxies. Overall, there is a lot of spread between the two quantities, and there does not appear to be any sort of immediate trend between $\tau_{\rm dep}$ and β.

Figure 4.2 shows depletion time normalized with free-fall time plotted against β in a similar manner. While there is still much spread between the two axes, there appears to be a stronger correlation in this case.

Figure 4.3 shows depletion time normalized with orbital time plotted against β, also exhibiting a moderate correlation between the two quantities.

The correlations between the three pairs of properties are summarized in Figure 4.4, which show histograms of the Spearman rank correlation coefficients (with

[1]Here, "beam-sampled" means that the data only include samples from an image sampled on a grid with spacing of one synthesized beam, rather than every pixel in the image. We do this because interferometer images are typically oversampled.

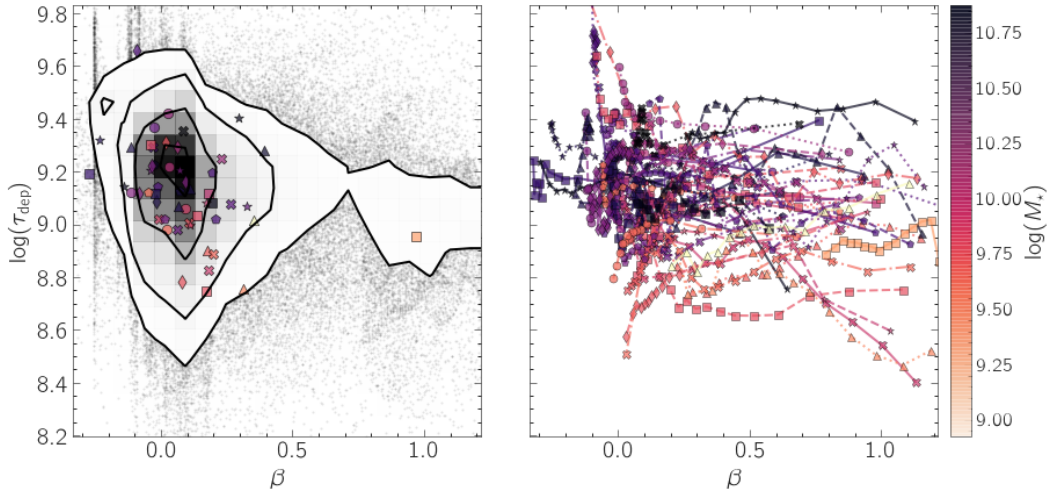

Figure 4.1: $\tau_{\rm dep}$ versus β for the "marginal" galaxies in the dataset. *Left:* 2D histogram of the combined $\tau_{\rm dep}$ and projected β maps over this sample, with the markers indicating the median values of each galaxy, and the colours of these markers indicating the stellar masses of the galaxy. *Right:* Overall trend of $\tau_{\rm dep}$ versus β for each galaxy, in radial bins with equal numbers of data. There does not appear to be a correlation between the two properties.

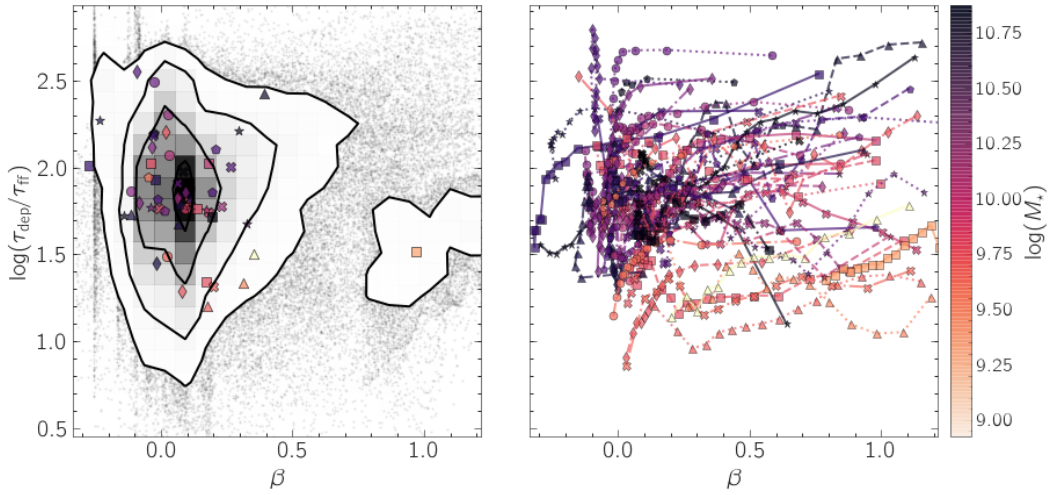

Figure 4.2: $\tau_{\rm dep}/\tau_{\rm ff}$ versus β for the "marginal" galaxies in the dataset. *Left:* 2D histogram of the combined $\tau_{\rm dep}/\tau_{\rm ff}$ and projected β maps over this sample, with the markers indicating the median values of each galaxy, and the colours of these markers indicating the stellar masses of the galaxy. *Right:* Overall trend of $\tau_{\rm dep}/\tau_{\rm ff}$ versus β for each galaxy, in radial bins with equal numbers of data. There appears to be a weak correlation between the two properties.

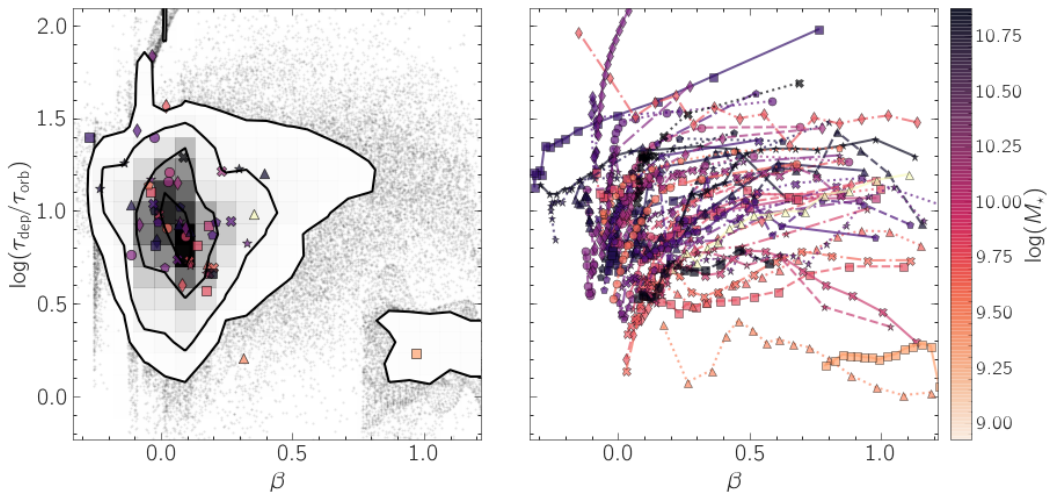

Figure 4.3: $\tau_{\rm dep}/\tau_{\rm orb}$ versus β for the "marginal" galaxies in the dataset. *Left:* 2D histogram of the combined $\tau_{\rm dep}/\tau_{\rm orb}$ and projected β maps over this sample, with the markers indicating the median values of each galaxy, and the colours of these markers indicating the stellar masses of the galaxy. *Right:* Overall trend of $\tau_{\rm dep}/\tau_{\rm orb}$ versus β for each galaxy, in radial bins with equal numbers of data. The two properties appear to be correlated, although this is likely due to an intrinsic anticorrelation between $\tau_{\rm orb}$ and β.

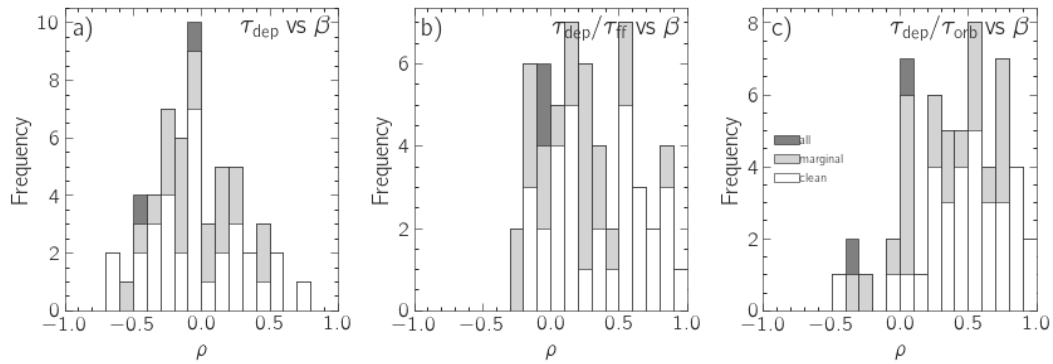

Figure 4.4: Histograms showing the Spearman rank coefficients for each galaxy across our main sample, illustrating observed correlations for: (a) $\tau_{\rm dep}$ versus β, (b) $\tau_{\rm dep}/\tau_{\rm ff}$ versus β, (c) $\tau_{\rm dep}/\tau_{\rm orb}$ versus β.

$\rho = 1$ indicating a correlation, -1 indicating an anticorrelation, and 0 indicating neither) between each pair of quantities for each individual galaxy, in each of the samples ("all", "marginal", and "clean"). As previously mentioned, no immediate trend is observed between $\tau_{\rm dep}$ and β. On the other hand, $\tau_{\rm dep}/\tau_{\rm ff}$ versus β shows a somewhat more significant correlation, and $\tau_{\rm dep}/\tau_{\rm orb}$ versus β displays a clearer correlation than the other two cases. However, we do caution that:

$$\tau_{\rm ff} \propto \Sigma_{\rm mol}^{-0.5} \, , \tag{4.5}$$

and

$$\begin{aligned} \beta =& \frac{d\ln(V)}{d\ln(R)} \, , \\ =& \frac{\tau_{\rm orb}}{2\pi} \frac{dV}{dR} \, . \end{aligned} \tag{4.6}$$

That is, the trends observed in Figures 4.2 and 4.3 may involve intrinsic correlations of the quantities being compared rather than real results from the data. Specifically, for the latter case, an intrinsic anticorrelation is expected between β and $\tau_{\rm orb}$ overall, as both are direct functions of a rotation curve, and $\tau_{\rm orb}$ tends to increase with radius while β tends to decrease with radius for a typical rotation curve.

4.2 Comparison to Models

Here, we show the results of testing the star formation models described in Section 1.4. As with the main analysis, this is performed using the 53 galaxies that have all required PHANGS and z0MGS data while also producing at least "marginal" rotation curves.

The "constant H_2 star formation efficiency" model, which naively predicts a constant depletion time, is tested by simply comparing $\tau_{\rm dep}$ with β and observing whether a correlation exists (Figure 4.1). As stated in the previous section, the two quantities do not exhibit any clear correlation, although we do note that depletion times tend to vary among galaxies by roughly an order of magnitude.

Figure 4.5 shows the depletion time plotted against Q. A moderate anticorrelation is observed between the two properties, contrary to what was predicted in

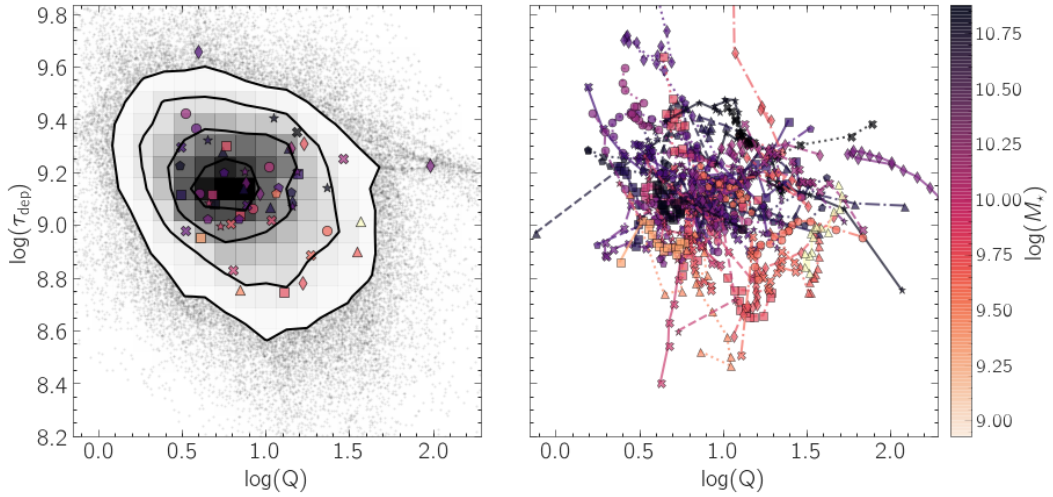

Figure 4.5: $\tau_{\rm dep}$ versus Q for the "marginal" galaxies in the dataset. *Left:* 2D histogram of the combined $\tau_{\rm dep}$ and projected Q maps over this sample, with the markers indicating the median values of each galaxy, and the colours of these markers indicating the stellar masses of the galaxy. *Right:* Overall trend of $\tau_{\rm dep}$ versus Q for each galaxy, in radial bins with equal numbers of data. The quantities appear to be anticorrelated, contrary to predictions; however, this is likely due to an intrinsic anticorrelation between the two properties, rather than a real result from data.

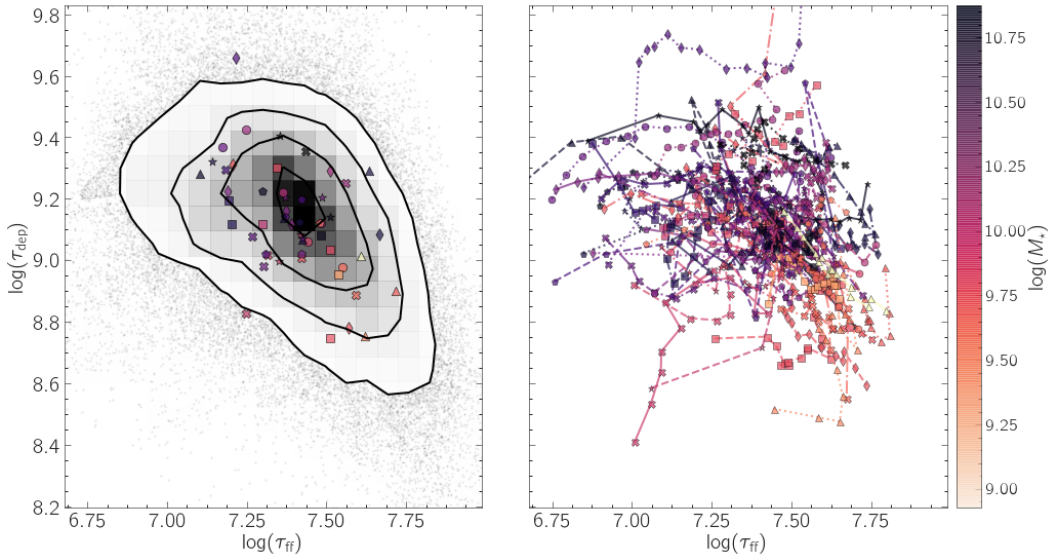

Figure 4.6: $\tau_{\rm dep}$ versus $\tau_{\rm ff}$ for the "marginal" galaxies in the dataset. *Left:* 2D histogram of the combined $\tau_{\rm dep}$ and $\tau_{\rm ff}$ maps over this sample, with the markers indicating the median values of each galaxy, and the colours of these markers indicating the stellar masses of the galaxy. *Right:* Overall trend of $\tau_{\rm dep}$ versus $\tau_{\rm ff}$ for each galaxy, in radial bins with equal numbers of data. There is a clear anticorrelation between the two quantities, opposite to what is predicted in the "disk free fall time with fixed scale height" model.

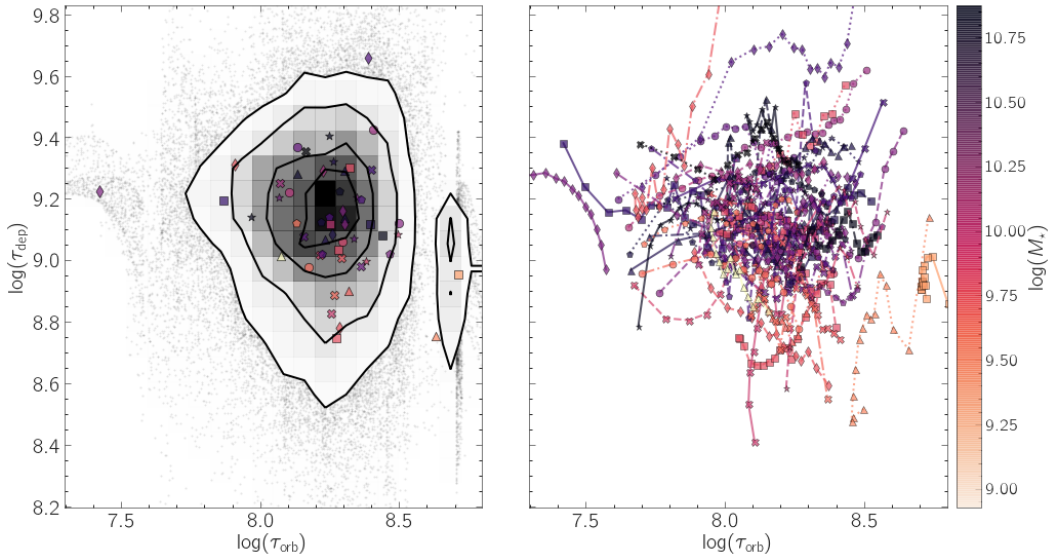

Figure 4.7: $\tau_{\rm dep}$ versus $\tau_{\rm orb}$ for the "marginal" galaxies in the dataset. *Left:* 2D histogram of the combined $\tau_{\rm dep}$ and $\tau_{\rm orb}$ maps over this sample, with the markers indicating the median values of each galaxy, and the colours of these markers indicating the stellar masses of the galaxy. *Right:* Overall trend of $\tau_{\rm dep}$ versus $\tau_{\rm orb}$ for each galaxy, in radial bins with equal numbers of data. There does not appear to be a correlation between the two properties.

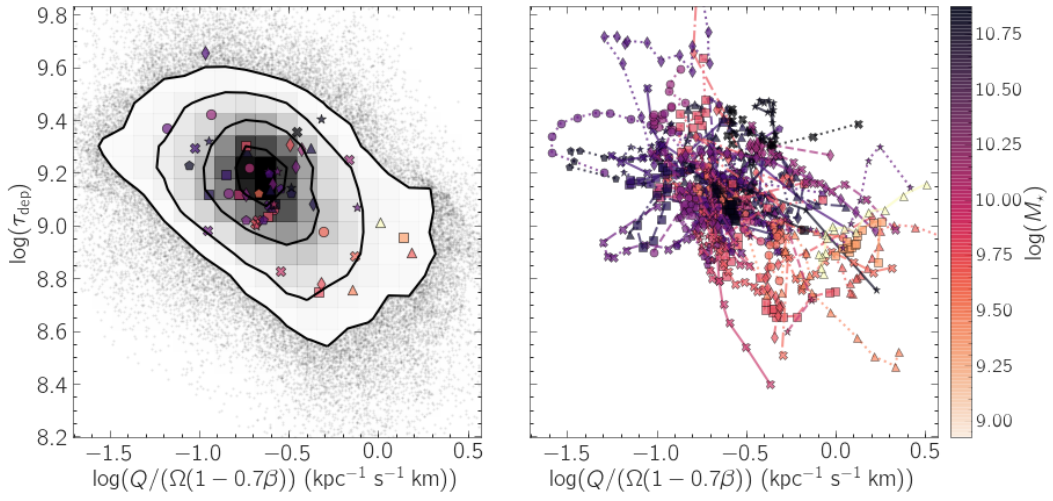

Figure 4.8: $\tau_{\rm dep}$ versus $Q/\left(\Omega(1-0.7\beta)\right)$ for the "marginal" galaxies in the dataset. *Left:* 2D histogram of the combined $\tau_{\rm dep}$ and $Q/\left(\Omega(1-0.7\beta)\right)$ maps over this sample, with the markers indicating the median values of each galaxy, and the colours of these markers indicating the stellar masses of the galaxy. *Right:* Overall trend of $\tau_{\rm dep}$ versus $Q/\left(\Omega(1-0.7\beta)\right)$ for each galaxy, in radial bins with equal numbers of data. There is an anticorrelation between the two quantities, contrary to what is predicted in Tan (2000)'s "GMC collision" model. However, this is likely due to a strong intrinsic anticorrelation between $\tau_{\rm dep}$ and Q.

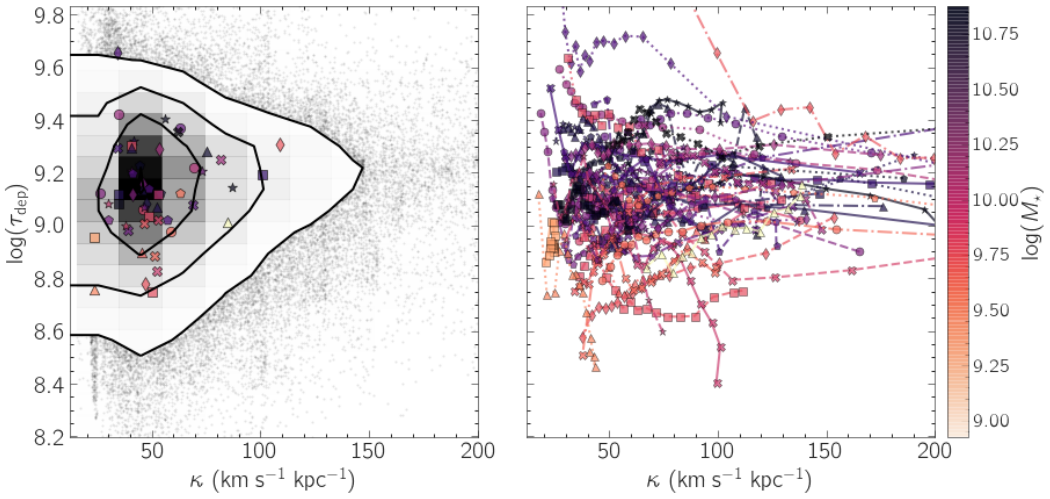

Figure 4.9: $\tau_{\rm dep}$ versus κ for the "marginal" galaxies in the dataset. *Left:* 2D histogram of the combined $\tau_{\rm dep}$ and κ maps over this sample, with the markers indicating the median values of each galaxy, and the colours of these markers indicating the stellar masses of the galaxy. *Right:* Overall trend of $\tau_{\rm dep}$ versus κ for each galaxy, in radial bins with equal numbers of data. There does not appear to be a correlation between the two quantities.

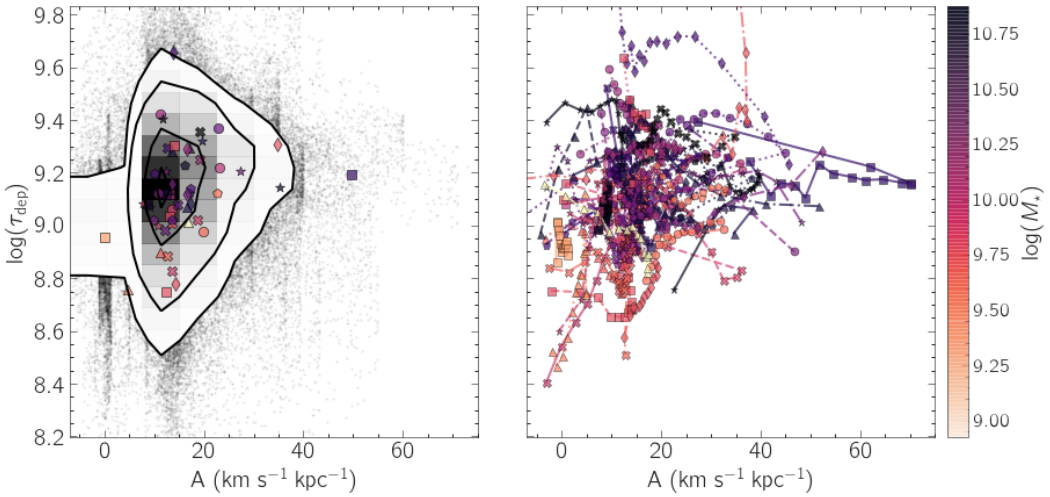

Figure 4.10: $\tau_{\rm dep}$ versus A for the "marginal" galaxies in the dataset. *Left:* 2D histogram of the combined $\tau_{\rm dep}$ and A maps over this sample, with the markers indicating the median values of each galaxy, and the colours of these markers indicating the stellar masses of the galaxy. *Right:* Overall trend of $\tau_{\rm dep}$ versus A for each galaxy, in radial bins with equal numbers of data. There does not appear to be a correlation between the quantities.

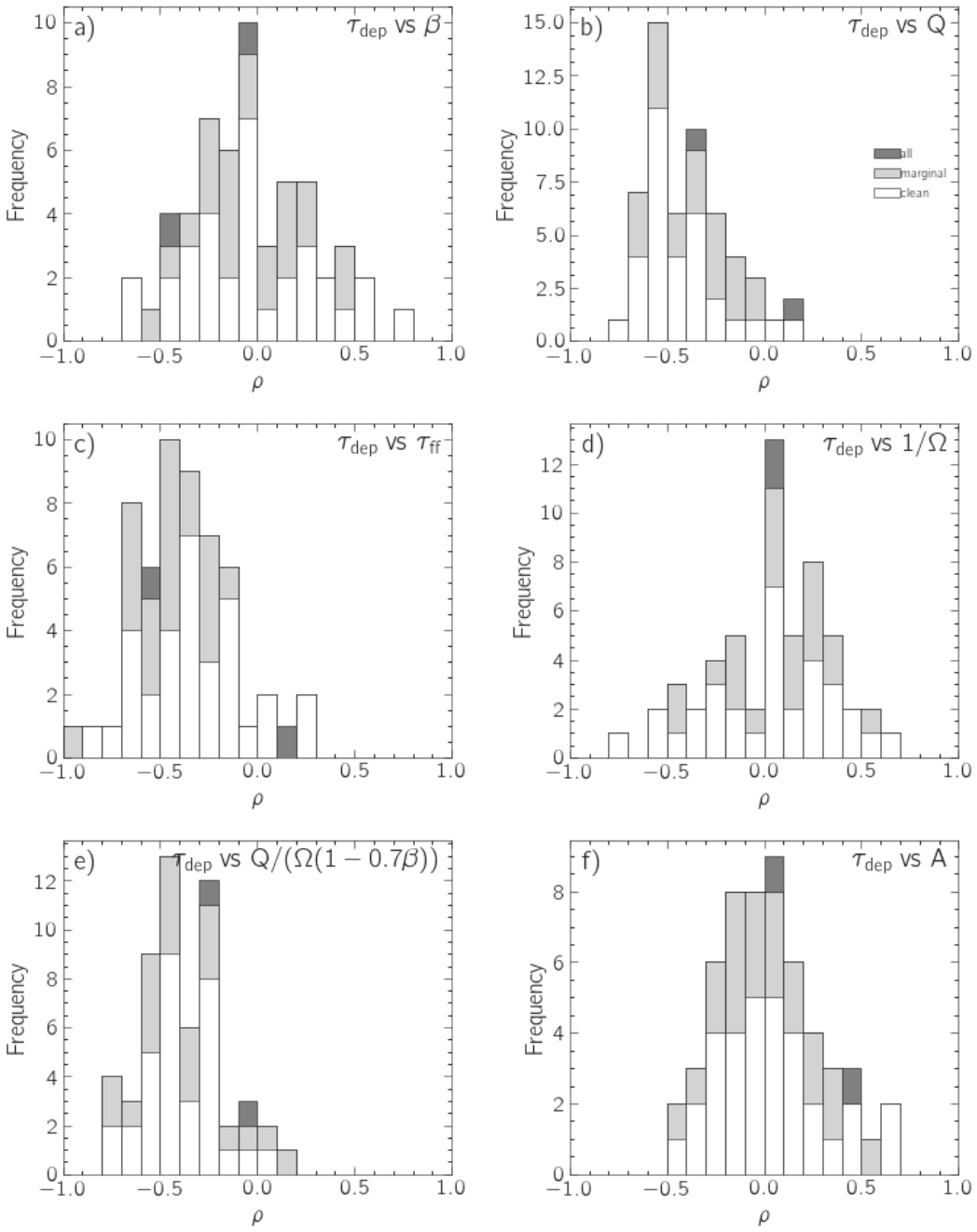

Figure 4.11: Histograms showing the Spearman rank coefficients for each galaxy across each sample, illustrating observed correlations for each tested model: (a) $\tau_{\rm dep}$ versus β. (b) $\tau_{\rm dep}$ versus the Toomre Q, which are expected to show a correlation according to Section 1.4.2. (c) $\tau_{\rm dep}$ versus $\tau_{\rm ff}$, which are expected to display a correlation according to Kennicutt (1998) assuming constant scale height. (d) $\tau_{\rm dep}$ versus $1/\Omega$ (proportional to $\tau_{\rm orb}$), which are expected to show a correlation according to Silk (1997). (e) $\tau_{\rm dep}$ versus $Q/\left(\Omega(1-0.7\beta)\right)$, which are expected to show a correlation according to Tan (2000). (f) $\tau_{\rm dep}$ versus A, which are expected to show a correlation according to Hunter et al. (1998). $\tau_{\rm dep}$ versus κ for the instability model (Meidt et al. 2018), while not shown here, was also tested; it produced a histogram largely identical to panel (a).

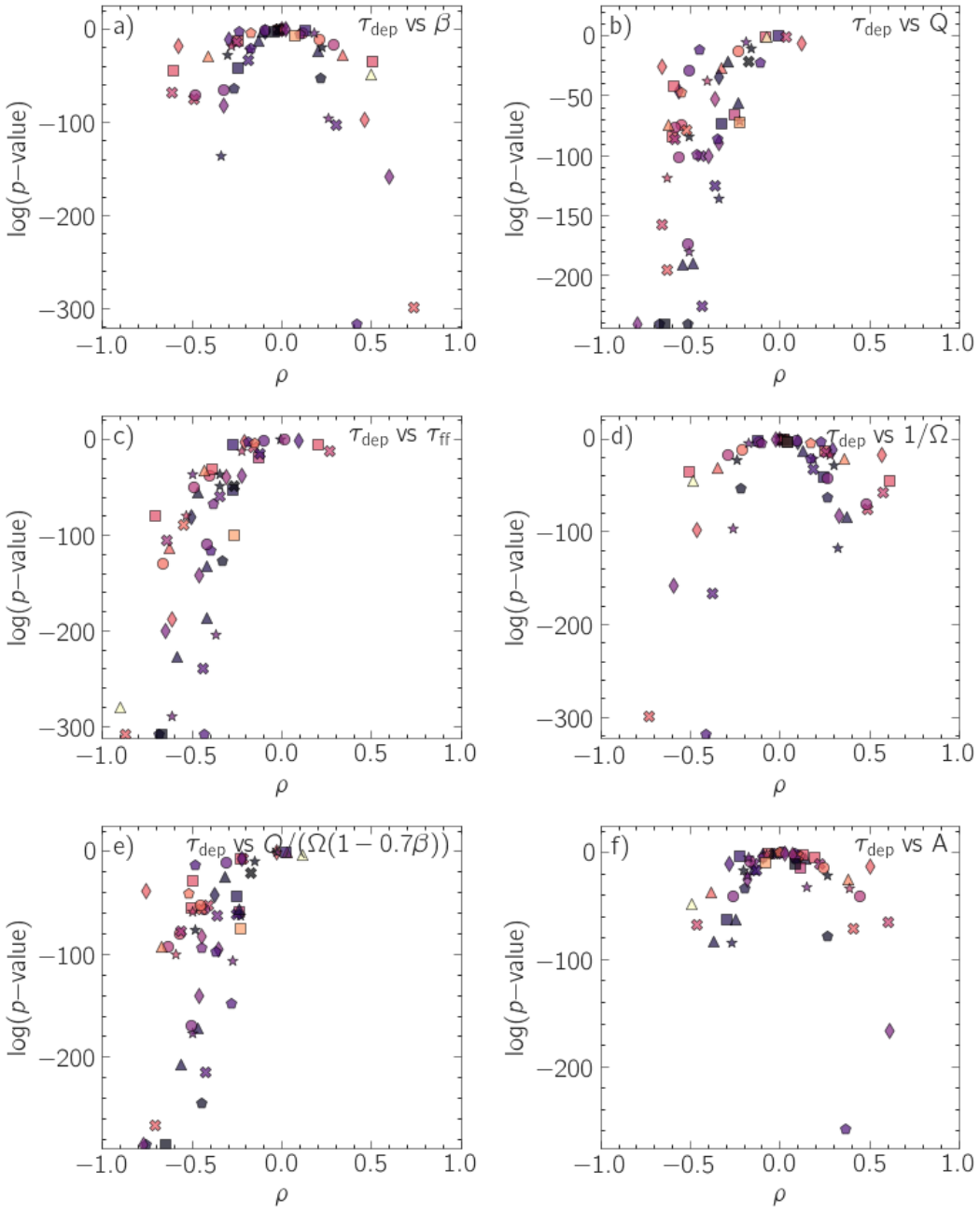

Figure 4.12: P-values for the Spearman rank coefficients for each galaxy across each sample, illustrating the significance of observed correlations for each tested model. P-values of exactly 0 are simply displayed at the bottom of each panel to indicate a logarithmic value approaching negative infinity. (a) $\tau_{\rm dep}$ versus β. (b) $\tau_{\rm dep}$ versus the Toomre Q. (c) $\tau_{\rm dep}$ versus $\tau_{\rm ff}$. (d) $\tau_{\rm dep}$ versus $1/\Omega$ (proportional to $\tau_{\rm orb}$). (e) $\tau_{\rm dep}$ versus $Q/\left(\Omega(1-0.7\beta)\right)$. (f) $\tau_{\rm dep}$ versus A. Note that $\tau_{\rm dep}$ versus κ for the instability model (Meidt et al. 2018), while not shown here, was also tested; its plot of p-values appeared incredibly similar to panel (a).

Section 1.4.2; however, we strongly caution that $\tau_{\rm dep} \propto \Sigma_{\rm mol}$ and $Q \propto \Sigma_{\rm mol}^{-1}$, meaning that this is likely a consequence of an intrinsic anticorrelation rather than a real result from the data.

Figure 4.6 shows the depletion time plotted against free-fall time as calculated with a constant scale height of ~ 100 pc (Section 1.4.3), where both quantities are again calculated using molecular surface densities rather than total gas densities. We note that the two quantities were expected to correlate linearly; however, we observe a strong anticorrelation instead.

Figure 4.7 shows the depletion time plotted against the orbital time to test the "orbital timescale" model (Section 1.4.4). A correlation was expected, but no clear correlation or anticorrelation is observed here.

Figure 4.8 shows the depletion time plotted against $Q/\left(\Omega(1-0.7\beta)\right)$, and an anticorrelation is observed, contrary to expectations (Section 1.4.5). However, as with the Toomre Q model, we caution that there is an intrinsic anticorrelation between $\tau_{\rm dep}$ and Q that appears to be dominating the relationship.

Figure 4.9 shows the depletion time plotted against κ (proportional to the approximate shear across cloud-sized regions; Section 1.4.6). The model predicts a positive correlation if this cloud-scale shear hinders cloud collapse. However, the trend between the two quantities appears to be largely nonexistent.

Figure 4.10 shows the depletion time plotted against the Oort A parameter, where a correlation is expected according to the shear-regulated model (Section 1.4.7). At first glance there appears to be an incredibly tenuous correlation when all of the data is compared at once; however, there appears to be little correlation on a galaxy-to-galaxy basis, to the point that we cannot reasonably conclude that a correlation exists.

The correlations among each of the galaxies for each theoretical model are summarized in Figure 4.11, which show histograms of the Spearman rank correlation coefficients in each of the samples ("all", "marginal", and "clean") for each of the models. The corresponding p-values of these correlation coefficients (that is, the probabilities that equally extreme or more-extreme results could be observed with a pair of completely uncorrelated quantities) are plotted in Figure 4.12, where val-

ues closer to 0 indicate high statistical significance. We note that nearly all of the p-values are incredibly close to 0.

Overall, we see little evidence that supports the idea that shear regulates star formation in the expected direction. We review the base results and ramifications in Section 5.

Chapter 5

Discussion

In this section, we discuss the results for the main analysis of $\tau_{\rm dep}$ versus β, along with possible reasons for the behaviours seen regarding the theoretical SFR model tests. As described in Section 2.3, the work presented here assumes an empirical model for the CO(2-1)-to-molecular conversion factor ($\alpha_{\rm CO}^{(2-1)}$) in which it varies based on the metallicity implied by the mass and radius of each galaxy. However, as also mentioned in Section 2.3, we had initially used a constant CO(2-1)-to-molecular conversion factor prior to adopting the more sophisticated (albeit experimental) method, adopting the Milky Way value of $6.2\frac{M_{\odot}/{\rm pc}^2}{\rm K\ km\ s^{-1}}$. The results for this comparatively simple method are presented and discussed in Appendix A.

5.1 Main Results & Models

A glance at Figure 4.1 does not reveal an immediate trend between $\tau_{\rm dep}$ and β. Individual galaxies tend to display somewhat of a correlation at higher shear, where β approaches 0 (on the outskirts of the galaxy where molecular depletion times decrease due to lower surface densities); however, other regions of the galaxies tend to not show an immediate trend. Figure 4.4a displays the distribution of Spearman rank correlation coefficients centered around 0 for this pair of quantities, indicating a lack of correlation; although we do note that the correlation coefficients tend to vary significantly from galaxy to galaxy. Overall, we cannot conclude that there is evidence for a correlation between $\tau_{\rm dep}$ and β.

Figure 4.2 shows a notably stronger correlation between $\tau_{\rm dep}/\tau_{\rm ff}$ and β, and not

just for the outskirts of the galaxies either. As seen in Equation 1.2, $\tau_{\rm ff} \propto \Sigma_{\rm mol}^{-0.5}$, and molecular densities tend to smoothly decrease with radius (Leroy et al., 2008), meaning that free-fall times tend to decrease as you get closer to the centers of galaxies. What this means is that $\tau_{\rm dep}/\tau_{\rm ff}$ will tend to increase with decreasing radius (that is, the depletion times become much longer compared to free-fall times towards the centers of galaxies by virtue of the free-fall times getting shorter), which overall coincides with β tending to increase with decreasing radius, albeit with significant galaxy-to-galaxy variation. Figure 4.4b highlights this trend handily, by showing a consistently positive Spearman rank correlation, with significant spread.

Figure 4.3 also displays a clear correlation between $\tau_{\rm dep}/\tau_{\rm orb}$ and β, which is supported by the consistently high Spearman rank correlation coefficients as seen in Figure 4.4c. However, as described in the previous section, $\tau_{\rm orb}$ has an intrinsic anticorrelation with β overall, which is what causes the two properties here to appear to correlate. There was not a significant trend between $\tau_{\rm dep}$ and β, and by throwing $\tau_{\rm orb}$ into the mix we are essentially comparing the rotation curve with itself, which does not provide us with any meaningful information.

We now move on to discussing the results for our star formation models.

For the "constant H_2 star formation efficiency" model (Section 1.4.1), Figure 4.1 does not show clear signs of a correlation between $\tau_{\rm dep}$ and β. This puts some points in favour of this simple conjecture that molecular depletion times do not vary with the galactic environment outside the molecular cloud; however, there is a lot of galaxy-to-galaxy variation in the depletion time values, which of course indicates that the actual molecular depletion times are hardly constant, either.

For the "Toomre Q" (Section 1.4.2), the moderate anticorrelation seen in Figure 4.5 does not match expectations. As described in Section 4.2, this is more likely due to an intrinsic anticorrelation between $\tau_{\rm dep}$ and Q than a real result from the data.

The "disk free fall time with fixed scale height" model (Section 1.4.3) predicts a linear trend between gas depletion time and gas free-fall time; however, Figure 4.6 shows a clear anticorrelation between the two, which is only further emphasized by Figure 4.11c. This hints at problems in our formulation when attempting to perform

this test. While our free-fall times were indeed calculated under the assumption of a constant scale height, we tested this particular law under the assumption that $\Sigma_{\rm gas} \approx \Sigma_{\rm mol}$ as described in Section 1.4. However, this is unlikely to be a good approximation in this case. With the molecular fraction tending to decrease with increasing radius (Leroy et al., 2008), this causes our estimated $\Sigma_{\rm gas}$ (and thus, gas depletion times) to appear artificially low with radius compared to reality, while free-fall times (proportional to $\Sigma_{\rm gas}^{-0.5}$) appeared artificially higher with radius. We can conclude from this that $\Sigma_{\rm mol}$ cannot reasonably act as a substitute for $\Sigma_{\rm gas}$ in regards to star formation laws where the latter is specified.

The "orbital timescale" model (Section 1.4.4) simply predicts a positive correlation between gas depletion time (estimated to be the molecular depletion time $\tau_{\rm dep}$) and $\tau_{\rm orb}$; however, a slight anticorrelation (with significant galaxy-to-galaxy variation as seen in Figure 4.11d, noting that $\tau_{\rm dep} \equiv 2\pi/\Omega$) is seen instead. As with the previously discussed models, this unexpected result is likely a consequence of our initial assumption that $\Sigma_{\rm gas} \approx \Sigma_{\rm mol}$ throughout; that is, our measurement of $\Sigma_{\rm mol}$ cannot be used as a substitute for total gas density $\Sigma_{\rm gas}$, especially at large radii where atomic gas begins to dominate.

The "GMC collision" model (Section 1.4.5), as described in Section 4.2, behaves contrary to its expectations of $\tau_{\rm dep}$ displaying a correlation with $Q/\left(\Omega(1-0.7\beta)\right)$. Again, as with the Toomre Q, this unexpected anticorrelation is due to the strong intrinsic anticorrelation between $\tau_{\rm dep}$ and Q.

The Meidt et al. (2018) model (Section 1.4.6) predicts that cloud-scale shear inhibits the collapse of gravitational instabilities, and thus predicts a positive trend between molecular $\tau_{\rm dep}$ and κ. Figure 4.9, however, does not appear to display any sort of correlation or anticorrelation between the two properties overall, very similarly to the comparison between $\tau_{\rm dep}$ and β. The Spearman rank correlation coefficient does not appear in Figure 4.11 for this model, as it would appear redundant compared to the $\tau_{\rm dep}$-vs-β histogram due to its striking similarity. We do note that this model considers $\Sigma_{\rm mol}$ rather than $\Sigma_{\rm gas}$, so the lack of correlation may be genuine here compared to some of the previously mentioned models.

Finally, the Hunter et al. (1998) model (Section 1.4.7) similarly predicts a trend

between τ_{dep} and A. These two models do not appear to be correlated, however, with the Spearman rank coefficients for each individual galaxy averaging to around 0 (Figure 4.11f).

As mentioned in Section 4, the p-values for the Spearman rank correlation coefficients for each of these comparisons are plotted in Figure 4.12, and consistently indicate an exceedingly low probability that similar results could be obtained under the null hypothesis, especially for correlation coefficients of approximately $|\rho| > 0.3$. That is, these results are consistently of high statistical significance wherever a correlation or anticorrelation is suggested; although we do note that data yielding correlation coefficients close to zero (that is, data that closely resemble the null hypothesis) tend to have higher p-values in the first place. We notice that the observed quantity comparisons that exhibit a strong correlation or anticorrelation overall tend to behave this way due to an intrinsic correlation or anticorrelation within the quantities themselves, and these results are thus discarded. More interestingly, however, are the quantity comparisons that do not exhibit a clear correlation or anticorrelation (such as τ_{dep} versus β). Their Spearman rank correlation coefficients tend to display strong galaxy-to-galaxy variation in this regard, in the sense that both correlations and anticorrelations of high statistical significance are still observed across the many individual galaxies. While the quantities themselves may not exhibit a clear trend, this behaviour provides evidence that some common underlying parameter(s) may be influencing the behaviour of both quantities.

Chapter 6

Summary & Conclusion

Recent evidence has suggested that star formation throughout galaxies is regulated by the local dynamical environment. We use recent CO(2-1) ALMA data and combined UV+IR star formation rate data from the z0MGS project to test these claims, primarily by comparing the molecular depletion times across the 74 primary PHANGS targets (with molecular surface densities and star formation rate surface densities convolved to a common physical scale of 750 pc, and calculated from integrated CO(2-1) intensities using an empirically-calibrated conversion factor) to their rotational shear (parameterized by the logarithmic derivative of the rotation curve β). In addition to this main analysis, we also used the in-hand data to test a number of proposed star formation models.

In order to generate the necessary smoothed analytic rotation curves for these goals, the DISKFIT software is used to optimize galaxy parameters such as kinematic position angle, inclination, and systemic velocity; producing noisy, empirical rotation curves for each galaxy as a byproduct. These optimized galactic parameters are then used to generate a smooth Universal Rotation Curve model (as defined in Persic et al., 1996) for each galaxy, which describes the overall circular motions of the gas based on the underlying mass distribution. Out of the initial PHANGS targets, 53 galaxies have all of the required data for the analysis.

Overall, when comparing quantities for both the main analysis and the tests for the star formation models using our very large homogeneous sample of molecular gas and star formation rate data, our analysis does not provide any substantial evidence for the influence of rotational shear on star formation rate, nor does it ex-

hibit clear support for any of the models. However, when comparing key quantities with no overall correlation such as depletion time and the β parameter, both correlations and anticorrelations with strong statistical significance are observed across the many individual galaxies. This strong but contradictory evidence of correlation suggests that, despite an overall trend not being apparent, the quantities are both influenced by some underlying parameter(s) that have yet to be fully considered.

6.1 Future Work

This analysis overall was performed on kpc scales due to the limited (~ 7.5") resolution of the WISE+GALEX star formation rate maps from the z0MGS project. However, PHANGS already has ~ 1" resolution CO(2-1) ALMA data available, and an upcoming Hα survey will obtain star formation rate maps on 1" scales as well. These new high-resolution data will be used to study the effect of shear on star formation rates at scales comparable to the galaxy disk scale heights (100 pc) as opposed to the present work, which is more comparable to the disk scale lengths (1 kpc).

References

Bolatto A. D., Wolfire M., Leroy A. K., 2013, ARA&A, 51, 207

Brandt J. C., 1960, ApJ, 131, 293

Carroll B. W., Ostlie D. A., 2006, An introduction to modern astrophysics and cosmology

Elmegreen B. G., 1989, ApJ, 338, 178

Hunter D. A., Elmegreen B. G., Baker A. L., 1998, ApJ, 493, 595

Kennicutt Robert C. J., 1998, ApJ, 498, 541

Kennicutt R. C., Evans N. J., 2012, ARA&A, 50, 531

Krumholz M. R., 2015, arXiv e-prints, p. arXiv:1511.03457

Krumholz M. R., Tan J. C., 2007, ApJ, 654, 304

Leroy A. K., Walter F., Brinks E., Bigiel F., de Blok W. J. G., Madore B., Thornley M. D., 2008, AJ, 136, 2782

Leroy A. K., et al., 2013, AJ, 146, 19

Leroy A. K., et al., accepted

Meidt S. E., et al., 2018, ApJ, 854, 100

Paturel G., Fouque P., Bottinelli L., Gouguenheim L., 1989, A&AS, 80, 299

Persic M., Salucci P., Stel F., 1996, MNRAS, 281, 27

Salo H., et al., 2015, ApJS, 219, 4

Sánchez S. F., et al., 2014, A&A, 563, A49

Sánchez S. F., et al., 2019, MNRAS, 484, 3042

Schiminovich D., et al., 2007, ApJS, 173, 315

Sellwood J. A., Sánchez R. Z., 2010, MNRAS, 404, 1733

Silk J., 1997, ApJ, 481, 703

Spekkens K., Sellwood J. A., 2007, ApJ, 664, 204

Suwannajak C., Tan J. C., Leroy A. K., 2014, ApJ, 787, 68

Tan J. C., 2000, ApJ, 536, 173

Utomo D., et al., 2018, ApJ, 861, L18

Appendix A

Alternate Method: Constant $\alpha_{\rm CO}^{(2-1)}$

Recent observations suggest that the CO(2-1)-to-molecular conversion factor tends to increase with radius (Bolatto et al., 2013), so all of our main results and all of our theoretical model tests, as presented in Sections 4 and 5, were calculated using this empirically-calibrated radially-scaling conversion factor. However, prior to obtaining the conversion factor this way, a heavily-simplified method was used instead, where the CO(2-1)-to-molecular conversion factor was assumed to have a constant value of $\alpha_{\rm CO}^{(2-1)} = 6.2 \frac{M_\odot/{\rm pc}^2}{\rm K\ km\ s^{-1}}$ (from the value observed in the Milky Way as described in Section 2.3; Utomo et al., 2018).

Here, we present all of the calculations presented in the aforementioned sections using this simplified method. Figures 4.1 through 4.12 are essentially "repeated" with the constant $\alpha_{\rm CO}^{(2-1)}$ in Figures A.1 through A.12. Note that the constant conversion factor creates the effect of $\Sigma_{\rm mol}$ decreasing with radius more harshly than it did with the more sophisticated (albeit experimental) method, which in turn causes $\tau_{\rm dep}$ to behave similarly. When comparing this new set of images with their more-sophisticated counterparts in Section 4, we notice overall that this simplified method introduces a stronger trend of depletion times being longer at lower radii than at higher radii. This radial trend for depletion time "shifts" many of the correlations (or lacks thereof) that were observed with the radially-scaling conversion factor, and often introduces weak correlations where there were none previously.

We stress that this method may be a gross oversimplification of the conversion factor, and may cause the molecular surface densities $\Sigma_{\rm mol}$ to appear artificially low with increasing radius compared to reality, which in turn causes all of the $\tau_{\rm dep}$

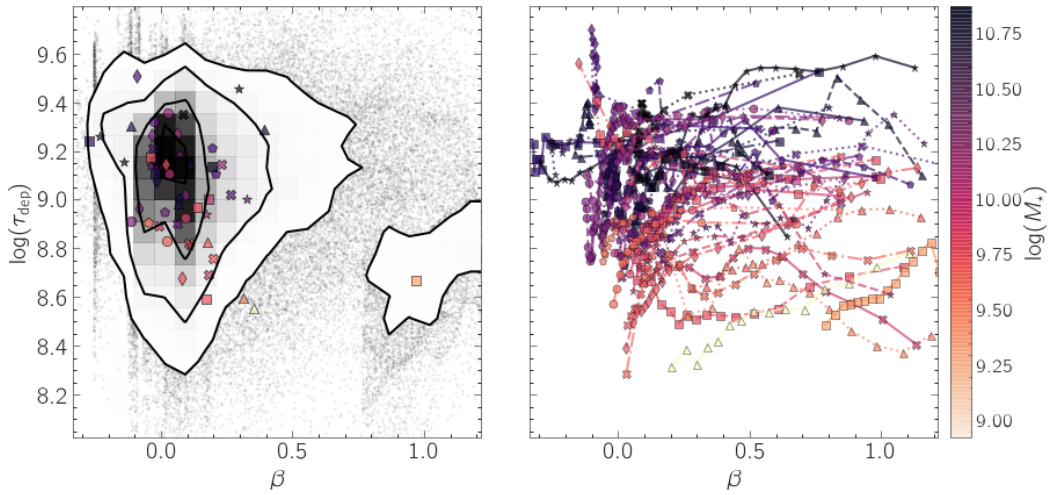

Figure A.1: τ_{dep} versus β for the "marginal" galaxies in the dataset, with constant $\alpha_{\rm CO}^{(2-1)}$. *Left:* 2D histogram of the combined $\tau_{\rm dep}$ and projected β maps over this sample, with the markers indicating the median values of each galaxy, and the colours of these markers indicating the stellar masses of the galaxy. *Right:* Overall trend of $\tau_{\rm dep}$ versus β for each galaxy, in radial bins with equal numbers of data. A slight positive correlation appears to have been introduced with this constant $\alpha_{\rm CO}^{(2-1)}$ method.

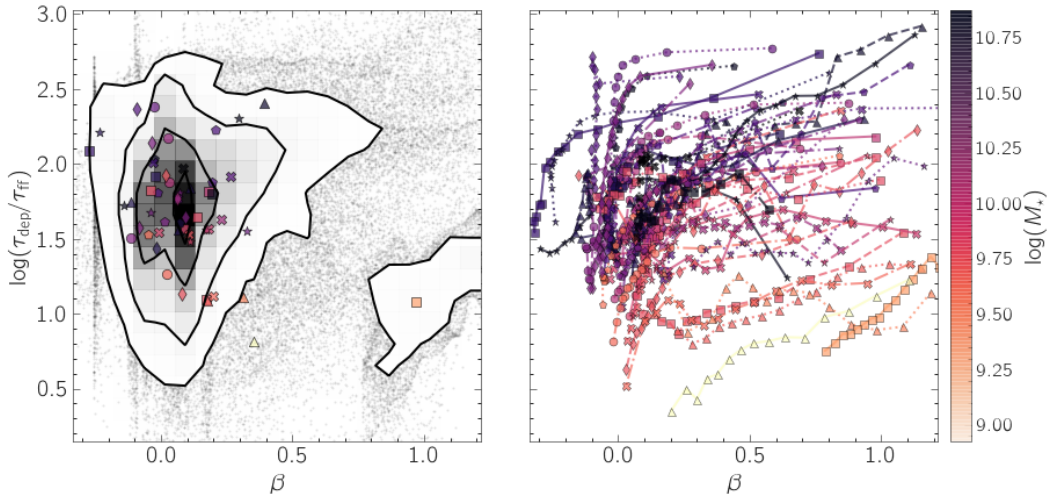

Figure A.2: $\tau_{\rm dep}/\tau_{\rm ff}$ versus β for the "marginal" galaxies in the dataset, with constant $\alpha_{\rm CO}^{(2-1)}$. *Left:* 2D histogram of the combined $\tau_{\rm dep}/\tau_{\rm ff}$ and projected β maps over this sample, with the markers indicating the median values of each galaxy, and the colours of these markers indicating the stellar masses of the galaxy. *Right:* Overall trend of $\tau_{\rm dep}/\tau_{\rm ff}$ versus β for each galaxy, in radial bins with equal numbers of data. There appears to be a weak correlation between the two properties.

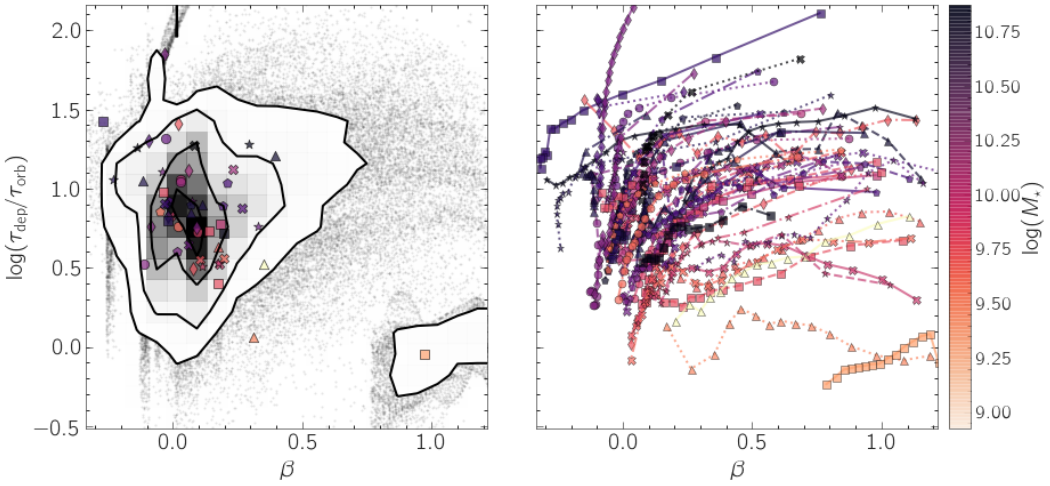

Figure A.3: $\tau_{\rm dep}/\tau_{\rm orb}$ versus β for the "marginal" galaxies in the dataset, with constant $\alpha_{\rm CO}^{(2-1)}$. *Left:* 2D histogram of the combined $\tau_{\rm dep}/\tau_{\rm orb}$ and projected β maps over this sample, with the markers indicating the median values of each galaxy, and the colours of these markers indicating the stellar masses of the galaxy. *Right:* Overall trend of $\tau_{\rm dep}/\tau_{\rm orb}$ versus β for each galaxy, in radial bins with equal numbers of data. The two properties appear to be correlated, although this is likely due to an intrinsic anticorrelation between $\tau_{\rm orb}$ and β. The trend appears to be enhanced somewhat compared to the radially-varying $\alpha_{\rm CO}^{(2-1)}$ method.

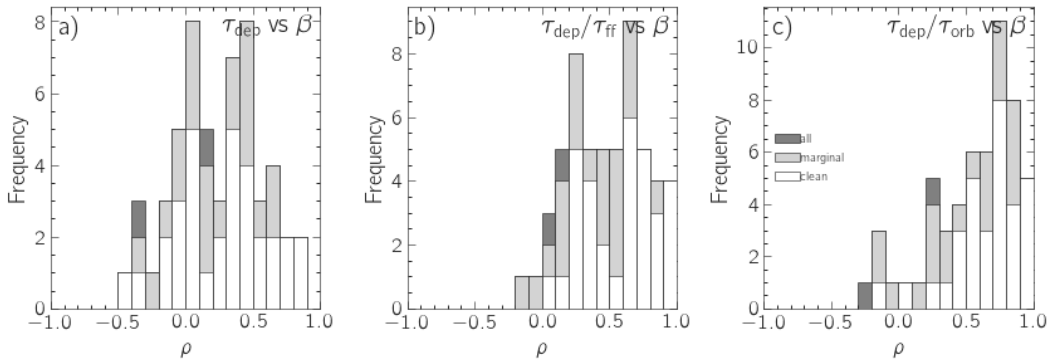

Figure A.4: Histograms showing the Spearman rank coefficients for each galaxy across our main sample, with constant $\alpha_{\rm CO}^{(2-1)}$, illustrating observed correlations for: (a) $\tau_{\rm dep}$ versus β, (b) $\tau_{\rm dep}/\tau_{\rm ff}$ versus β, (c) $\tau_{\rm dep}/\tau_{\rm orb}$ versus β.

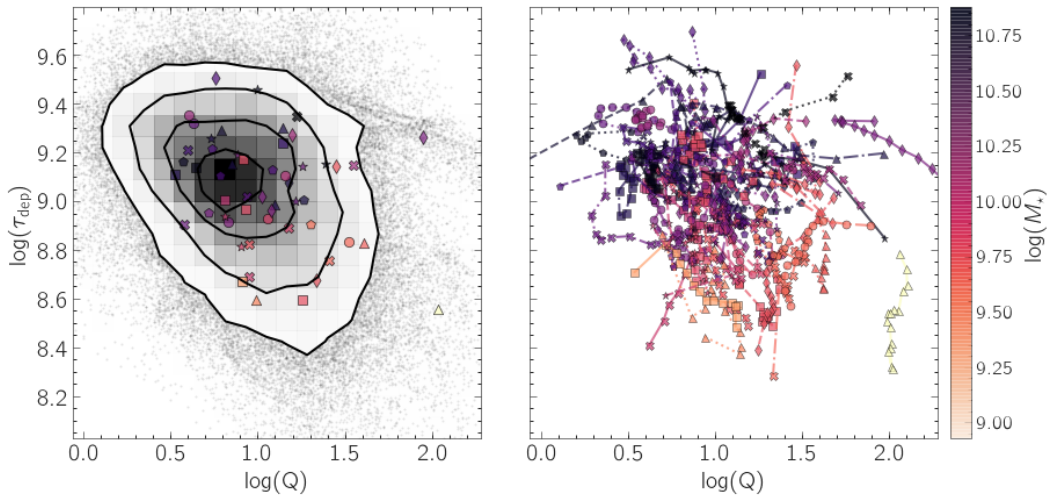

Figure A.5: $\tau_{\rm dep}$ versus Q for the "marginal" galaxies in the dataset, with constant $\alpha_{\rm CO}^{(2-1)}$. *Left:* 2D histogram of the combined $\tau_{\rm dep}$ and projected Q maps over this sample, with the markers indicating the median values of each galaxy, and the colours of these markers indicating the stellar masses of the galaxy. *Right:* Overall trend of $\tau_{\rm dep}$ versus Q for each galaxy, in radial bins with equal numbers of data. The quantities appear to be anticorrelated, closely resembling the radially-scaling $\alpha_{\rm CO}^{(2-1)}$ method.

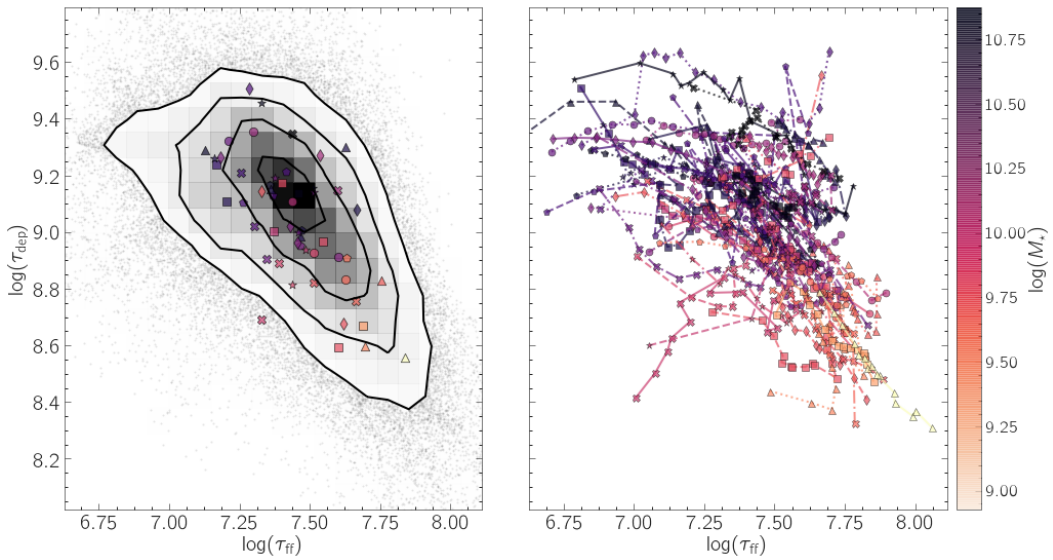

Figure A.6: $\tau_{\rm dep}$ versus $\tau_{\rm ff}$ for the "marginal" galaxies in the dataset, with constant $\alpha_{\rm CO}^{(2-1)}$. *Left:* 2D histogram of the combined $\tau_{\rm dep}$ and $\tau_{\rm ff}$ maps over this sample, with the markers indicating the median values of each galaxy, and the colours of these markers indicating the stellar masses of the galaxy. *Right:* Overall trend of $\tau_{\rm dep}$ versus $\tau_{\rm ff}$ for each galaxy, in radial bins with equal numbers of data. The anticorrelation between the properties is stronger here than with the radially-varying $\alpha_{\rm CO}^{(2-1)}$ method.

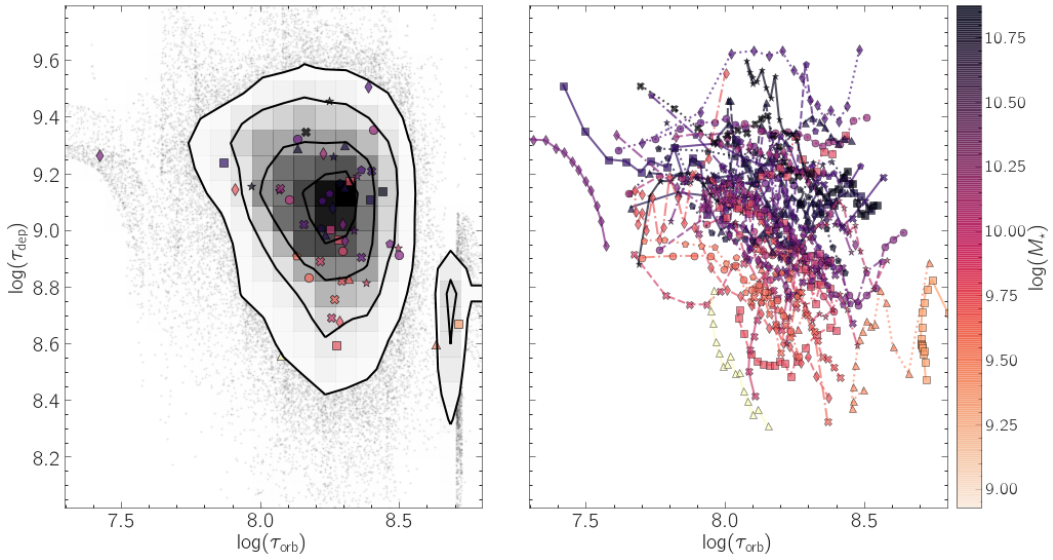

Figure A.7: $\tau_{\rm dep}$ versus $\tau_{\rm orb}$ for the "marginal" galaxies in the dataset, with constant $\alpha_{\rm CO}^{(2-1)}$. *Left:* 2D histogram of the combined $\tau_{\rm dep}$ and $\tau_{\rm orb}$ maps over this sample, with the markers indicating the median values of each galaxy, and the colours of these markers indicating the stellar masses of the galaxy. *Right:* Overall trend of $\tau_{\rm dep}$ versus $\tau_{\rm orb}$ for each galaxy, in radial bins with equal numbers of data. A slight anticorrelation between the two properties appears to have been introduced with this method.

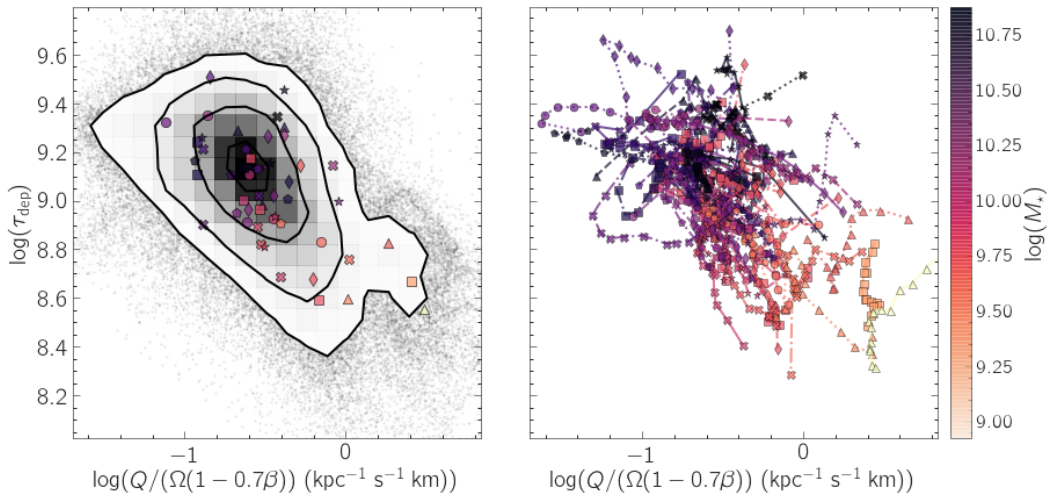

Figure A.8: $\tau_{\rm dep}$ versus $Q/\left(\Omega(1-0.7\beta)\right)$ for the "marginal" galaxies in the dataset, with constant $\alpha_{\rm CO}^{(2-1)}$. *Left:* 2D histogram of the combined $\tau_{\rm dep}$ and $Q/\left(\Omega(1-0.7\beta)\right)$ maps over this sample, with the markers indicating the median values of each galaxy, and the colours of these markers indicating the stellar masses of the galaxy. *Right:* Overall trend of $\tau_{\rm dep}$ versus $Q/\left(\Omega(1-0.7\beta)\right)$ for each galaxy, in radial bins with equal numbers of data. There is a clear anticorrelation between the two quantities, closely resembling the radially-scaling $\alpha_{\rm CO}^{(2-1)}$ method.

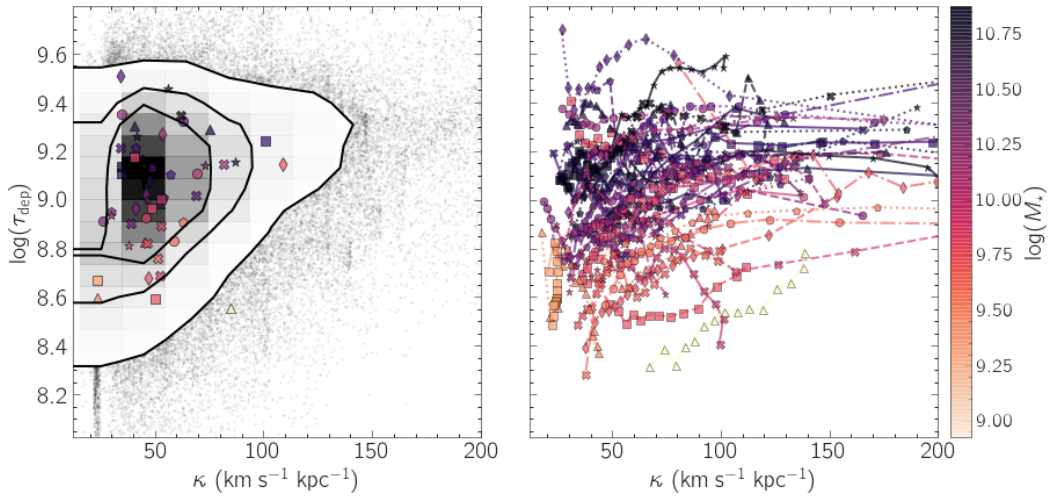

Figure A.9: $\tau_{\rm dep}$ versus κ for the "marginal" galaxies in the dataset, with constant $\alpha_{\rm CO}^{(2-1)}$. *Left:* 2D histogram of the combined $\tau_{\rm dep}$ and κ maps over this sample, with the markers indicating the median values of each galaxy, and the colours of these markers indicating the stellar masses of the galaxy. *Right:* Overall trend of $\tau_{\rm dep}$ versus κ for each galaxy, in radial bins with equal numbers of data. A slight positive correlation appears to have been introduced with this constant $\alpha_{\rm CO}^{(2-1)}$ method.

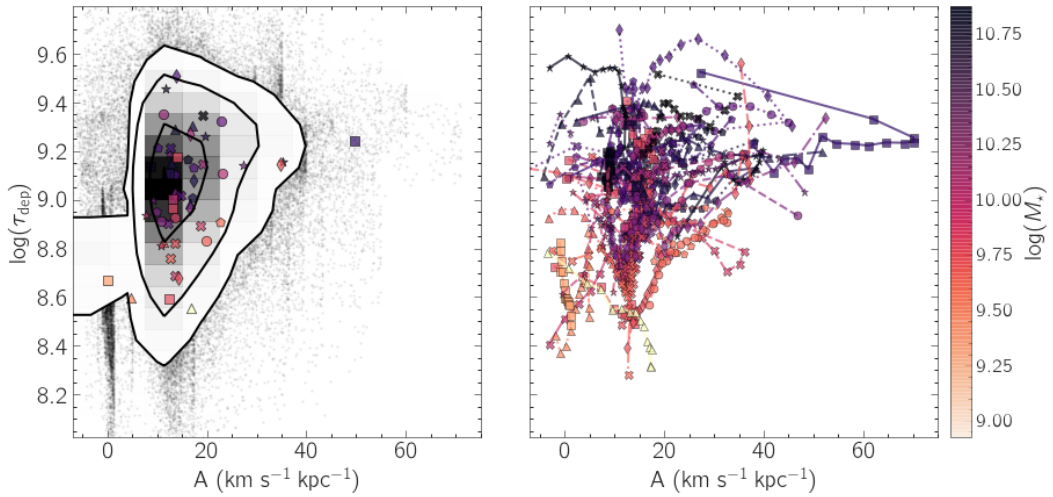

Figure A.10: $\tau_{\rm dep}$ versus A for the "marginal" galaxies in the dataset, with constant $\alpha_{\rm CO}^{(2-1)}$. *Left:* 2D histogram of the combined $\tau_{\rm dep}$ and A maps over this sample, with the markers indicating the median values of each galaxy, and the colours of these markers indicating the stellar masses of the galaxy. *Right:* Overall trend of $\tau_{\rm dep}$ versus A for each galaxy, in radial bins with equal numbers of data. Compared to the radially-varying $\alpha_{\rm CO}^{(2-1)}$ method, there appears to be a very slight correlation when all of the data is considered at once, although the correlation is tenuous at best on a galaxy-to-galaxy basis.

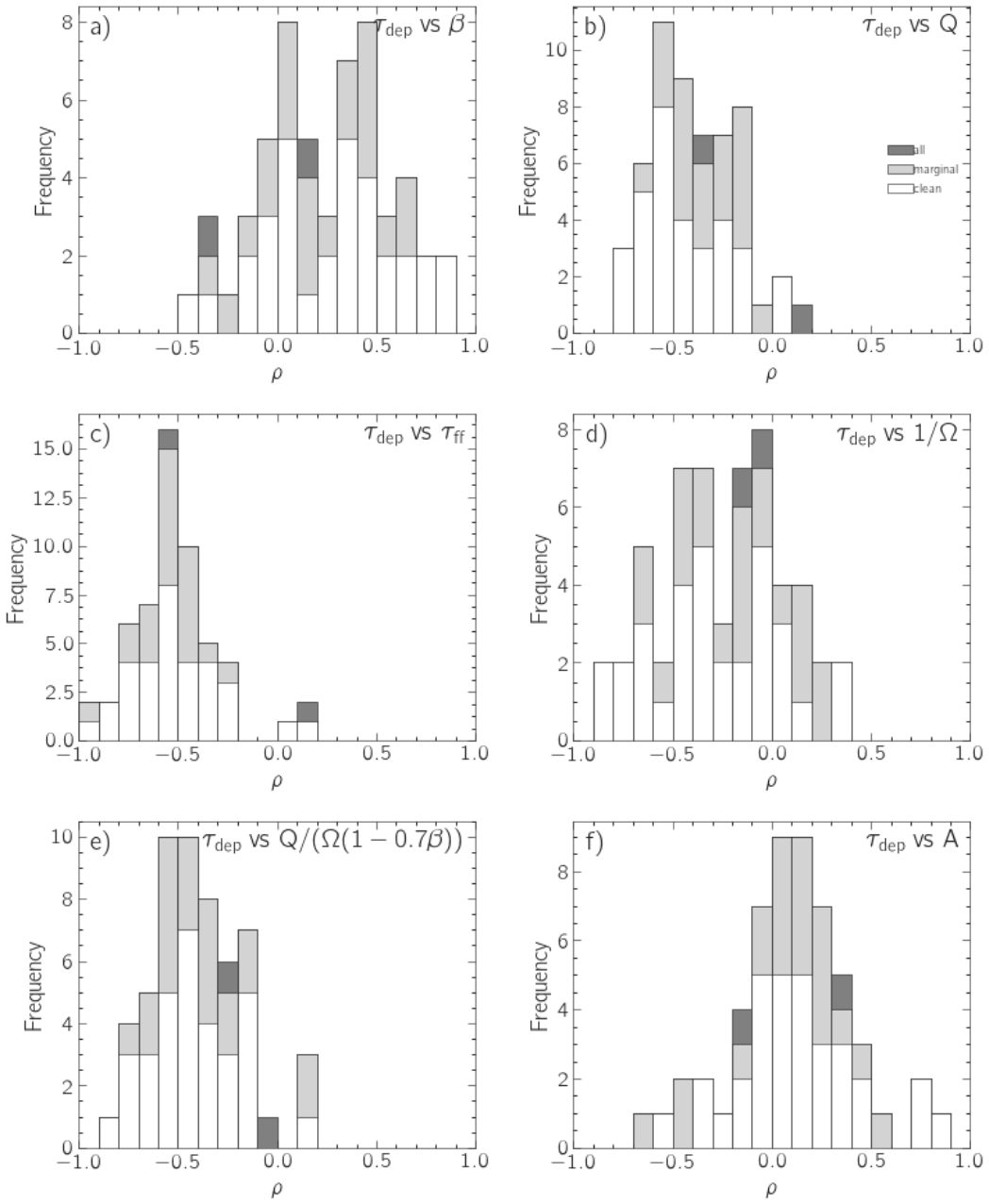

Figure A.11: Histograms showing the Spearman rank coefficients for each galaxy across each sample, with constant $\alpha_{\rm CO}^{(2-1)}$, illustrating observed correlations for each tested model: (a) $\tau_{\rm dep}$ versus β. (b) $\tau_{\rm dep}$ versus the Toomre Q, which are expected to show a correlation according to Section 1.4.2. (c) $\tau_{\rm dep}$ versus $\tau_{\rm ff}$, which are expected to display a correlation according to Kennicutt (1998) assuming constant scale height. (d) $\tau_{\rm dep}$ versus $1/\Omega$ (proportional to $\tau_{\rm orb}$), which are expected to show a correlation according to Silk (1997). (e) $\tau_{\rm dep}$ versus $Q/\left(\Omega(1-0.7\beta)\right)$, which are expected to show a correlation according to Tan (2000). (f) $\tau_{\rm dep}$ versus A, which are expected to show a correlation according to Hunter et al. (1998). Note that $\tau_{\rm dep}$ versus κ for the instability model (Meidt et al. 2018), while not shown here, was also tested; it produced a histogram largely identical to panel (a) of this figure even with the constant $\alpha_{\rm CO}^{(2-1)}$ method.

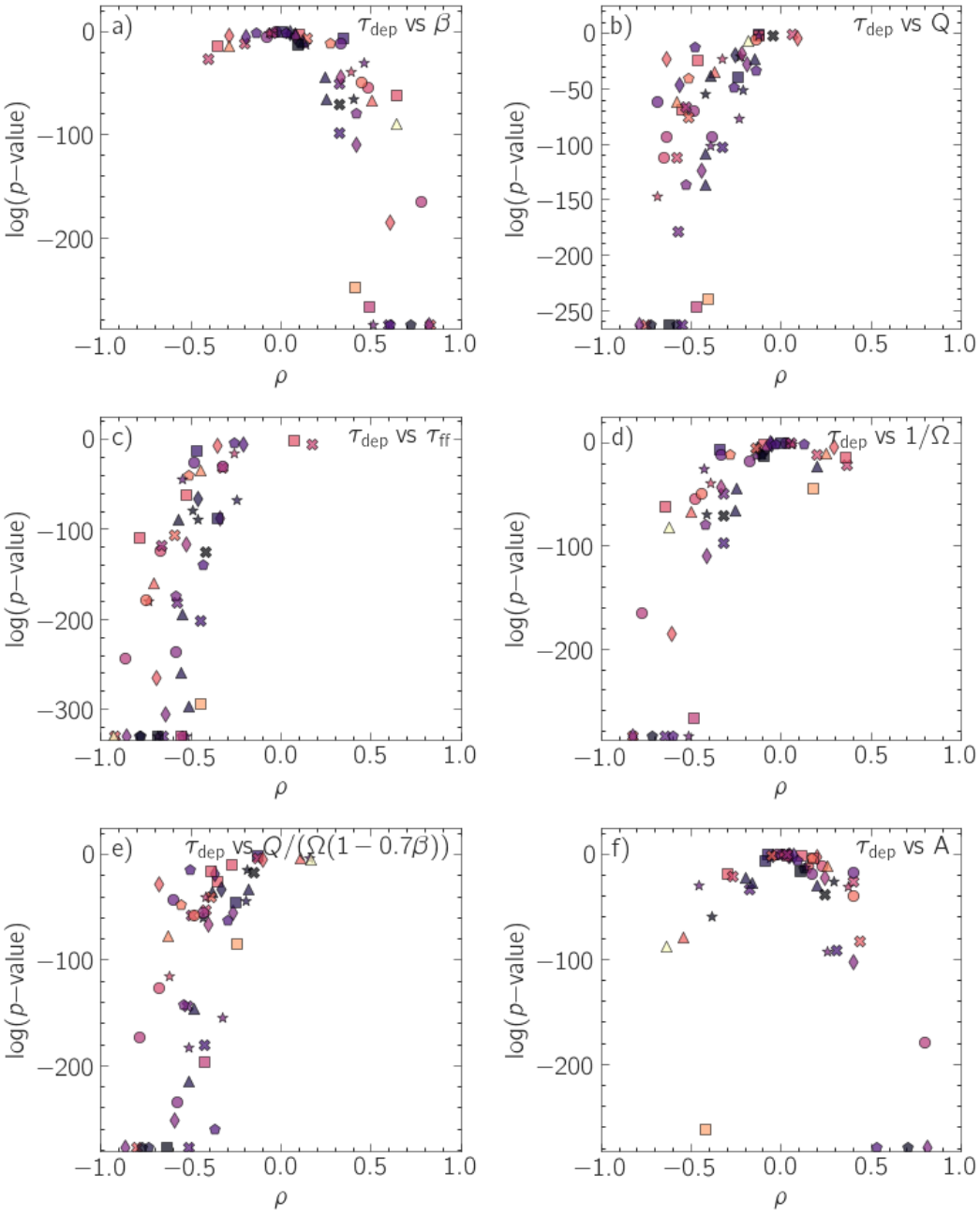

Figure A.12: P-values for the Spearman rank coefficients for each galaxy across each sample, with constant $\alpha_{CO}^{(2-1)}$, illustrating the significance of observed correlations for each tested model. P-values of exactly 0 are simply displayed at the bottom of each panel to indicate a logarithmic value approaching negative infinity. (a) τ_{dep} versus β. (b) τ_{dep} versus the Toomre Q. (c) τ_{dep} versus τ_{ff}. (d) τ_{dep} versus $1/\Omega$ (proportional to τ_{orb}). (e) τ_{dep} versus $Q/\left(\Omega(1-0.7\beta)\right)$. (f) τ_{dep} versus A. Note that τ_{dep} versus κ for the instability model (Meidt et al. 2018), while not shown here, was also tested; its plot of p-values appeared incredibly similar to panel (a) of this figure even with the constant $\alpha_{CO}^{(2-1)}$ method.

calculations to show more change with radius than what is actually occurring.

Figures A.1 and A.4a show the trend between $\tau_{\rm dep}$ and β under this simplified method. While these quantities did not exhibit a correlation with the radially-scaling method, a very faint correlation does seem to appear here, as depletion time decreases with radius more strongly than it did previously. Similarly, where a trend was observed between $\tau_{\rm dep}/\tau_{\rm ff}$ and β (Figures A.2, A.4b), this relation appears to be significantly stronger now that molecular density decreases with radius more harshly. The same can be said for $\tau_{\rm dep}/\tau_{\rm orb}$ versus β, which exhibited a strong correlation previously; the strength of this correlation has increased somewhat with this simplified method (Figures A.3, A.4c).

Similar changes can be observed in the theoretical model tests. The most stark difference from the results in Section 4 is that the unexpected anticorrelation between $\tau_{\rm dep}$ versus $\tau_{\rm ff}$ has become significantly stronger than it was with the radially-scaling conversion factor (Figures A.6, A.11c) due to the molecular gas density (our estimate for the total gas density that this model considers) decreasing more strongly with radius.

As another consequence of this effect, the constant conversion factor causes slight correlations or anticorrelations to manifest in the "orbital timescale" (Figures A.7, A.11d), "Meidt et al. (2018)" (Figure A.9, with histogram nearly identical to Figure A.11a), and "Hunter et al. (1998)" (albeit very weakly; Figures A.10, A.11f) models, in the sense that all of these tests' Spearman rank correlation coefficients no longer appear to average at nearly 0. Specifically: the "orbital timescale" model changes from exhibiting no correlation to having an unexpected anticorrelation due to the estimated gas density decreasing with radius more harshly, which suggests that the results from Section 4 would have been more in line with expectations (i.e. a positive correlation, instead of a lack of correlation) had we been able to properly use $\Sigma_{\rm gas}$ instead of incorrectly estimating it to be $\Sigma_{\rm mol}$. The Meidt et al. (2018) model also sees a correlation introduced here, although we note that its lack of correlation in Section 4 may be genuine, since that model relies on $\Sigma_{\rm mol}$ and the experimental radially-varying conversion factor is arguably more accurate than this simplified method. The Hunter et al. (1998) model also appears to have a

correlation introduced with this simplified method compared to the radially-varying $\alpha_{\rm CO}^{(2-1)}$ (albeit an incredibly weak one), owing to the overall increase in the radial dependence of $\tau_{\rm dep}$.

Finally, the Toomre Q and GMC collision models did not appear to be significantly affected by this change.

Figure A.12 shows plots of Spearman rank correlation coefficients compared to their p-values, with each panel presenting the same model as in Figure A.11. As with Figure 4.12, the correlations exhibit strong statistical significance for this (vastly oversimplified) constant-$\alpha_{\rm CO}^{(2-1)}$ model.

Appendix B

$\tau_{\rm dep}$ versus β: Alternate display methods

The main test of $\tau_{\rm dep}$ versus β in Section 4.1 (Figure 4.1) proved to not show a substantial correlation. However, a handful of display tricks were considered to see if a visible trend might emerge if the data were perhaps presented in a slightly different way.

B.1 Normalization of β-Axis and $\tau_{\rm dep}$-Axis by Medians

Figures B.1 and B.2 display $\tau_{\rm dep}$ versus β, with each galaxy's contribution to the $\tau_{\rm dep}$-axis or both axes (respectively) normalized with respect to its own median. This brings each galaxy's trends closer to the center of each panel, with the hope that if a common functional relationship between the two quantities existed, it would manifest more clearly when normalized this way.

It didn't.

B.2 Normalization of $\tau_{\rm dep}$-Axis by Characteristic Depletion Timescale

Another method at normalizing the y-axis involved dividing each galaxy's depletion time by its own "characteristic" depletion time, defined as the mean of depletion time values from all lines of sight within 0.5 kpc of the characteristic radius, $R_{\rm e}$

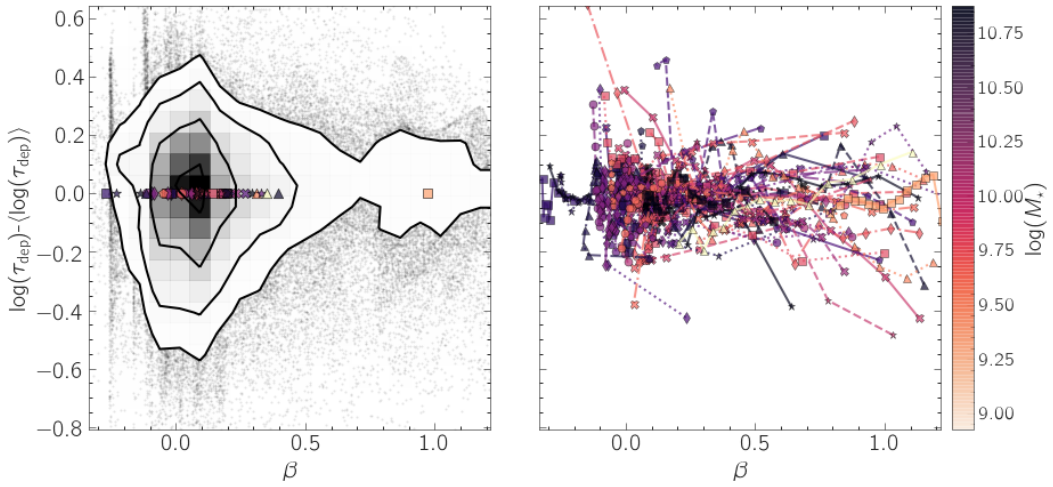

Figure B.1: $\log(\tau_{\rm dep}) - \langle\log(\tau_{\rm dep})\rangle$ versus β for the "marginal" galaxies in the dataset. *Left:* 2D histogram of the combined $\tau_{\rm dep}$ (with each galaxy's contribution normalized with respect to its own median) and projected β maps over this sample, with the markers indicating the median values of each galaxy, and the colours of these markers indicating the stellar masses of the galaxy. *Right:* Overall trends for each galaxy, in bins of equal number.
Even with the depletion axis normalized, there does not appear to be a strong correlation between the two properties.

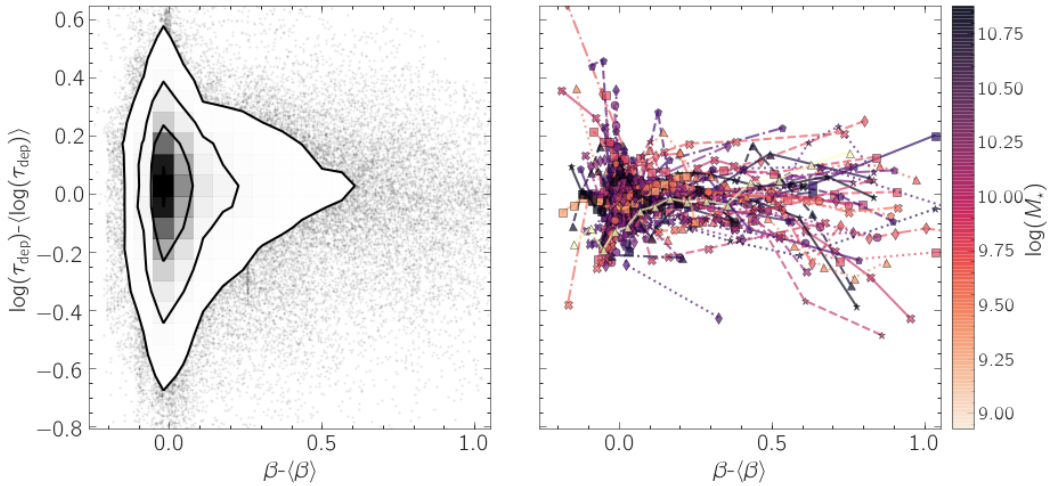

Figure B.2: $\log(\tau_{\rm dep}) - \langle\log(\tau_{\rm dep})\rangle$ versus $\beta - \langle\beta\rangle$ for the "marginal" galaxies in the dataset. *Left:* 2D histogram of the combined $\tau_{\rm dep}$ and projected β maps over this sample (with each galaxy's contributions normalized with respect to their own medians on both axes). *Right:* Overall trends for each galaxy, in bins of equal number.
Even with both axes normalized, there does not appear to be a strong correlation between the two properties.

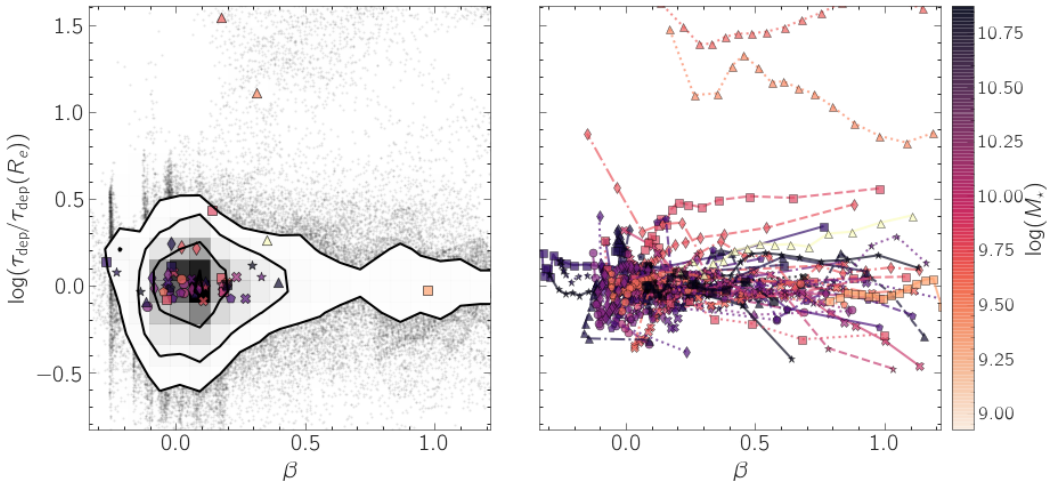

Figure B.3: $\tau_{\rm dep}/\tau_{\rm dep}(R_{\rm e})$ versus β for the "marginal" galaxies in the dataset. *Left:* 2D histogram of the combined $\tau_{\rm dep}/\tau_{\rm dep}(R_{\rm e})$ and projected β maps over this sample, with the markers indicating the median values of each galaxy, and the colours of these markers indicating the stellar masses of the galaxy. *Right:* Overall trends for each galaxy, in bins of equal number.
Even with the depletion axis normalized by a value intrinsic to each individual galaxy, there does not appear to be a strong correlation between the two properties.

(Figure B.3). Shifting each galaxy's trend up or down by a value intrinsic to that galaxy was thought to possibly have highlighted a trend that was not seen previously but this did not reveal anything more clearly.

B.3 Separation by Mass

As seen in most of the figures in this work, each individual galaxy is assigned a colour based on its stellar mass, in order to potentially highlight a pattern when quantities such as $\tau_{\rm dep}$ and β are compared. As an example of this, Figure 2.2 displays a linear trend between star formation rate and molecular surface densities, with less-massive galaxies tending to have lower gas densities, and therefore shorter depletion times.

This same pattern of lower-mass galaxies having shorter molecular depletion times can be seen in Figures 4.1 through 4.10, and in Figures A.1 through A.10. This did not lead to any insight on the correlations themselves, however.

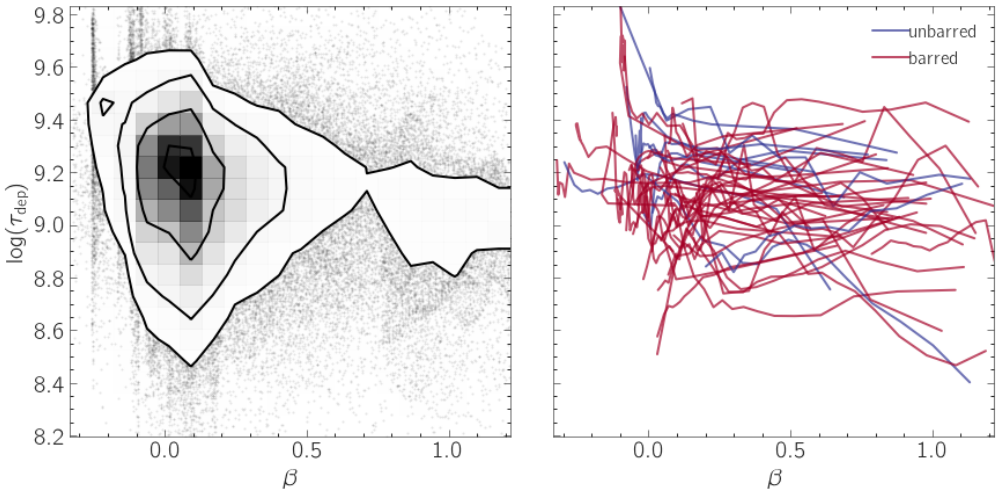

Figure B.4: $\tau_{\rm dep}$ versus β for the "marginal" galaxies in the dataset, coloured by whether the galaxy is barred. *Left:* 2D histogram of the combined $\tau_{\rm dep}$ and projected β maps over this sample. *Right:* Overall trends for each galaxy, in bins of equal number, coloured based on whether each galaxy is barred or not.
Even with the barred/unbarred galaxies separated in this way, no additional pattern became apparent.

B.4 Separation by Presence of a Bar

Figure B.4 is essentially the same as Figure 4.1, except galaxies are coloured by whether they are barred rather than by mass. No correlation between the presence of a bar and either $\tau_{\rm dep}$ or β is apparent.

It is worth noting that, as mentioned in Section 3.1, DISKFIT was performed using an unbarred model. This means that strongly-barred galaxies may not have the best possible rotation curves in the first place, and that behaviours may be slightly different if a bar fit were to be run successfully. However, a substantial improvement in the context of this work seems unlikely; the rotation curves are still smoothed using a simple 3-parameter fit to the URC model, causing any improvements at lower radii from a successful bar fit to be largely "smoothed out" anyways.

B.5 Separation by Hubble Type

Similarly to the above, Figure B.5 is the same as Figure 4.1 except coloured based on each galaxy's Hubble morphology T rather than stellar mass, with later-type

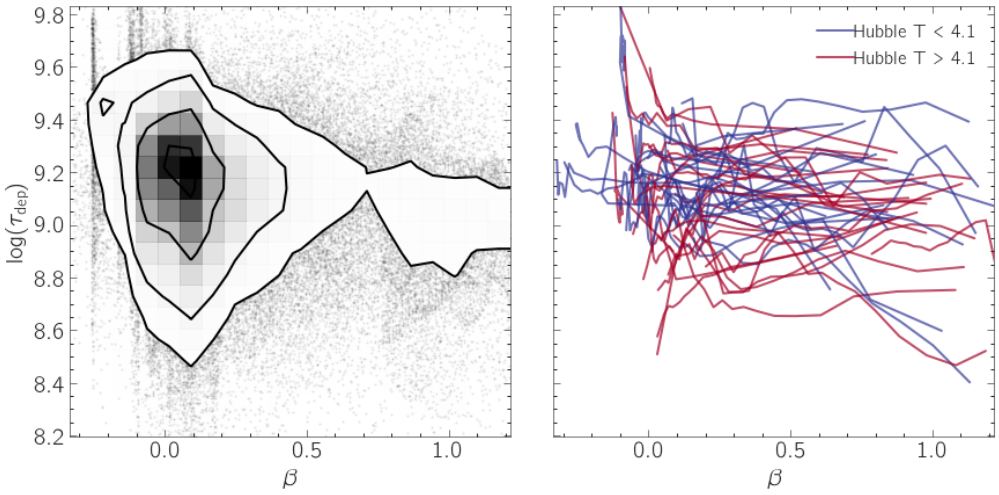

Figure B.5: $\tau_{\rm dep}$ versus β for the "marginal" galaxies in the dataset, coloured by Hubble type T. *Left:* 2D histogram of the combined $\tau_{\rm dep}$ and projected β maps over this sample. *Right:* Overall trends for each galaxy, in bins of equal number, coloured based on each galaxy's Hubble type.
Even when sorted by morphology in this way, no additional pattern became apparent.

galaxies receiving a redder colouration than earlier-types. While this does not shed any light on the trend (or lack thereof) between $\tau_{\rm dep}$ and β, we do note that later-type galaxies do seem to have lower depletion times overall.

Appendix C

Alternatives to the Universal Rotation Curve

C.1 Alternative Rotation Curve Smoothing Models

As mentioned in Section 3.2, there were several methods for smoothing the DISK-FIT rotation curves that were tested. While the URC model was selected in the end, another theoretical rotation curve model considered was Brandt's parameterization of a galactic rotation curve (Brandt 1960), which we will refer to as the Brandt model:

$$V(R) = V_{\max} \frac{R/R_{\max}}{\left(\frac{1}{3} + \frac{2}{3}\left(\frac{R}{R_{\max}}\right)^n\right)^{\frac{3}{2n}}} \tag{C.1}$$

for some positive $V_{\max}$, $R_{\max}$, and n.

Another was an incredibly simple exponential fit (Leroy et al. 2013), used mainly for illustrative comparisons when considering the Brandt and URC models:

$$V(R) = v_{\text{flat}}\left(1 - \exp\left(\frac{R}{R_{\text{flat}}}\right)\right) \tag{C.2}$$

for some v_{flat} and R_{flat}. We will simply refer to this as the simple model.

Overall, the Brandt and URC models behave quite similarly and both create very plausible smoothed rotation curves. However, the Universal model is better at capturing certain rising/falling features from the fitted rotation curves, so between the two, the URC model was applied to our rotation curves for our main analysis.

C.1.1 Spline Fitting

In addition to attempting fits to theoretical rotation curve models, we also attempted to smooth the curves with a spline fit. The intended purpose for this was to avoid "over-smoothing" the DISKFIT rotation curves to the point that the individual rising/falling shapes are lost (as is the case with the aforementioned theoretical models), but instead create a less-jittery version of the DISKFIT rotation curve that retained these distinct, small-scale patterns. While these rotation curves would essentially be smoothed versions of the observed deprojected *mom1* data (instead of making any attempt to capture the underlying circular motions of the orbiting gas), the objective here was to simply test whether the smaller-scale rises and falls of a rotation curve projected to a 2D velocity map would correlate in some way with the depletion time, in a way that the smoother theoretical models could not capture.

Figure C.1c shows an example of both the URC fit and a spline fit for NGC1566's rotation curve; and Figure C.1d displays how the β parameter varies with radius for both of these smoothing methods, with the depletion time versus radius also appearing in the background in grey. However, even with the rises and falls being captured in the rotation curve, the β parameter and the depletion time still do not exhibit any particularly clear correlation.

In addition to not producing any significant improvement, there are other reasons that the spline fits could not be used in the main analysis. First, the weighted spline fits for the rotation curves require custom knots for each galaxy, meaning that all of the galaxies would essentially have their final rotation curves tailored by hand until it was arbitrarily deemed sufficient. The spline fits could not be done procedurally (i.e. consistently and without ambiguity) for the galaxies. Secondly, the spline fits do not involve the necessary beam-smearing correction, and finding another place to perform that step may has proven to be difficult (as DISKFIT itself responds poorly when attempting to correct for beam-smearing within that software), considering that the spline fit considers the rotation curve alone and does not involve the *mom1* map.

However, in spite of these additional difficulties, the main reason that theoretical rotation curve fits were preferred over spline fits in the main analysis is that

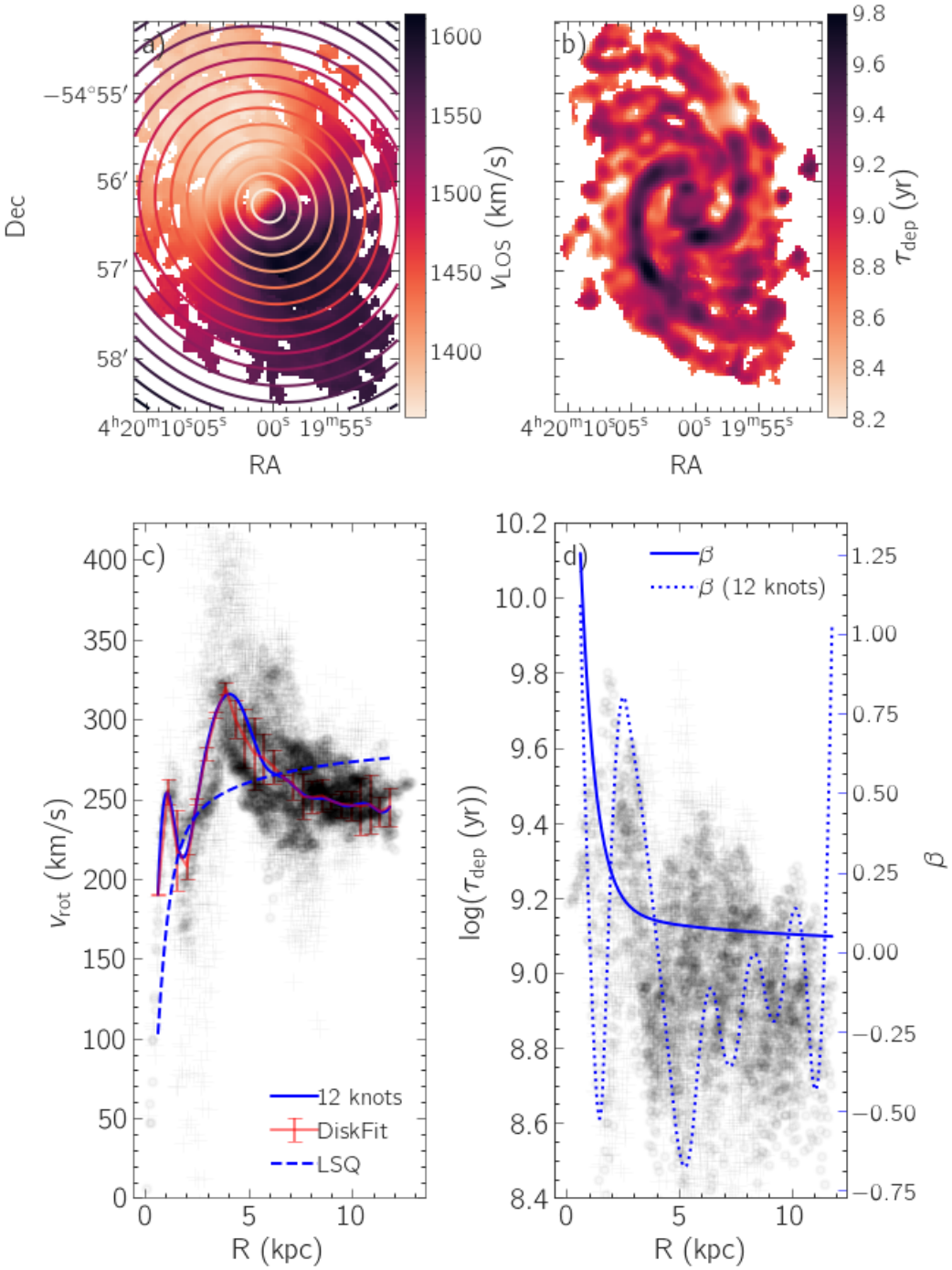

Figure C.1: Example comparison between the LSQ-smoothed URC and the spline-smoothed rotation curve for NGC1566. (a) Observed line-of-sight velocity. (b) Depletion time. (c) Compares each of the smoothed rotation curves to the DISKFIT output curve as well as the deprojected *mom1* data, in grey (where the dots indicate *mom1* data along the major axis, and the "+" marks indicate *mom1* data elsewhere). (d) Compares the β curves of both the LSQ-smoothed and spline-smoothed rotation curves (blue) to the depletion time as a function of radius (grey, with dots and "+" defined similarly).

the erratic rising/falling behaviours seen in the *mom1* maps are signs of noncircular motions throughout the galaxy, and are not necessarily representative of the underlying mass distribution. This underlying mass distribution is responsible for the circular motions throughout each galaxy, which is the underlying mechanic behind the large-scale shearing motions of the galaxy that we are considering to begin with.

Appendix D

DISKFIT: Alternatives to Centroid Velocity

As described in Section 3.1, the final line-of-sight velocity maps that were used for each galaxy were the 7m centroid "moment 1" maps from the PHANGS data. However, in order to generate the best possible parameter fits and rotation curves, a variety of options for the line-of-sight velocity maps were considered for DISKFIT.

The automated DISKFIT code was run on a wider variety of maps than the final 7m "moment 1" maps presented in the main report. In addition to these 7m "moment 1" maps, we also attempted 12m+7m "moment 1" data (with 12m+7m+tp where available) for its higher resolution and improved details. When the 7m data proved to be more reliable due to its wider coverage, we also attempted a "hybrid" version of these maps; that is, "moment 1" maps that used the 12m+7m data where available and 7m otherwise (such that the "hybrid" maps contained all the details of the 12m+7m data, and all the coverage of the 7m data). In addition, peak velocity maps (hereafter "*peakvels*") were attempted instead of the "moment 1" data for all aforementioned resolutions (and combinations thereof), in hopes that they would be more accurate as a velocity map for DISKFIT to use.

In the end, the 7m "moment 1" maps provided the most stable and consistent galaxy parameter fits and rotation curves.

D.1 12m+7m Maps

The key advantage that the 12m+7m maps offer is their substantially higher resolution, although it comes at the cost of coverage (that is, a 12m+7m map has more "empty space" than its corresponding 7m map does, under similar masking methods). DISKFIT tends to not respond well to holes and gaps in coverage, so the 12m+7m maps proved to yield inconsistent results that seldom looked as believable as (let alone better than) what the 7m data was capable of offering.

D.2 Hybrid Maps

The "hybrid" maps attempted to take advantage of both the 12m+7m data's high resolution and the 7m data's wider coverage, by simply filling in with 7m data wherever 12m+7m data was absent. However, DISKFIT produced inconsistent fits that also seldom looked as believable as (let alone better than) what the 7m data was capable of offering.

D.3 Peak Velocity Maps

A data cube is essentially a map containing a spectrum at each pixel (where the frequencies of the spectrum correspond to a line-of-sight velocity), and velocity maps are generated by finding the velocity of the CO(2-1) emission line. However, in lines of sight where the spectrum may have multiple peaks of similar intensity at different velocities, the method of velocity centroids (Equation 2.3) will fail to choose one of them and instead awkwardly select a velocity somewhere in the middle. Choosing the peak velocity instead circumvents this issue, thus producing a map of the brightest line-of-sight velocities (with these values being found by performing a quadratic fit at the spectral peaks so as to reduce inaccuracies from limited spectral resolution).

However, in lines of sight with multiple peaks in the spectrum of similar intensity, simply selecting the most intense velocity bears the risk of selecting a peak that is not necessarily indicative of the galaxy's motion. In nearby lines of sight, where

one of these multiple peaks in the spectrum becomes slightly higher than the other, the peak velocity method also risks selecting two completely different velocities in adjacent lines of sight, causing the final velocity map to have more "jitter" than the centroid method. In the end, between the two, the centroid maps produced more consistent and reliable fits with DISKFIT.